GEM TN-93-458

GEM Magnetic Field Measurements Meeting

MIT Building NW22, Room 150
Boston, MA

August 20, 1993

Abstract:

Agenda, attendees, and presentations of the GEM Magnetic Field Measurements Meeting held in Boston, MA. on August 20, 1993.

The meeting on the GEM magnetic field measurements.
Friday, August 20. MIT building NW22, Room 150, 185 Albany St., Boston

A G E N D A

8:30	Richard Stroynowski	- Introduction
8:45	Frank Taylor	- Muon system requirements for the knowledge of the magnetic field.
9:30	Bob Granetz	- Field measurements at Alcator-Cmod
9:50	Emanuel Bobrov	- NMR field measurements
10:15	coffee break	
10:30	Jeff Freidberg	- Mathematical methods
11:00	Bob Pillsbury	- Methods used in plasma fusion magnets
11:30	Larry Rubin (?)	- Magnetic field sensors
12:00	lunch break	
13:00	Orin Fackler	- TOSCA calculations, fits etc
14:00	Jim Sullivan	- distributed source approach

Name	Telephone		Email
Jim Sullivan	617-253-7537	MIT	Sullivan@MITLNS
JEFF FREIDBERG	617-253-8670	MIT	
BOB PILLSBURY	617-253-8605	MIT	RDPJ@PFC.MIT.EDU
Robert Granetz	" " 8634	MIT	GRANETZ@PFC.MIT.EDU
Leonard Myatt	617-253-3157	MIT	MYATT@PFC.MIT.EDU
Vinnie Polychronakos	516-282-3982	BNL	POLYCHRON@BNLDAG.AGS.BNL.GOV
BRAD SMITH	617-258-7852	MIT	SMITH@PFC.MIT.EDU
Nicolai Martovetsky	214 708 6324	SSCL	MARTOVETSKY@SSCVX1
Peter G Marston	MIT-PFC		
Orrin Fackler	(510) 423-1766	LLNL	FACKLER@NEU.LLNL.GOV
Richard Stoynowski	(214) 768-4076	SMU	RYSZARD@SSCVX1.SSC.GOV
Frank Taylor	(617) 253-7245	MIT	FET@MITLNS
Emanuel Bobrov	(617) 253-5406	MIT	BOBROV@PFC.MIT.EDU
Bill Punchard	(617) 253-2860	MIT (FBNML)	
E. A. Chaniotakis	MIT PFC		
Larry Rubin	617 253 5517	MIT (FBNML)	

GEM MAGNET

OPEN FIELD SUPERCONDUCTING SOLENOID WITH TWO FORWARD FIELD SHAPING IRON PIECES (TRUNCATED CONES).

→ NON-UNIFORM FIELD
IN A VOLUME ~ 7880 m^3
CENTRAL VALUE 0.8T

MAGNETIC FIELD TOGETHER WITH MEASUREMENT OF THE TRAJECTORY IS USED TO DETERMINE MOMENTUM OF CHARGED PARTICLES IN

CENTRAL TRACKER
MUON SYSTEM

HOW WELL DO WE NEED TO KNOW MAGNETIC FIELD

TDR FIELD INTEGRAL ALONG TRAJECTORY

0.09T (10-30)% IN CENTRAL TRACKER

0.4 % IN MUON SYSTEM

LOCAL KNOWLEDGE 0.5% (?) CENTRAL TRACKER

(FRANK TAYLOR'S TALK)

GEM DETECTOR MAGNET SYSTEM

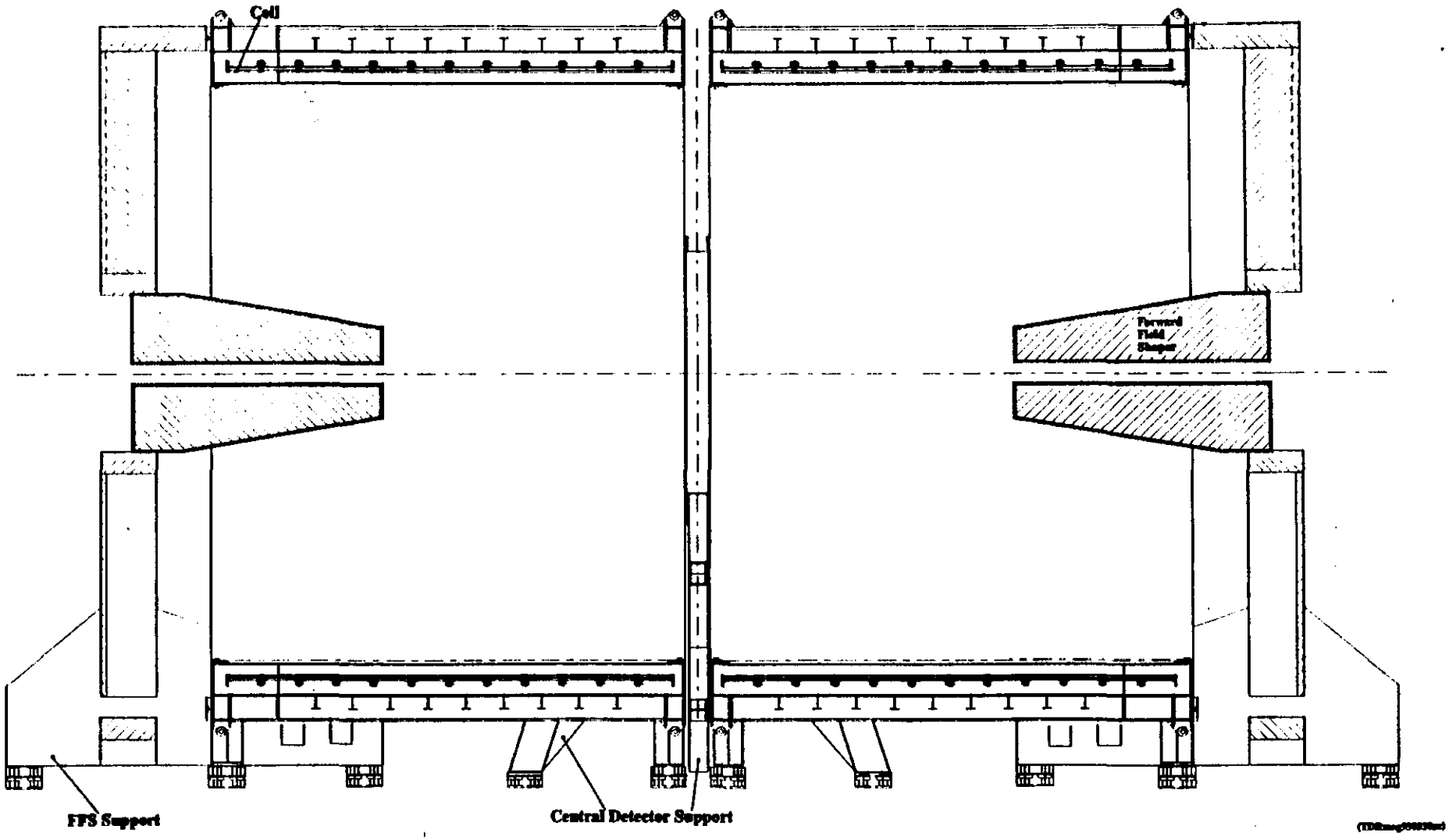

OPTION A _ PHASE 10

NORTH FFS INSTALLATION

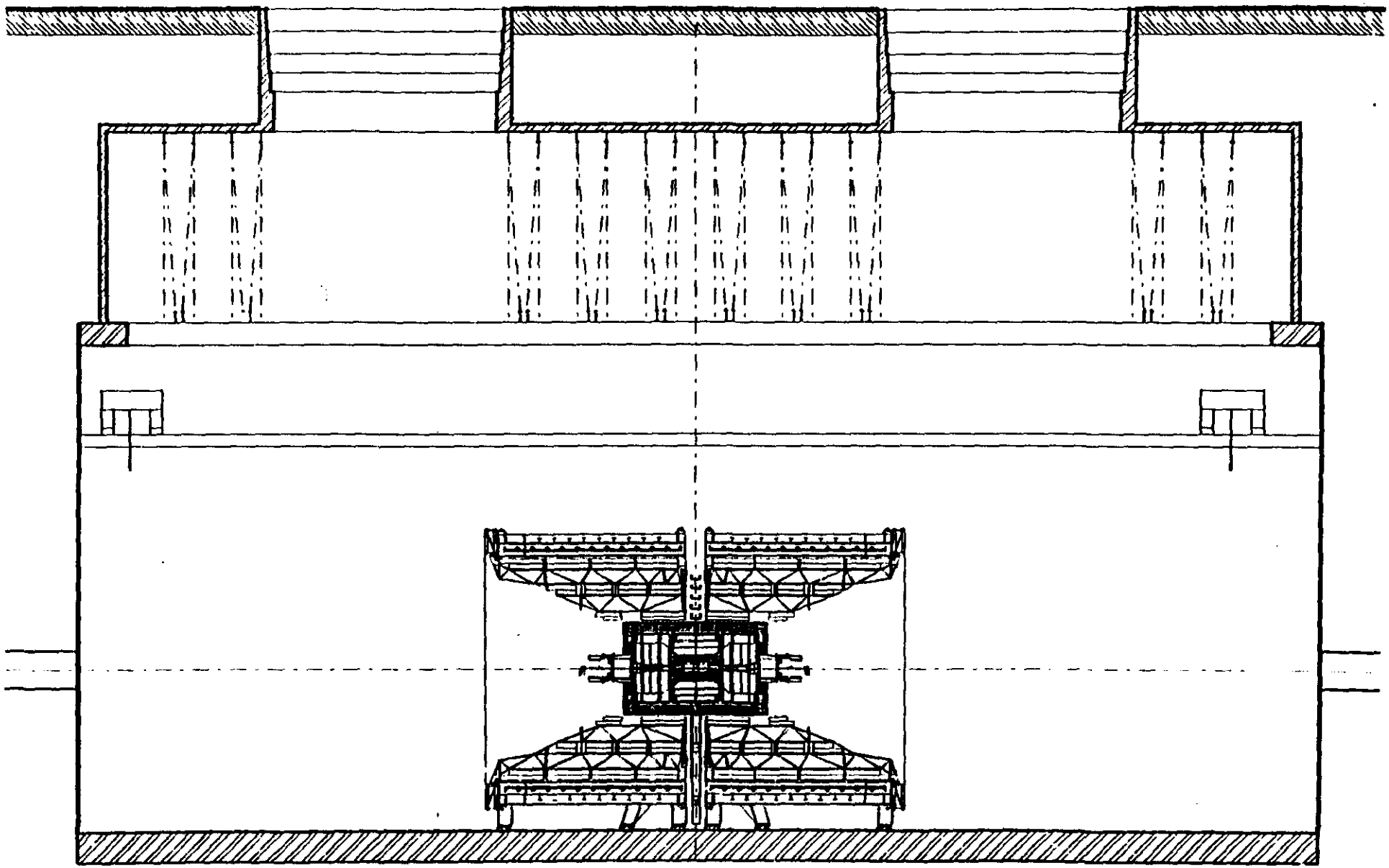

OPTION A _ PHASE II

SOUTH FFS INSTALLATION

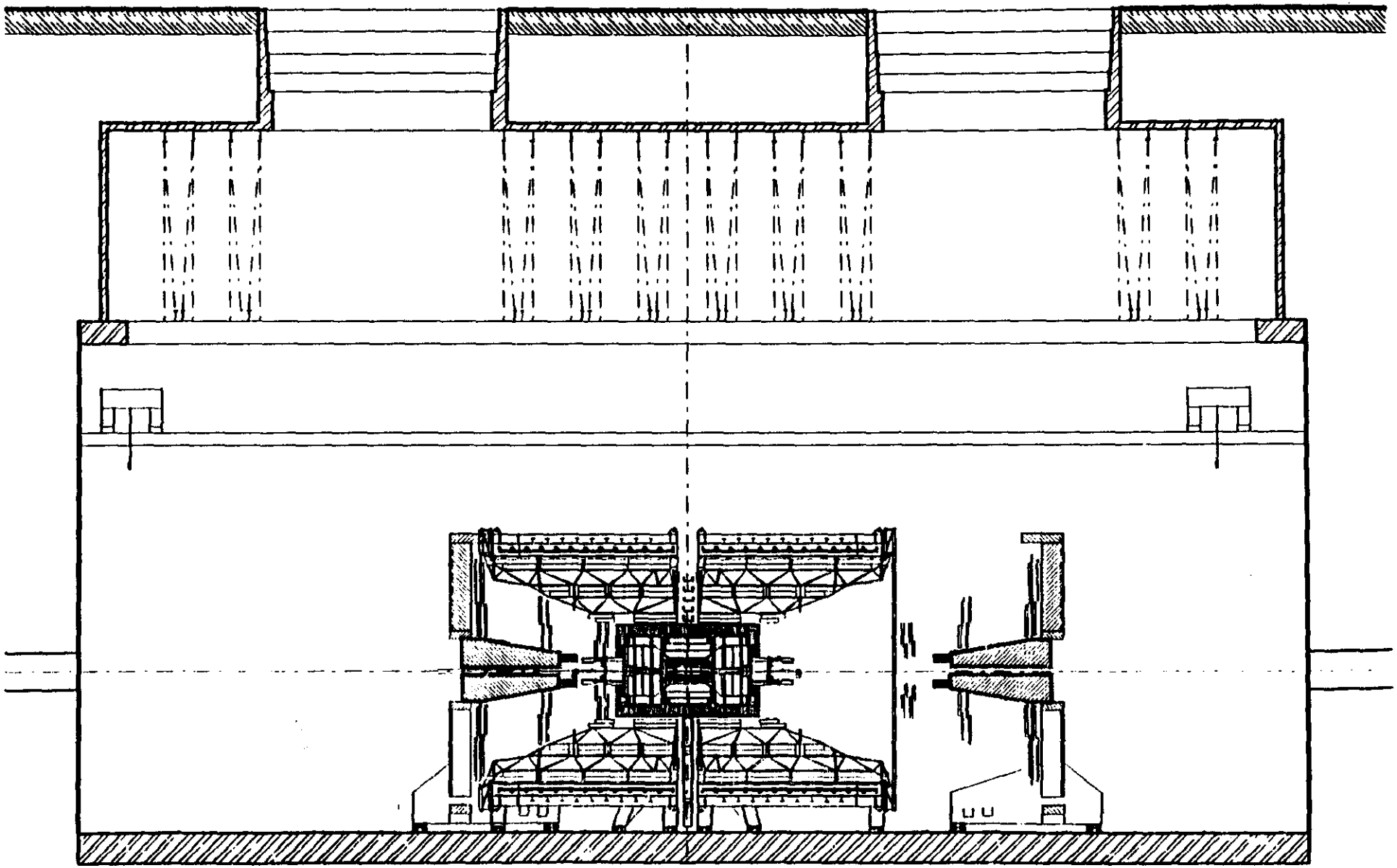

INSTALLATION SCHEDULE (BASELINE)

MAGNET - TWO HALF COILS COMPLETED, INSTALLED TESTED MARCH 1997.

FORWARD FIELD SHAPERS INSTALLED AUGUST - OCTOBER 1998 **AFTER** INSTALLATION OF MUON SYSTEM AND CALORIMETERS.

REASONS FOR THIS SCENARIO

- RESOURCE LOADED FUNDING PROFILE
  EARLY COMPLETION OF FFS WOULD REQUIRE EARLY COMMITTMENT OF SUBSTANTIAL FUNDING
- FUNDING UNCERTAINTY
  MAY NEED TO STAGE, FFS IS A GOOD CANDIDATE
- EASE OF INSTALLATION

	FY91	FY92	FY93	FY94	FY95	FY96	FY97	FY98	FY99	TOTAL
FFS	$0	$0	$745	$122	$6,836	$4,947	$2,023	$739	$80	$15,492
Bal of Magnet	$200	$2,900	$13,225	$43,398	$30,424	$16,243	$3,277	$171	$0	$109,838
TOTAL	**$200**	**$2,900**	**$13,970**	**$43,520**	**$37,260**	**$21,190**	**$5,300**	**$910**	**$80**	**$125,330**

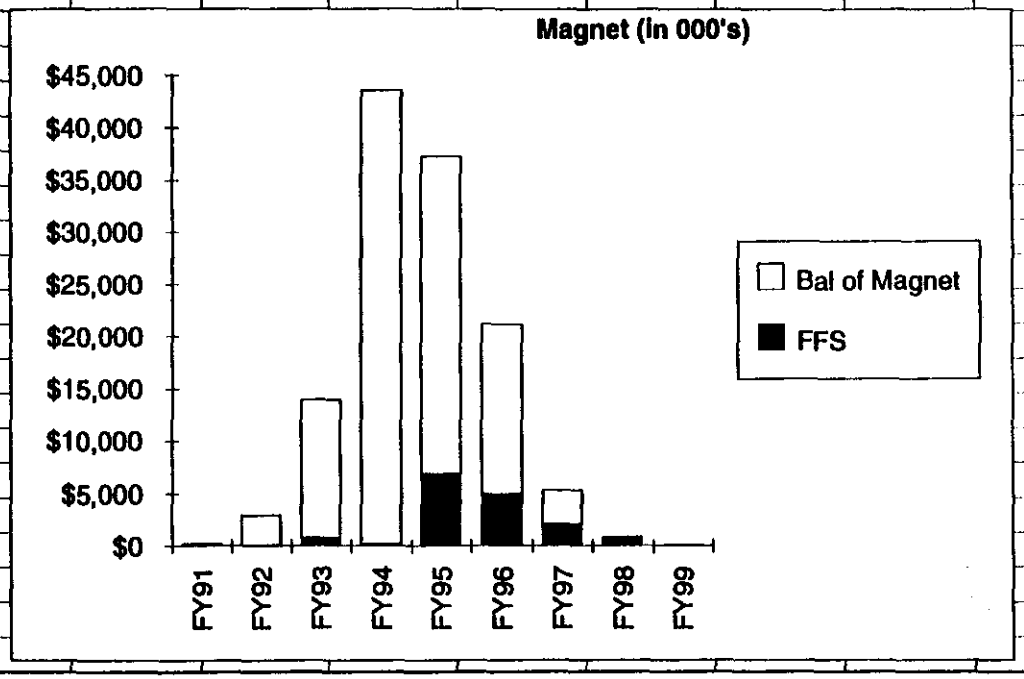

- CONSEQUENCES OF INSTALLATION SCENARIO

FIELD AT TIME OF EARLY MAGNET TEST (SOLENOID ONLY) IS DRAMATICALLY DIFFERENT FROM THAT OF COMPLETED MAGNET ASSEMBLY

FIELD HAS TO BE MEASURED WITH CALORIMETRY AND MUON SYSTEM IN PLACE — STANDARD FIELD MAPPING OF A GRID OF SPACE POINTS CANNOT BE DONE.

FIELD HAS TO BE KNOWN FOR ALL INSTALLATIO AND STAGING SENARIOS

- TWO HALF-COILS ONLY
- HALF-COILS WITH FFS
- HISTERESIS EFFECTS

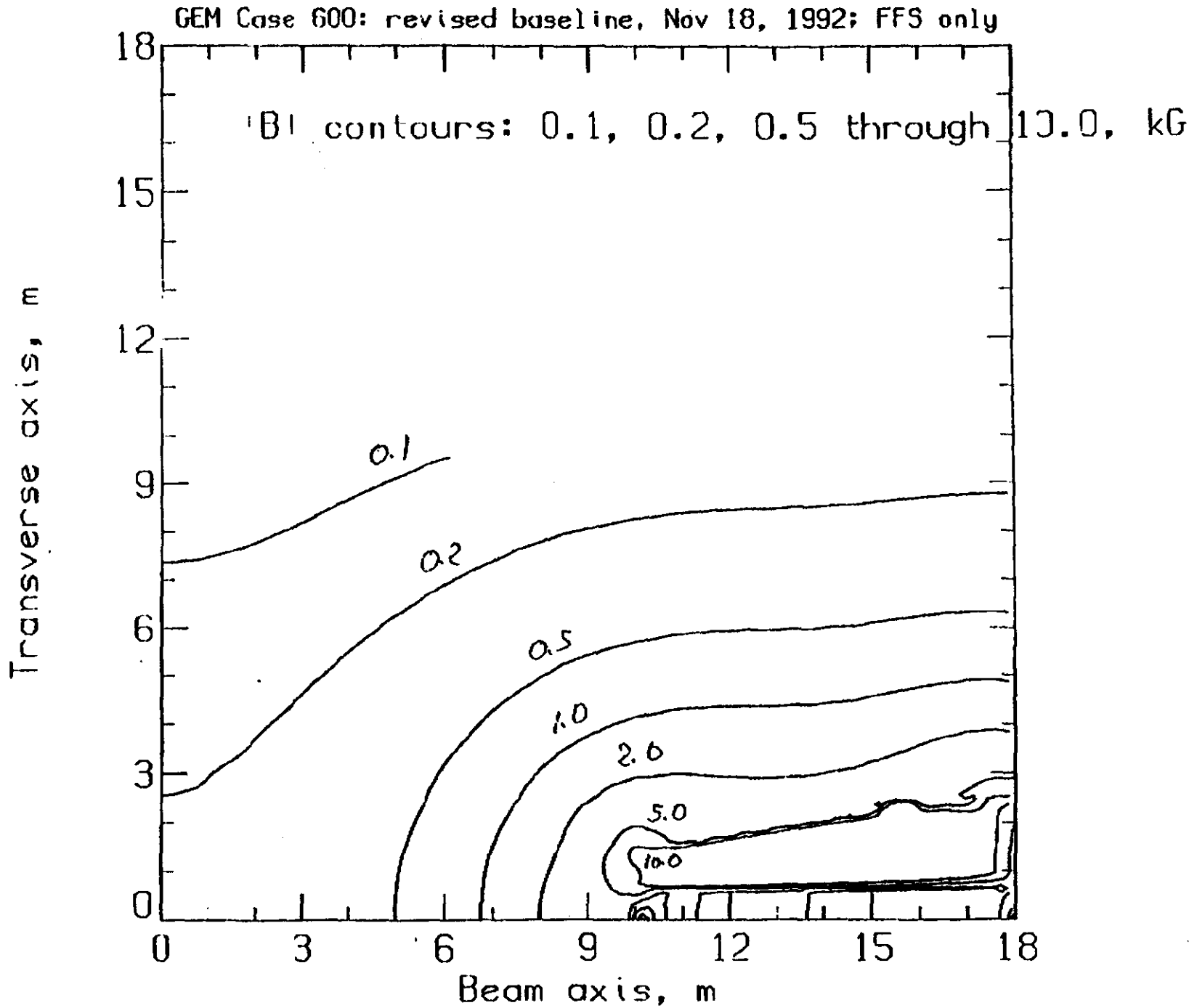

Field difference between a completed and stripped (no FFS) magnet,

GEM Case 600: revised baseline, Nov 18, 1992
solenoid on!

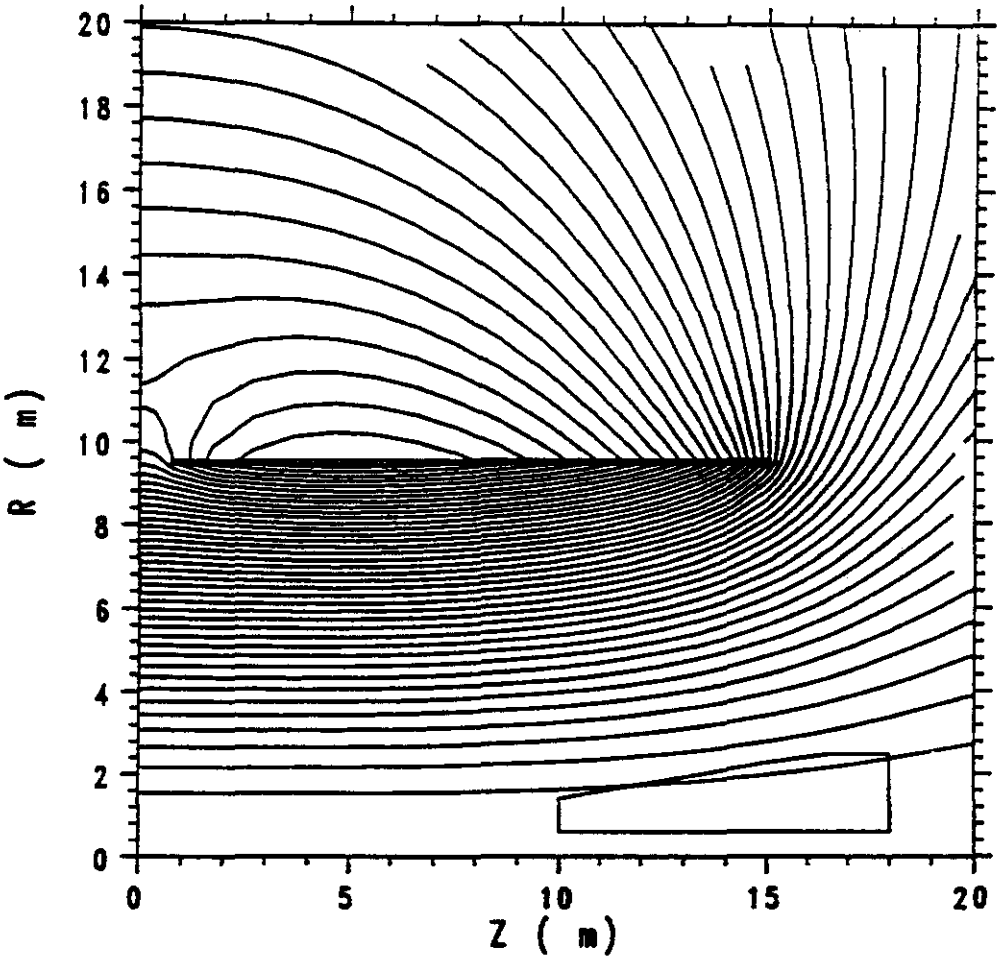

GEM Field ~~fin~~ — no FFS

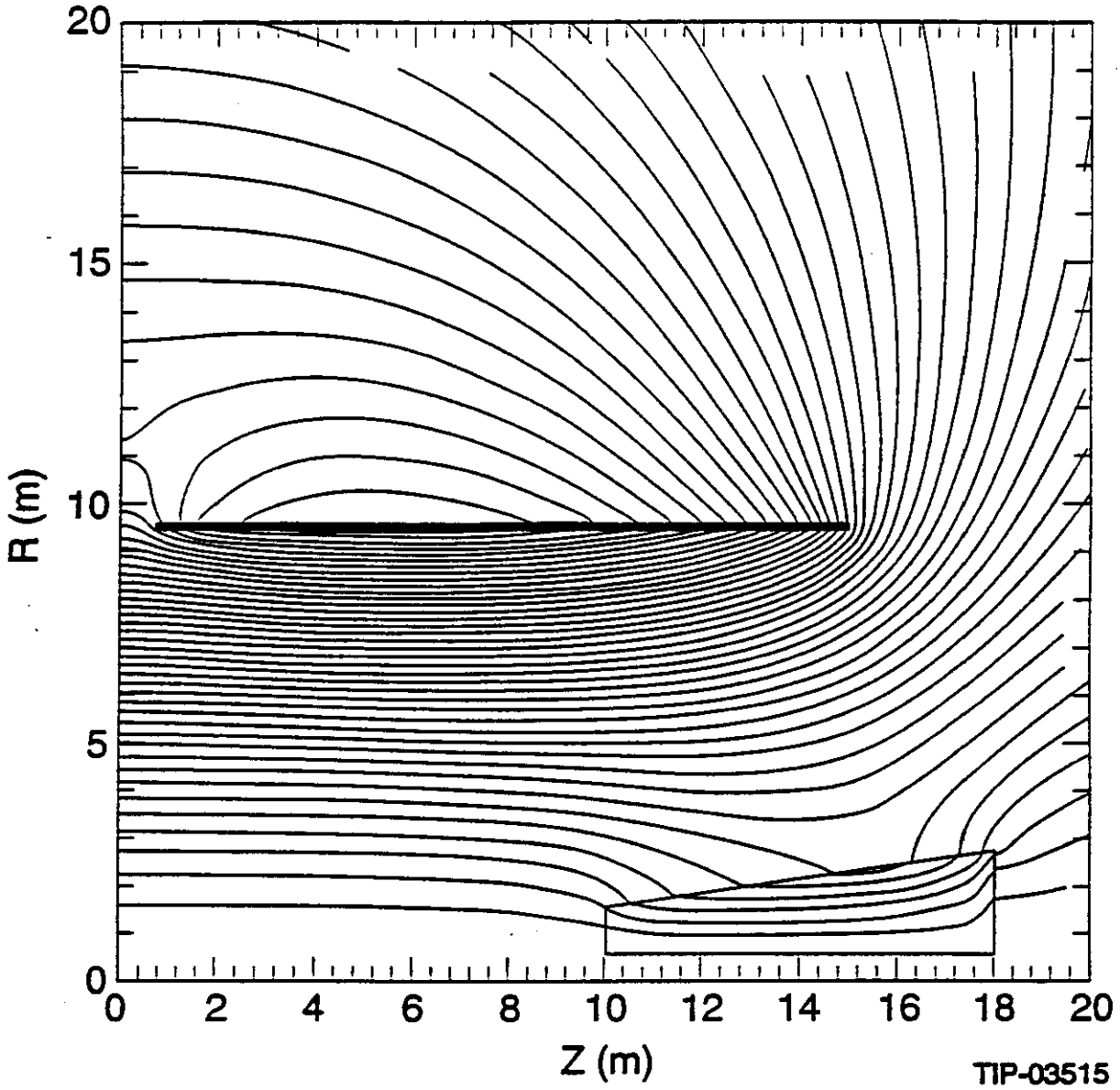

BASELINE GEM FIELD

3-4

F.E. Taylor - MIT
August 20, 1993

How Well Does The GEM B-field Need To Be Known ?

- **Criteria:**

  (1) Accuracy in reconstructing the sagitta of muon trajectory.

  (2) Corrections for the L-angle effect in muon chambers.

- **Memo:**

  Sullivan and Taylor Feb. 23, 1993

- **Considerations:**

  (1) Specification of field tied to overall system performance.

  (2) Non-uniform field ==> approximate L-angle compensation.

MASSACHUSETTS INSTITUTE OF TECHNOLOGY
LABORATORY FOR NUCLEAR SCIENCE
CAMBRIDGE, MASSACHUSETTS 02139

TO: Gary Sanders - GEM Project Manager
FROM: Frank Taylor and Jim Sullivan - GEM Muon System / JET JAS
SUBJECT: Knowledge Requirement of GEM Magnetic Field
DATE: February 23, 1993

The muon system requires that the magnetic field be known accurately. There are two major considerations which drive the magnetic field knowledge:

- Accuracy of reconstructing the sagitta of the muon trajectory.
- Corrections for the Lorentz angle effect in the muon tracking chambers.

Global Field Knowledge Requirement:

Including the energy-loss fluctuations in the calorimeter, the best transverse momentum resolution of the present GEM muon system is $\delta P_t/P_t = 2\%$. As a global field requirement we specify that any additional systematic error to the momentum resolution contributed by a lack of knowledge of the magnetic field may not exceed 20% of the minimum resolution, or 0.4%.

Thus we specify that the vector integral BL^2 (radial and longitudinal components) evaluated along rays from the IP at the chamber plane locations be known to < 0.4 % *.

Note that this criterion also applies to the knowledge requirement of any azimuthal non uniformity in the field as well as the reproducibility of the field for successive operation cycles.

Local Field Knowledge Requirement:

The single layer resolution of the CSC baseline technology has a Lorentz angle sensitivity of 60 μm/Tesla. As our criterion we specify that the total single layer resolution (chamber + random systematic misalignments) be degraded by no more than 5% of its B=0 value. In our performance simulation model the chamber single layer resolution is added in quadrature with a 50 μm random systematic error. Taking the chamber single layer resolution to be 75 μm this criterion requires that the Lorentz angle smearing be no more than a 7% contribution, i.e. 75 μm is allowed to be degraded to a value no more than 80.25 μm. Note that both the direction and magnitude of the field are important in the Lorentz angle correction.

This implies that the error of local field vector must not exceed $\Delta B < 0.09$ T.

In summary, the integral BL^2 value is the driving requirement, meaning that field measurements should be focused on evaluating this quantity, particularly in regions of large field gradient and magnitude.

---

* By BL^2 we mean the double integral:

$$BL^2 = 2\int_0^L dl' \int_0^{l'} B \times dl$$

where dl is a differential ray-vector (dl' is a scaler), B is the vector magnetic field, and L is evaluated at the locations of the chamber planes.

cc: Barry Barish
Gary Deis
Norm Gober
Mike Harris
Peter Marston
Mike Marx
Nicolai Martovetsky
Gena Mitselmakher
Vinnie Polychronakos
Paul Reardon
Larry Rosenson
Brad Smith
Ryzard Stroynowski
Alexie Vorobyov
Scott Whitaker
Bill Willis

CLEAR TOPPER

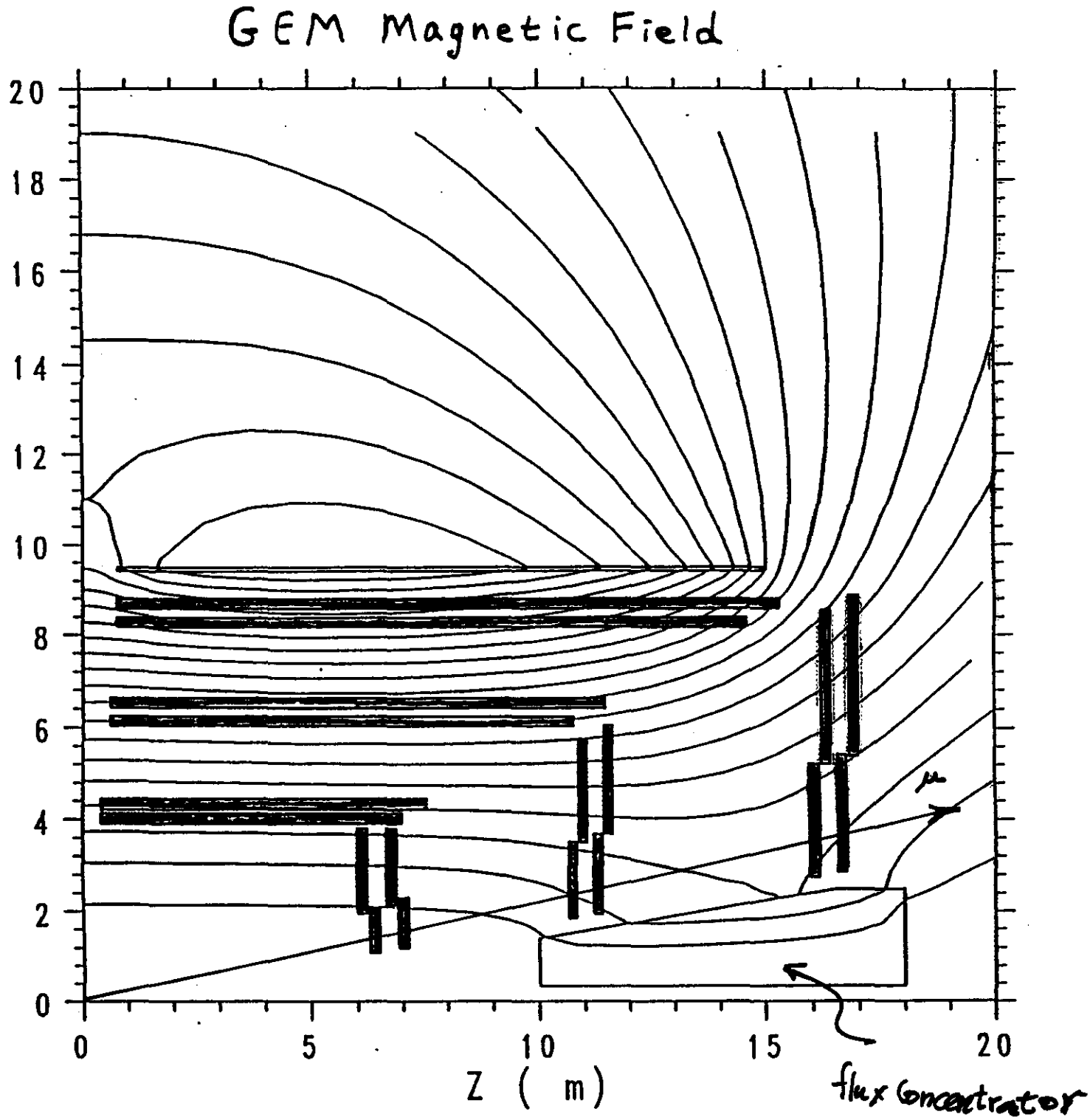

2 ϕ segments of chambers shown

Factors Affecting Pt Resolution

Parametric Model of Resolutions*

Barrel:

$$S_{total} \approx \frac{0.3B(R_3-R_1)^2}{8p_t} \sim BL^2$$

$$\sigma_{1,3}^2 = \sigma_e^2 + \frac{(\sigma_i^2+\sigma_c^2)}{N_{1,3}}$$

$$\sigma_2^2 = \sigma_e^2 + \frac{(\sigma_i^2+\sigma_c^2)}{N_2} + \sigma_{ms}^2$$

$$\sigma_{ms}^2 = \left(\frac{0.015(R_3-R_1)}{Pt}\right)^2 \frac{X_0 N_2}{16 \sin\theta}$$

$$\sigma_{total}^2 = \sigma_2^2 + \frac{\sigma_1^2+\sigma_3^2}{4}$$

where: $\sigma_e \leq 25\ \mu m$, $\sigma_i \leq 50\ \mu m$, $\sigma_c \leq 75 \mu m$, $N_{1,2,3} = 6$, $X_0 = 0.011$/layer

Low Pt (< 100 GeV/c)

- Multiple scattering in SL2 material
- Fluctuations in energy loss in calorimeter

High Pt (≥ 100 GeV/c)

- Spatial resolution error budget: $s_{total} \leq 50\ \mu m$ at 500 GeV/c

* Actual calculations are done with non-uniform field

Global Field Knowledge Requirement

- Method:

To determine the muon momentum for three point measurement, solve:

$$P_t = \frac{\kappa \sin\theta}{8S(L,\theta)} \beta\lambda^2(L,\theta)$$

where:

$$\beta\lambda^2(L,\theta) = \left| 2 \int_0^L ds' \int_0^{s'} (\mathbf{dx} \times \mathbf{B}) \right|$$

- Measure $S(L,\theta)$, and θ

- Field map/model of magnet determines $\beta\lambda^2(L,\theta)$

- Require relative error in $\beta\lambda^2(L,\theta)$ be a small contribution, say < 0.4%.

P_T resolution with all contributions except BL^2

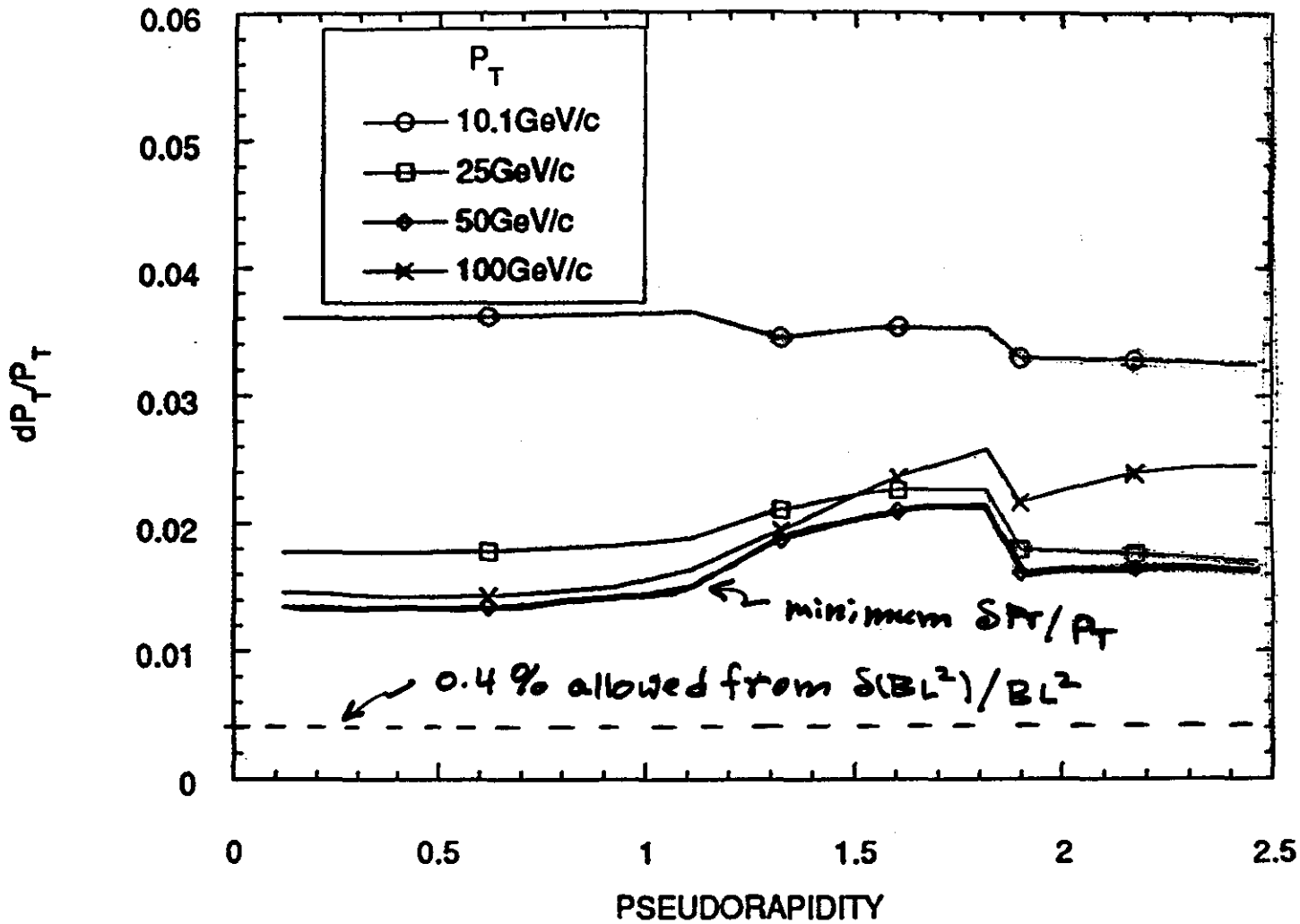

$\beta\lambda^2$ (BL^2) for Various θ-values

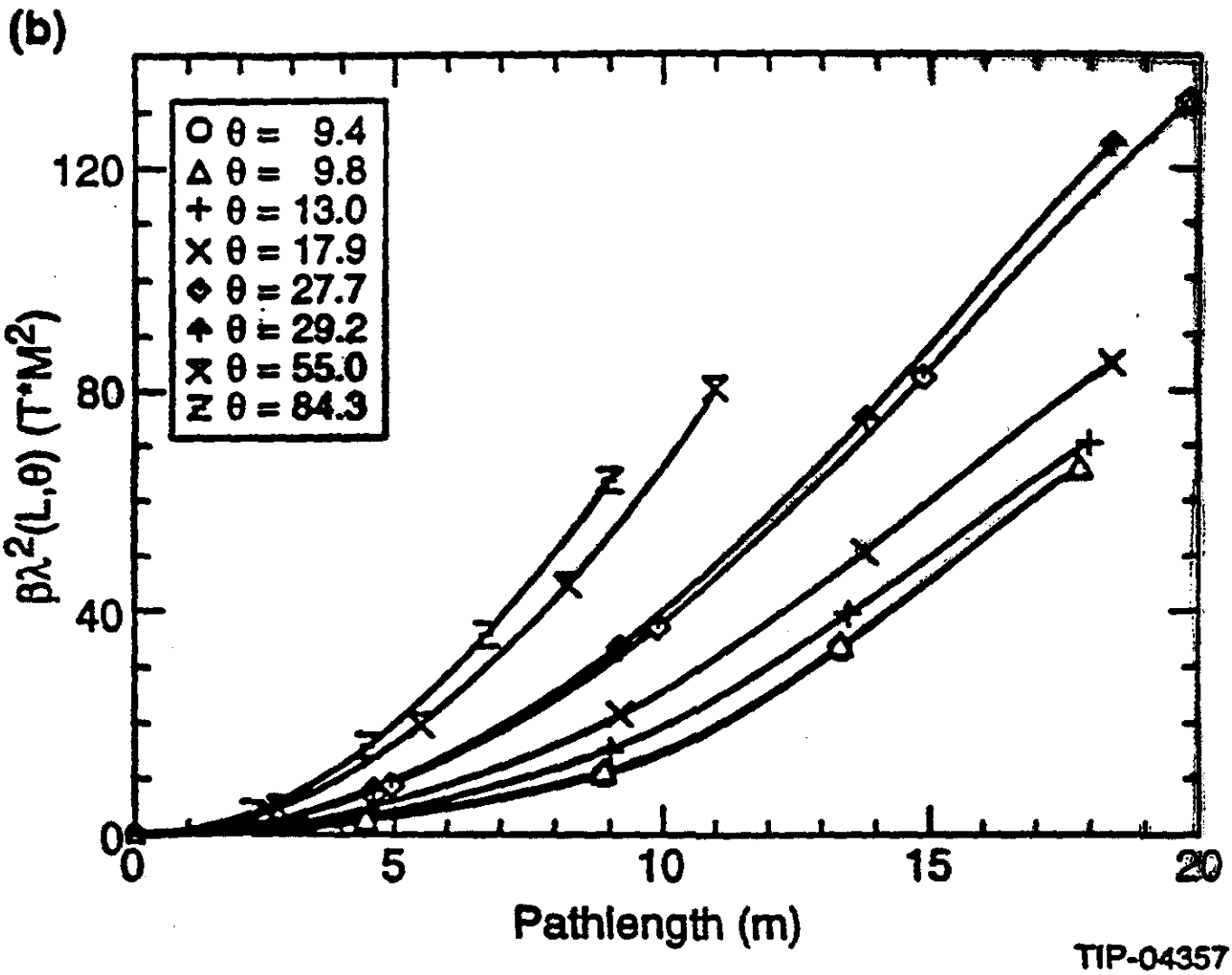

Orders of magnitude: Barrel $L \simeq 4\,m$, $B \simeq 0.8\,T$

error in B : $\delta B \leq 32$ gauss

error in L : $\delta L \leq 8\,mm$

Local Field Requirement

- Lorentz angle dependent on local B - value:

  - Barrel: $[B_z \times E_y]$ dominate term
  - Endcap: $[B_z \times E_y]$ dominate term but $[B_y \times E_z]$ significant

- Lorentz angle effect affects chamber resolution:

  - Barrel: SL_3 most strongly affected
  - Endcap: SL_2 and SL_3 affected

- Strategy:

  - Minimize resolution smearing on average

- Knowledge Requirement: [Changed from Memo]

  - Needed to design system
  - Variation over chamber area large
  - In some cases uncompensated, e.g. Endcap - SL2 $B_y \times E_z$ term

- Needed:

  - Full simulation of resol'n smearing from local B-field variations

Lorentz Angle Compensation

$$\tan \Theta_L \sim \frac{kB}{E}$$

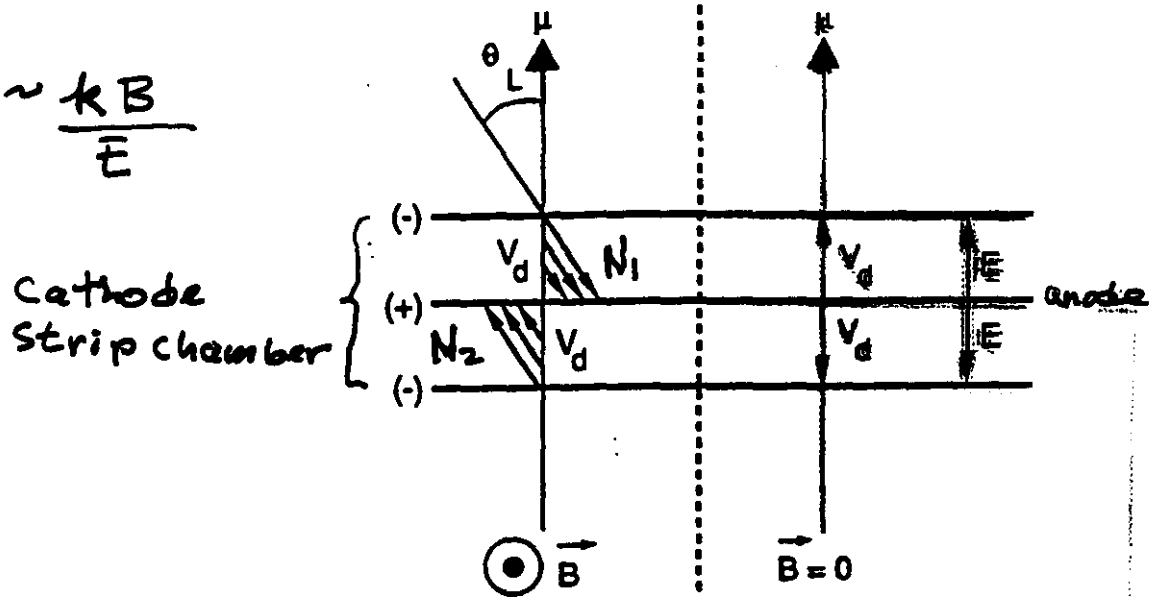

Solution for barrel region

ionization:

$N_1 \neq N_2 \Rightarrow$ resoln degraded

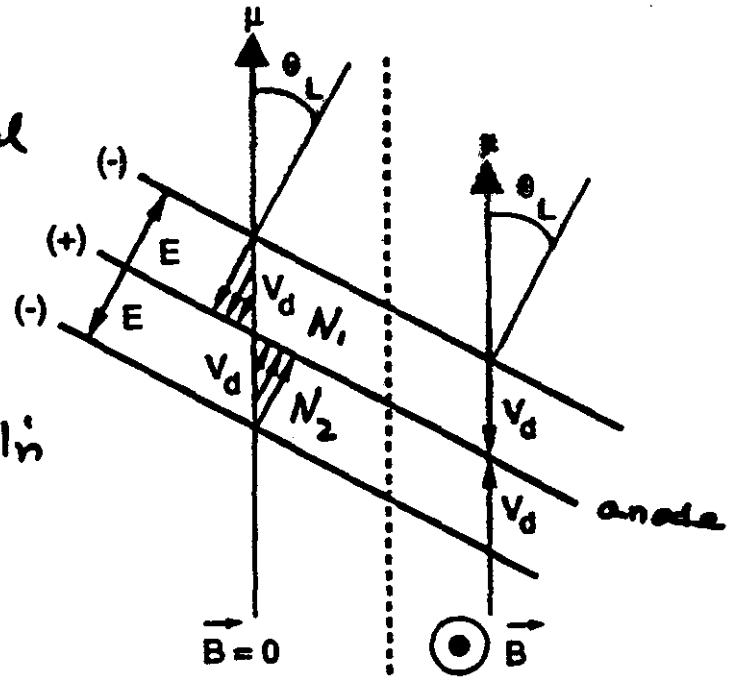

TIP-03883

FIG. 4-31. Sketch of the Lorentz effect for barrel.

Chamber resolution vs ϕ angle

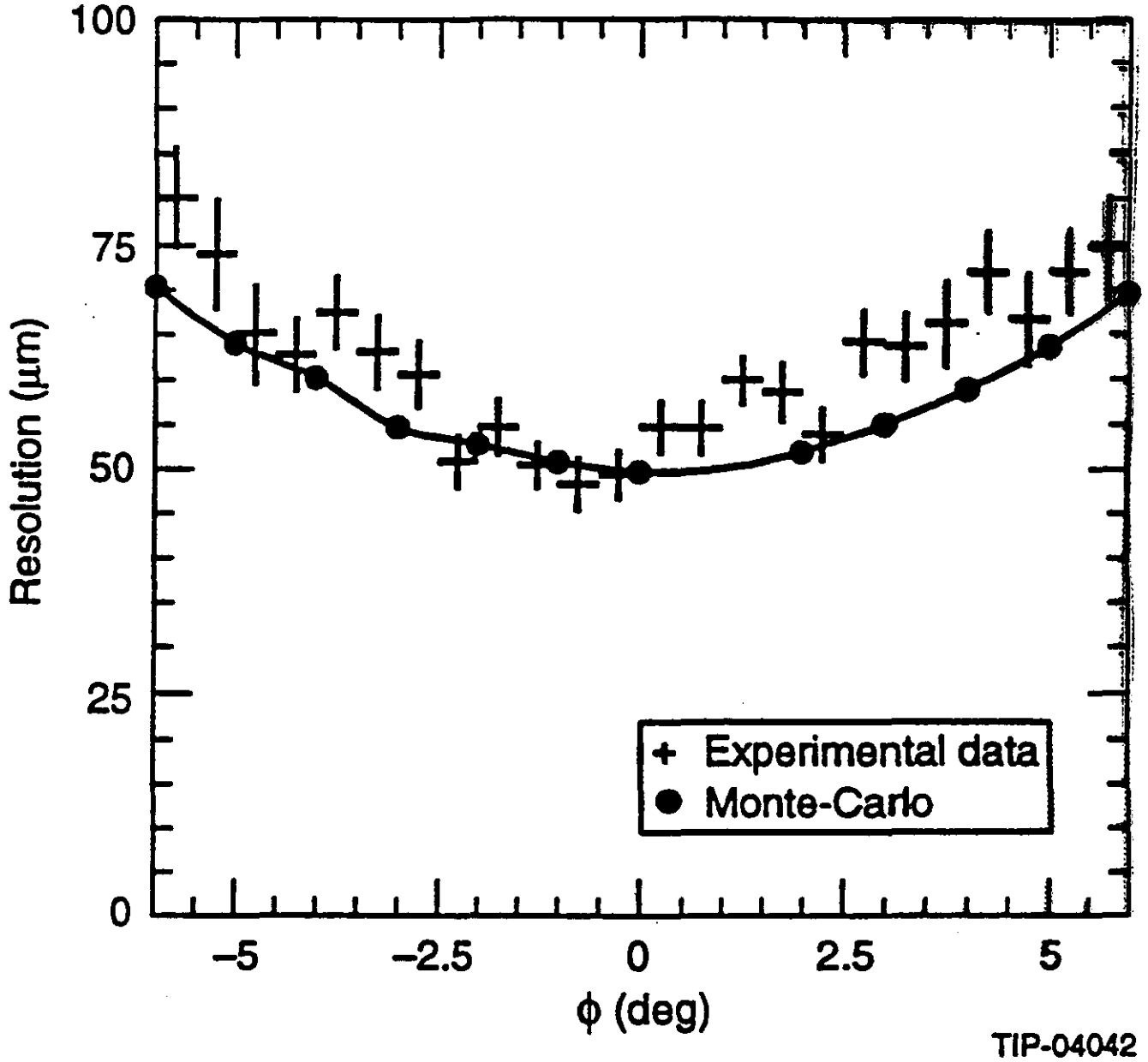

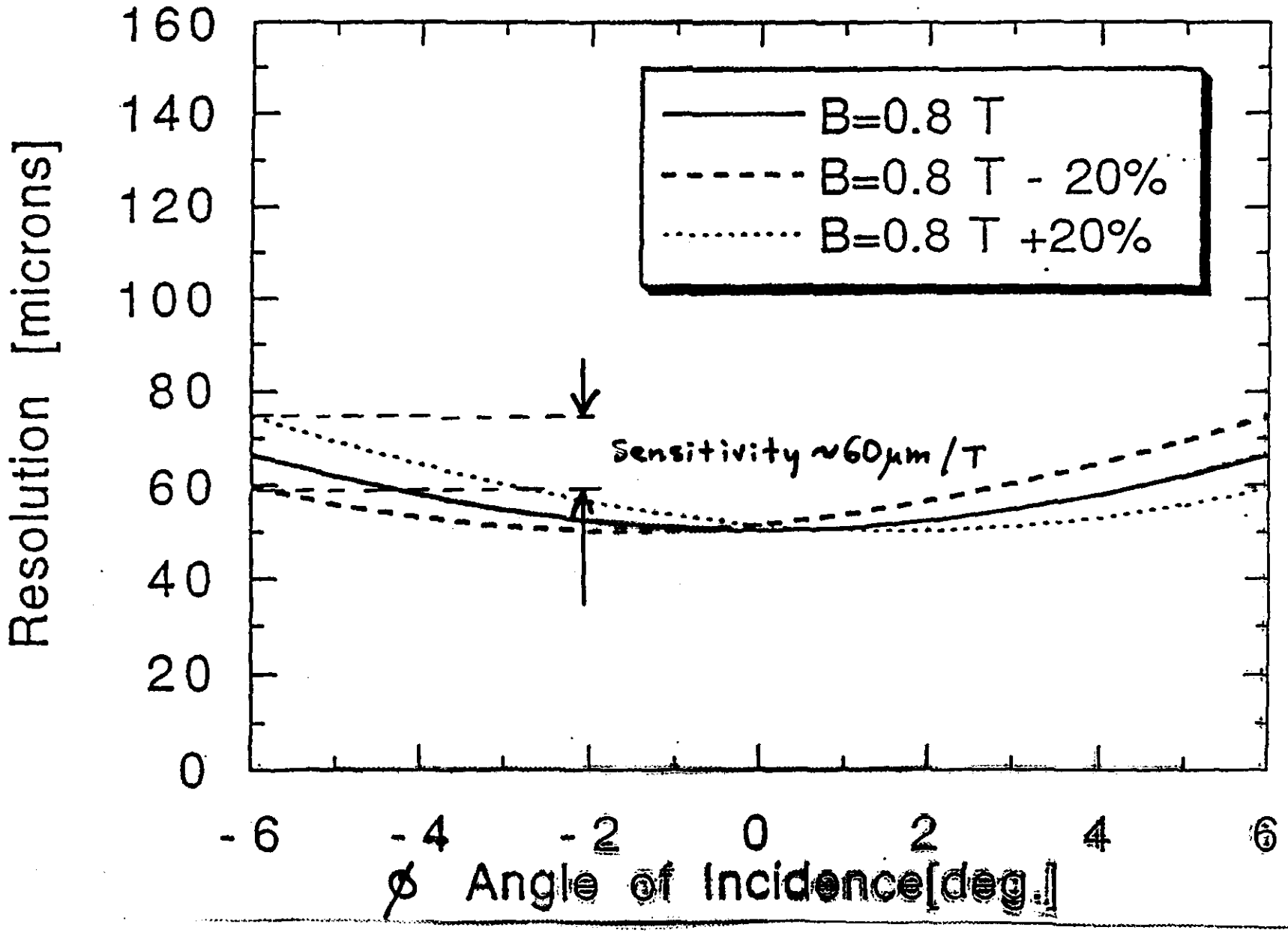
Resolution [microns]
160
140
120
100
80
60
40
20
0
-6
-4
-2
0
2
4
6
ϕ Angle of Incidence[deg.]
B=0.8 T
B=0.8 T - 20%
B=0.8 T +20%
Sensitivity ~60μm / T

Barrel Region

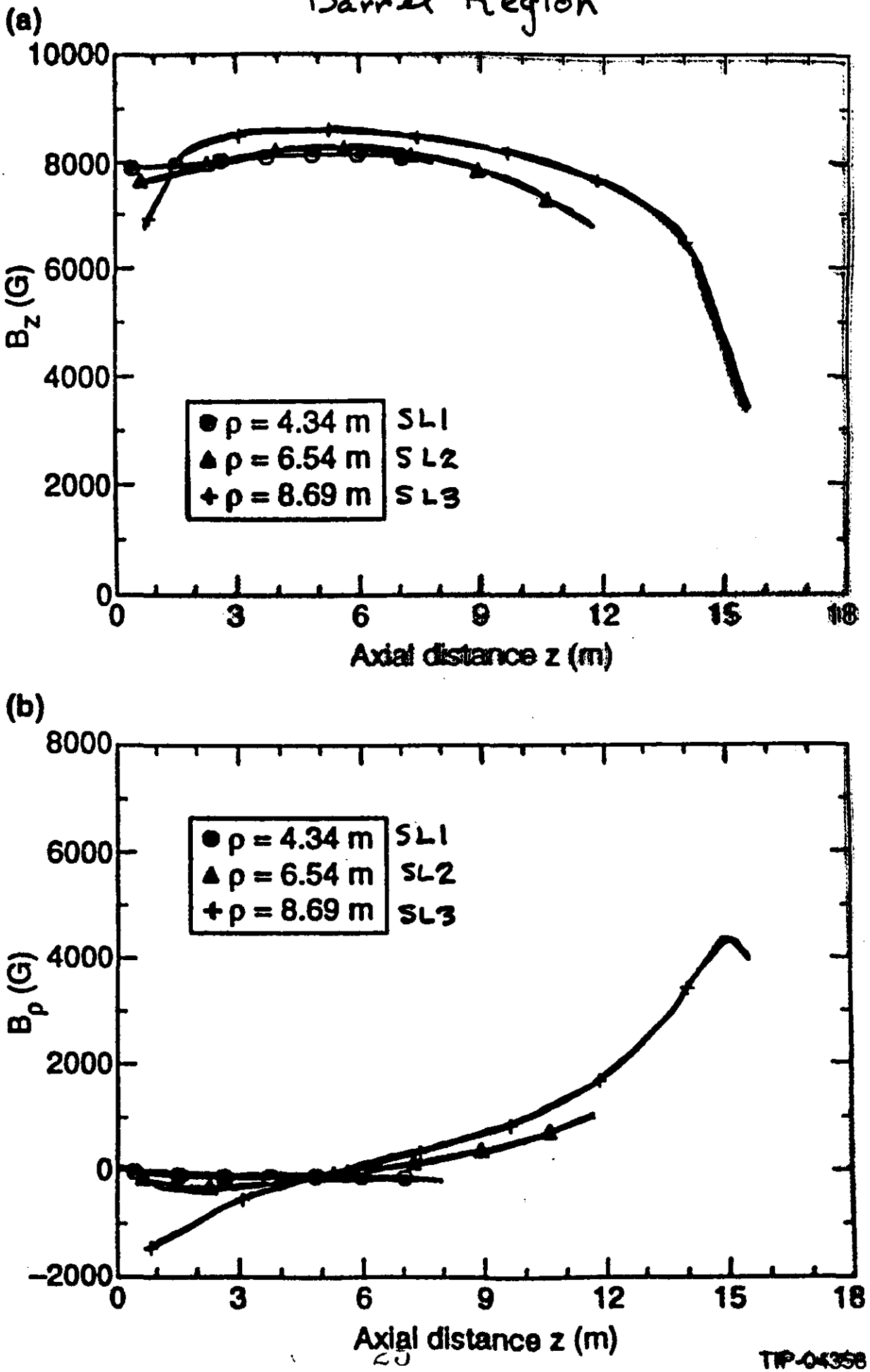

TIP-04358

Lorentz Angle Compensation - Barrel

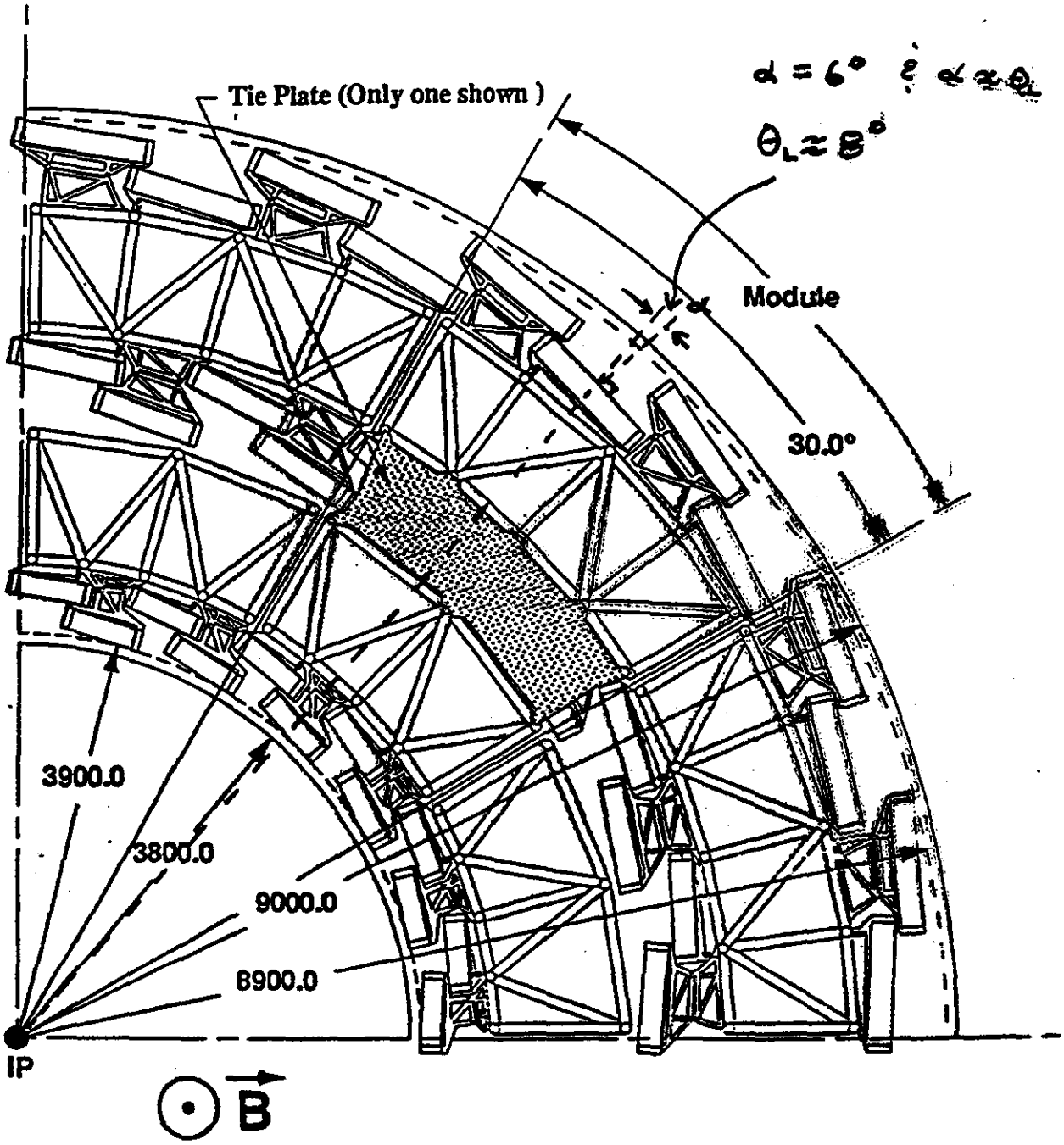

Barrel Region (End View)

Lorentz Angle Compensation End Caps

Contributions:

$\bar{B}_z \times \bar{E}_z \equiv 0$

Longitudinal component $\bar{B}$

$\bar{B}_z \times \bar{E}_y \neq 0$

Radial component $\bar{B}$

$\bar{B}_y \times \bar{E}_z \neq 0$

Choose to compensate

$\bar{B}_z \times \bar{E}_y$ component only

But $B_y \times E_z$ significant!

(a)

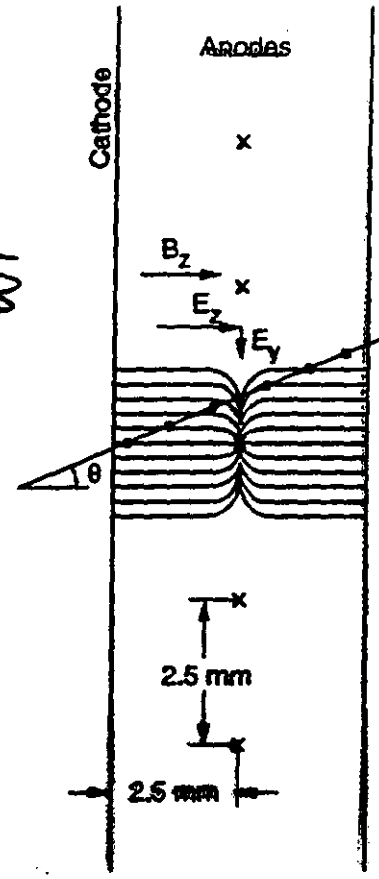

E_y is radial field component

(b)

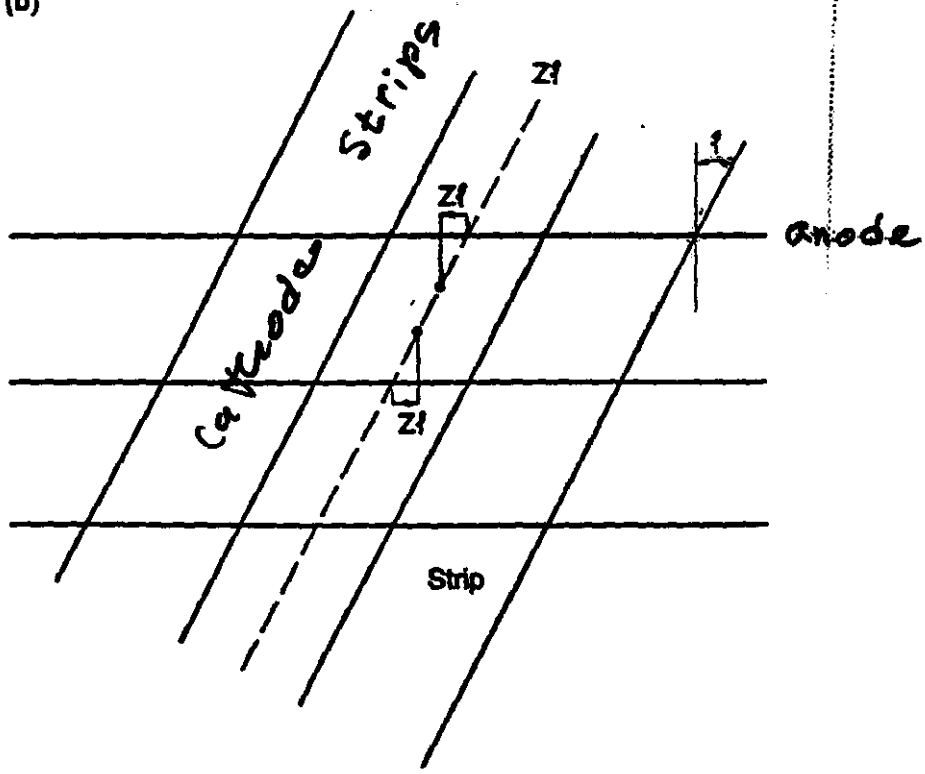

TIP-04359

Endcap Region

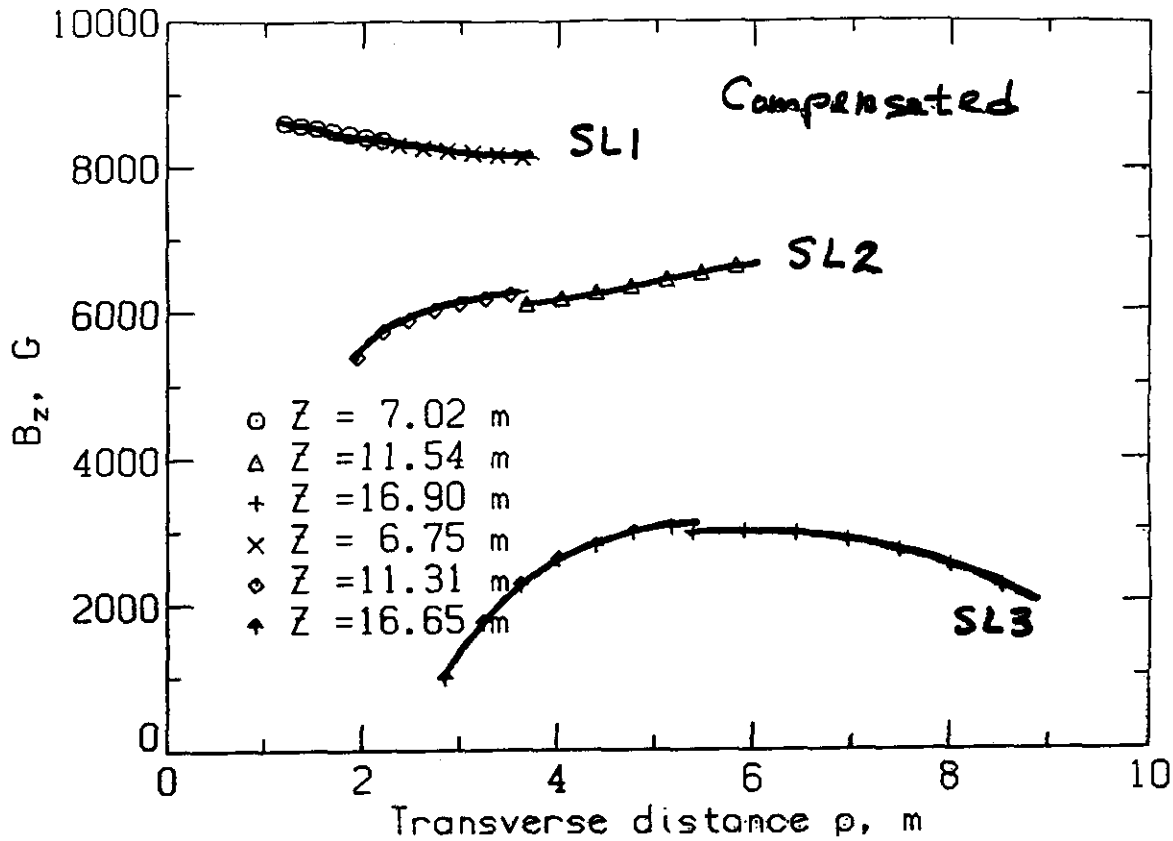

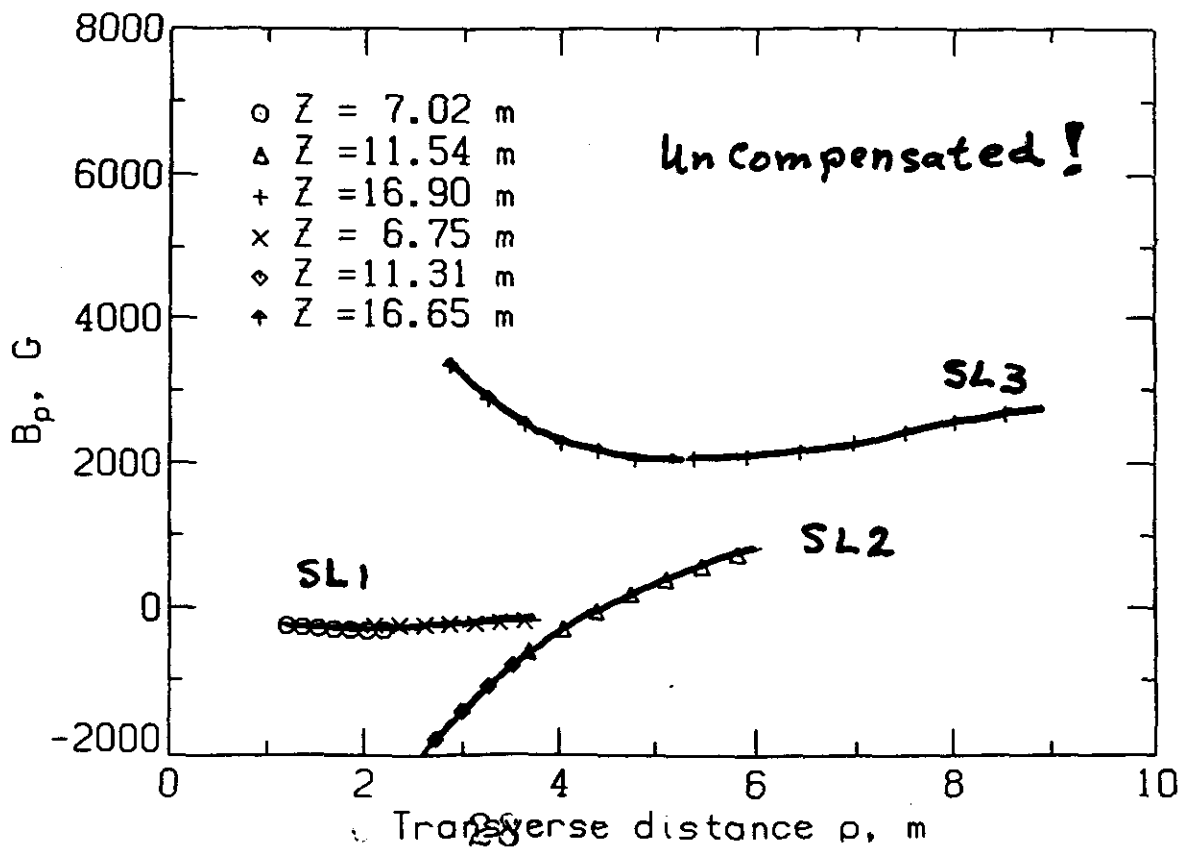

Endcap Cathode Strip Chamber

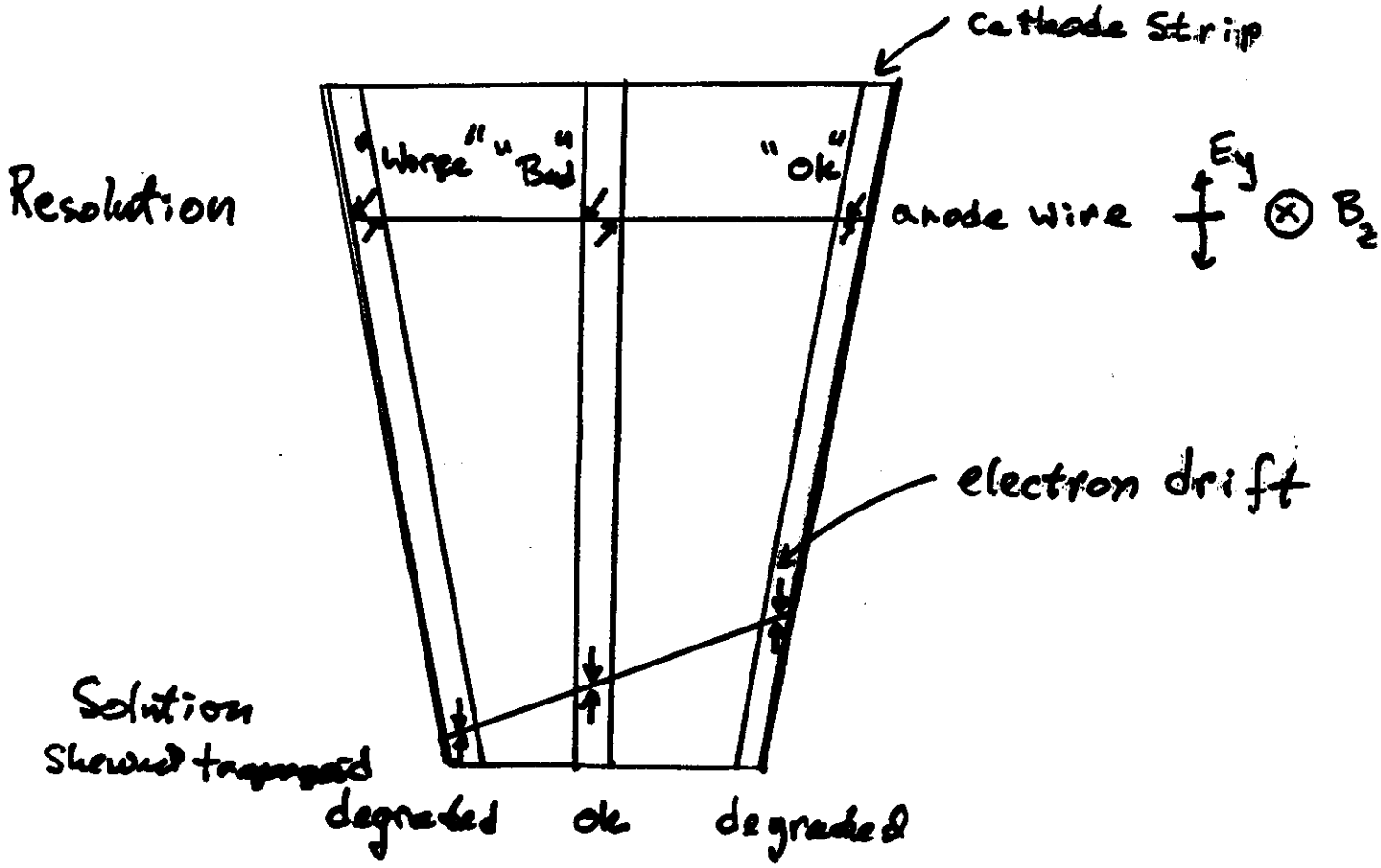

$E_y \times B_z$ term

Note $E_z \times B_y$ term not compensated

Summary of B-Field Knowledge

- BL^2 known to $\delta BL^2/BL^2 \leq 0.4$ %.

  - Error associated with BL^2 small contribution to overall error (30% of 1.3% = 0.4 % systematic).

- Local B - field known to $\Delta B \leq \pm 0.18$ T (about $\pm$ 20 %).

  - Dependent on L-angle (above for $\theta_L = 8^0$).
  - Tighter criterion for larger L-angle.
  - More simulation needed.

Local requirement probably satisfied by global requirement.

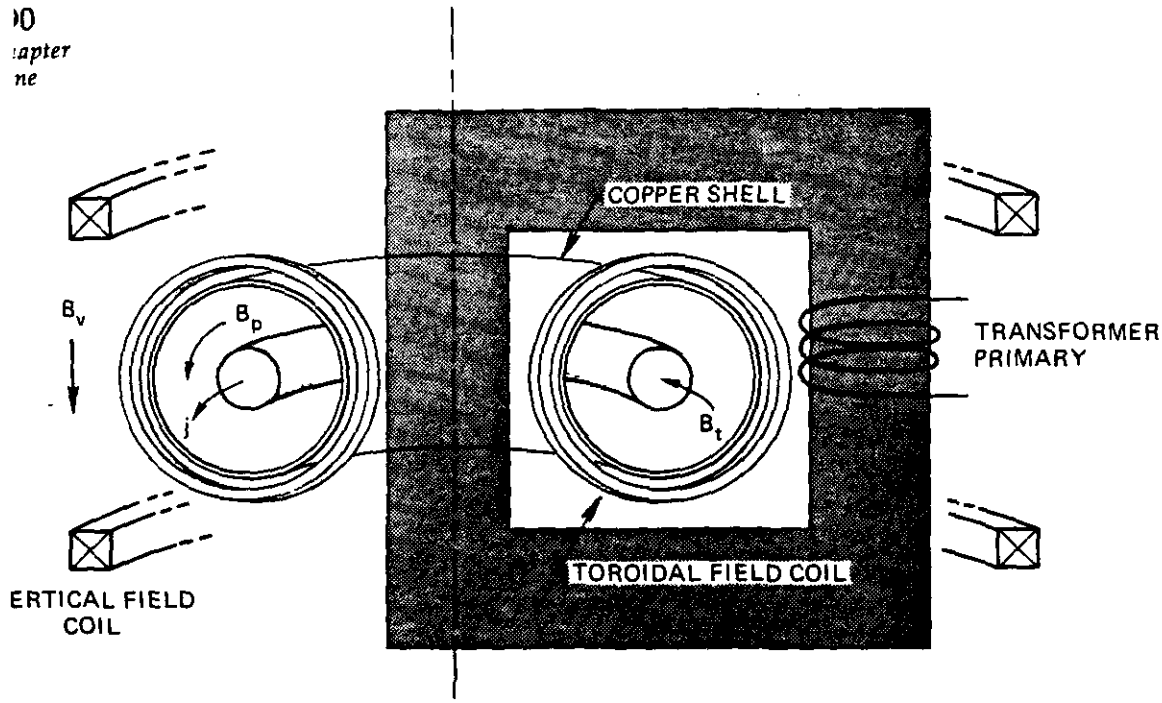

FIGURE 9-6 In a tokamak, the toroidal field component B_t is produced by the ordinary type of coils, while the poloidal component B_p is produced by a large plasma current induced by a transformer. Additional stabilizing forces are provided by a weak vertical field B_v and by eddy currents in a highly conducting copper shell.

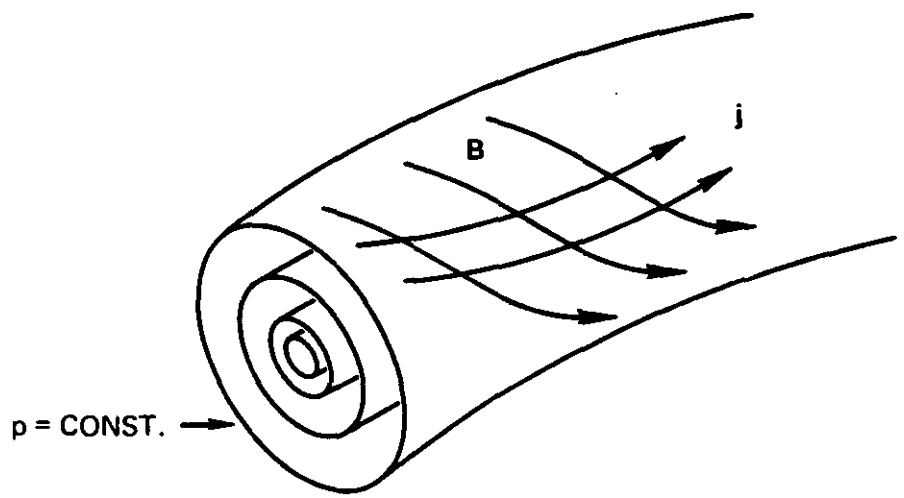

FIGURE 6-3 Both the j and B vectors lie on constant-pressure surfaces.

- MHD Equilibrium Equations

$$\left.\begin{aligned} \nabla\cdot\underline{B} &= 0 \\ \nabla\times\underline{B} &= \mu_0 \underline{J} \end{aligned}\right\} \text{Maxwell's equ}$$

and

$$\underline{J}\times\underline{B} = \nabla p \quad \text{Force balance}$$

- Tokamak is axisymmetric $\left(\frac{\partial}{\partial\varphi} \equiv 0\right)$

$$\therefore \underline{B}_p = \nabla\times\underline{A}_\varphi = \nabla\times\frac{1}{R}\psi\,\hat{\varphi}$$

$\psi \equiv$ poloidal flux functio

- Substitute ψ back into MHD eq's + combine together to get Grad-Shafranov equ for $\psi(R,Z)$.
- 2nd order, elliptic, non-linear boundary value problem (need $\psi + \frac{\partial\psi}{\partial n}$

in Fig. 15. Here R,ϕ,Z describe the usual right-handed cylindrical coordinate system. The assumption of toroidal axisymmetry implies that $\partial/\partial\phi=0$. It then follows from $\nabla\cdot\mathbf{B}=0$ that $\mathbf{B}$ can be written as

$$\mathbf{B}=B_\phi\mathbf{e}_\phi+\mathbf{B}_p,\quad \mathbf{B}_p=\frac{1}{R}\nabla\psi\times\mathbf{e}_\phi\,, \tag{4.30}$$

where B_ϕ is the toroidal field, B_p is the poloidal field, and $\psi/R=A_\phi$, the toroidal component of the vector potential. It can also be easily shown that the poloidal flux ψ_p is related to ψ by $\psi_p=2\pi\psi$. In axisymmetric tori it is convenient to label the magnetic flux surfaces with ψ rather than the pressure p.

Substituting Eq. (4.30) into Ampere's law yields

$$\mathbf{J}=-\frac{1}{R}\Delta^*\psi\mathbf{e}_\phi+\frac{1}{R}\nabla(RB_\phi)\times\mathbf{e}_\phi\,, \tag{4.31}$$

where Δ^* is the elliptic operator given by

$$\Delta^*\psi\equiv R\frac{\partial}{\partial R}\left[\frac{1}{R}\frac{\partial\psi}{\partial R}\right]+\frac{\partial^2\psi}{\partial Z^2}\,. \tag{4.32}$$

The last step in the derivation is to substitute Eqs. (4.30) and (4.31) into the momentum equation [Eq. (4.1)]. An efficient way to do this is to decompose Eq. (4.1) into three components, along $\mathbf{B}$, $\mathbf{J}$, and $\nabla\psi$ (normal to the flux surface). The $\mathbf{B}$ component gives $\mathbf{B}\cdot\nabla p=0$ or $\mathbf{e}_\phi\cdot\nabla\psi\times\nabla p=0$. As expected, this implies that p is a surface quantity,

$$p=p(\psi)\,. \tag{4.33}$$

Similarly, the $\mathbf{J}$ component gives $\mathbf{J}\cdot\nabla p=0$ or $\mathbf{e}_\phi\cdot\nabla\psi\times\nabla(RB_\phi)=0$, so that RB_ϕ is also a surface quantity,

$$RB_\phi=F(\psi)\,. \tag{4.34}$$

It can easily be shown that $F(\psi)=I_p/2\pi$, where I_p is the poloidal current passing through the surface bounded by $R=\text{const}$, $Z=0$.

The Grad-Shafranov equation is obtained by substituting these results into the $\nabla\psi$ component. The result is

$$\Delta^*\psi=-R^2\frac{dp}{d\psi}-F\frac{dF}{d\psi}\,. \tag{4.35}$$

Equation (4.35) is a second-order nonlinear partial differential equation describing axisymmetric toroidal equilibria. The nature of the equilibria (i.e., tokamak, reversed field pinch, etc.) is to a large extent determined by the choice of the two free functions $p(\psi)$ and $F(\psi)$ and, of course, the boundary conditions. These issues are discussed in more detail on an individual basis in later sections.

Consider now the macroscopic plasma parameters β and q. There is no unique definition of β which is simultaneously meaningful in all geometries and simple to evaluate. The different definitions, which usually are not too dissimilar from each other or Eq. (4.21), are also discussed on an individual basis.

On the other hand, the safety factor q is uniquely defined and can be calculated as follows. The equation for a magnetic field line in toroidal coordinates r,θ,ϕ defined by (see Fig. 15)

$$R=R_0+r\cos\theta,\quad Z=r\sin\theta \tag{4.36}$$

can be expressed as

$$\frac{Rd\phi}{B_\phi}=\frac{dr}{B_r}=\frac{rd\theta}{B_\theta}=\frac{dl}{B_p}\,, \tag{4.37}$$

where $dl=[(dr)^2+(rd\theta)^2]^{1/2}$ is the poloidal arc length and $B_p=(B_r^2+B_\theta^2)^{1/2}=|\nabla\psi|/R$ is the poloidal magnetic field. As the magnetic line wraps exactly once around the poloidal cross section, the toroidal angle $\Delta\phi$ along which it travels is given by

$$\Delta\phi=\int_0^{\Delta\phi}d\phi=\int_0^{2\pi}\left[\frac{rB_\phi}{RB_\theta}\right]_S d\theta\,. \tag{4.38}$$

Thus the average fractional poloidal transit per single toroidal transit is just $\iota=2\pi(2\pi/\Delta\phi)$, the rotational transform. The safety factor $q=2\pi/\iota$ then has the form

$$q(\psi)=\frac{1}{2\pi}\int_0^{2\pi}\left[\frac{rB_\phi}{RB_\theta}\right]_S d\theta=\frac{F(\psi)}{2\pi}\int\frac{dl}{R^2B_p}\,. \tag{4.39}$$

In Eqs. (4.38) and (4.39) the integrals are to be evaluated on the flux surface on which the magnetic line lies.

Because of the nonlinearity, the Grad-Shafranov equation must in general be solved numerically. Most of the major fusion laboratories around the world have developed such codes. They can be used for essentially arbitrary $p(\psi)$ and $F(\psi)$, as well as for rather sophisticated boundary conditions. Examples of these numerical equilibria are presented later.

However, from the point of view of obtaining physical understanding, it is perhaps more instructive to perform asymptotic analysis of the Grad-Shafranov equation. The simplifications that arise often permit analytic solu-

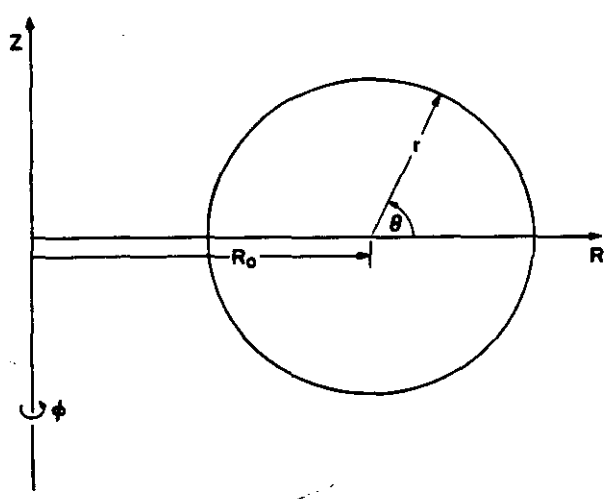

FIG. 15. Axisymmetric toroidal geometry.

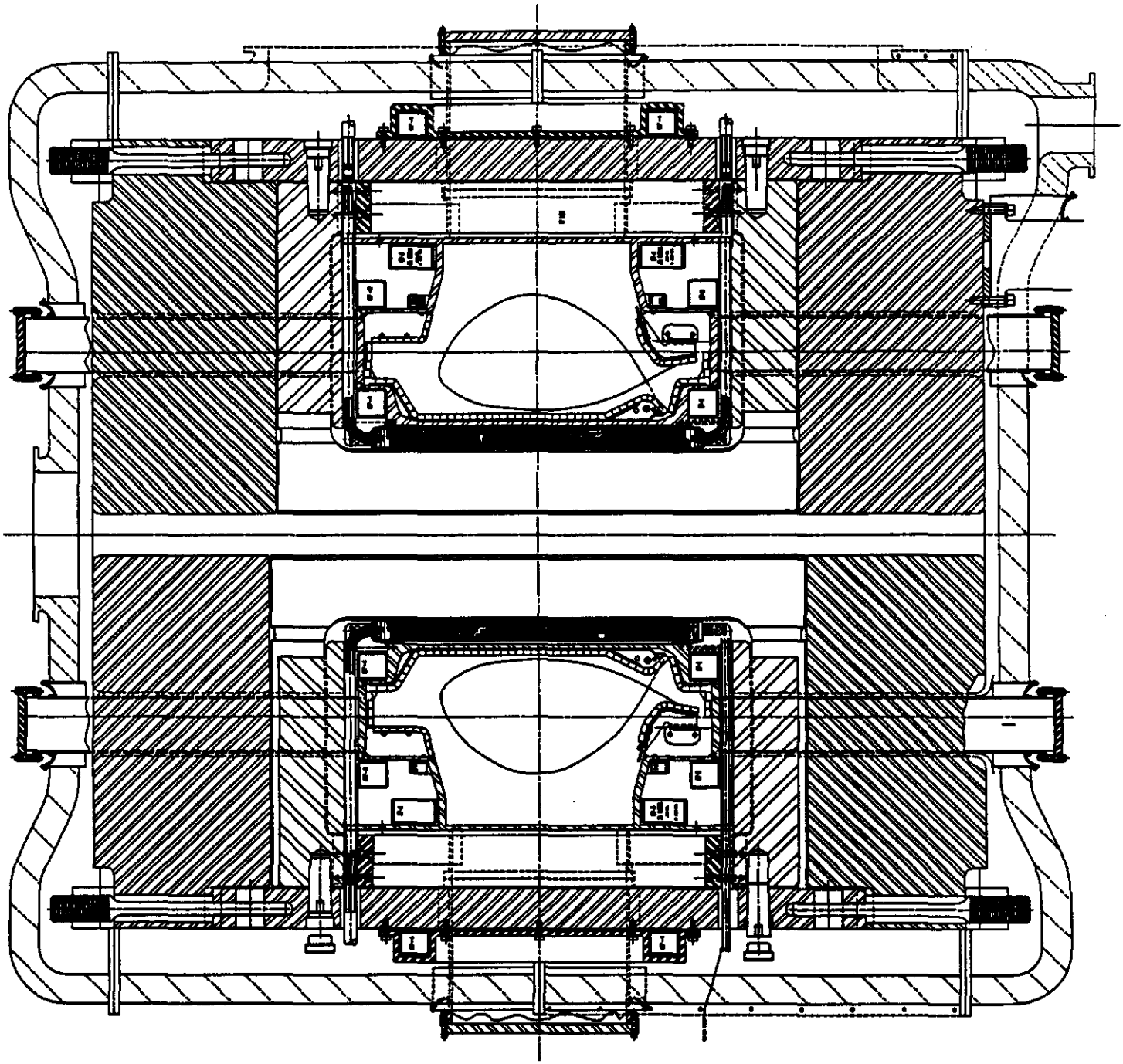

Bp coils 03-OCT-1991

(4 toroidal locations)

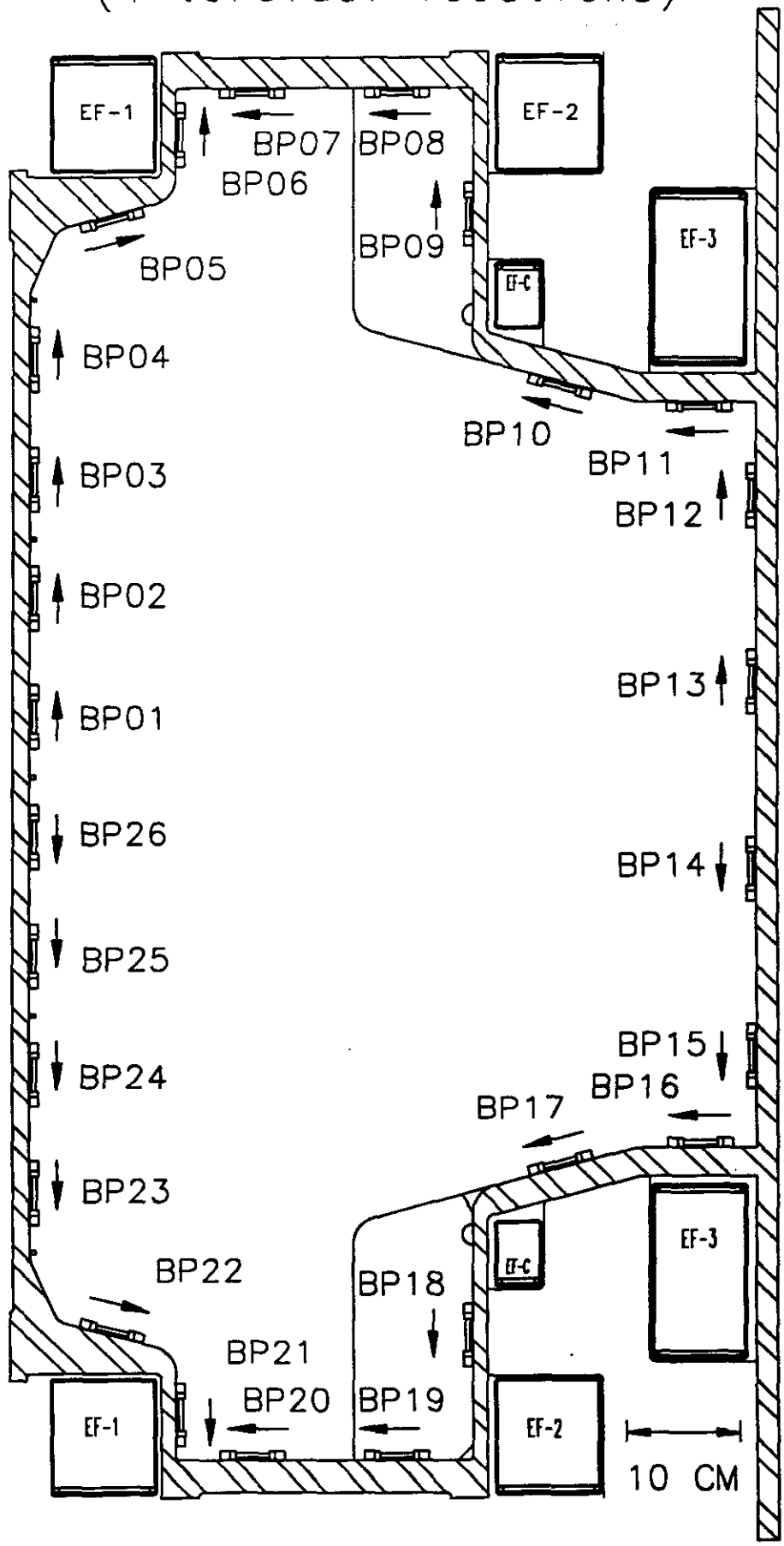

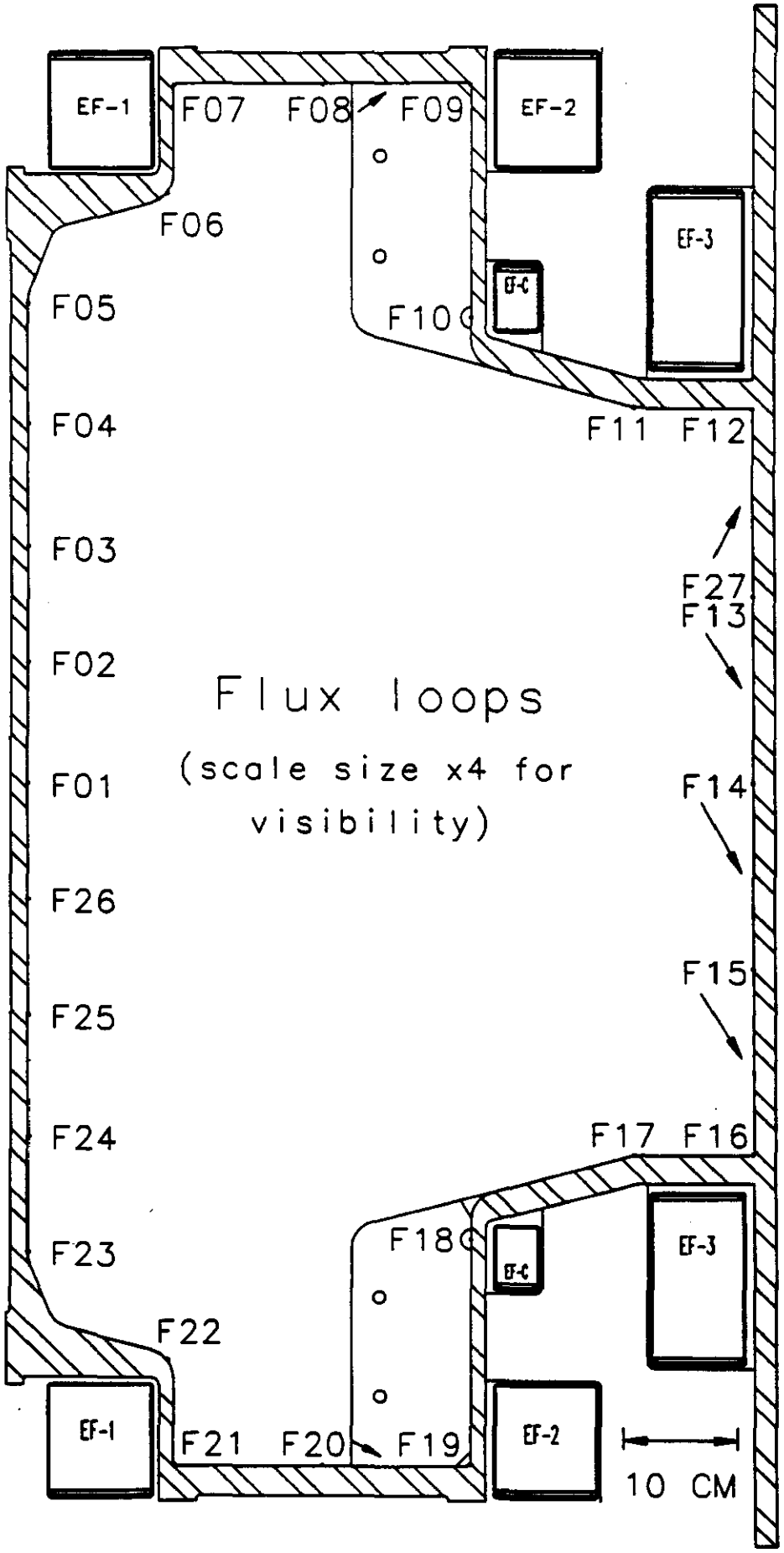
EF-1
F07
F08
F09
EF-2
F06
EF-3
EF-C
F05
F10
F04
F11
F12
F03
F27
F13
F02
Flux loops
(scale size x4 for visibility)
F01
F14
F26
F15
F25
F24
F17
F16
F23
F18
EF-C
EF-3
F22
EF-1
F21
F20
F19
EF-2
10 CM

Alcator C-MOD Magnetics Instrumentation

Sensor	Toroidal #	Poloidal #	Total elements	Measurement/ purpose
Rogowski coils	3	2 (halves)	6	plasma current, feedback control
B_p coils	4 arrays	26 per array	104	B poloidal, equilibrium reconstr., feedback control
Flux loops			29	poloidal flux, equilibrium reconstr., feedback control
(full)	—	21		
(partial)	1	6		
(1/10-partial)	1	2		
Mirnov array	6	10	16	Edge fluctuations
Diamagnetics				
main loop	2	—	2	plasma pressure, kinetic energy
compensation	2	2(×2)	8	
Saddle coils	4	1	4	'locked' modes
		Total	169	

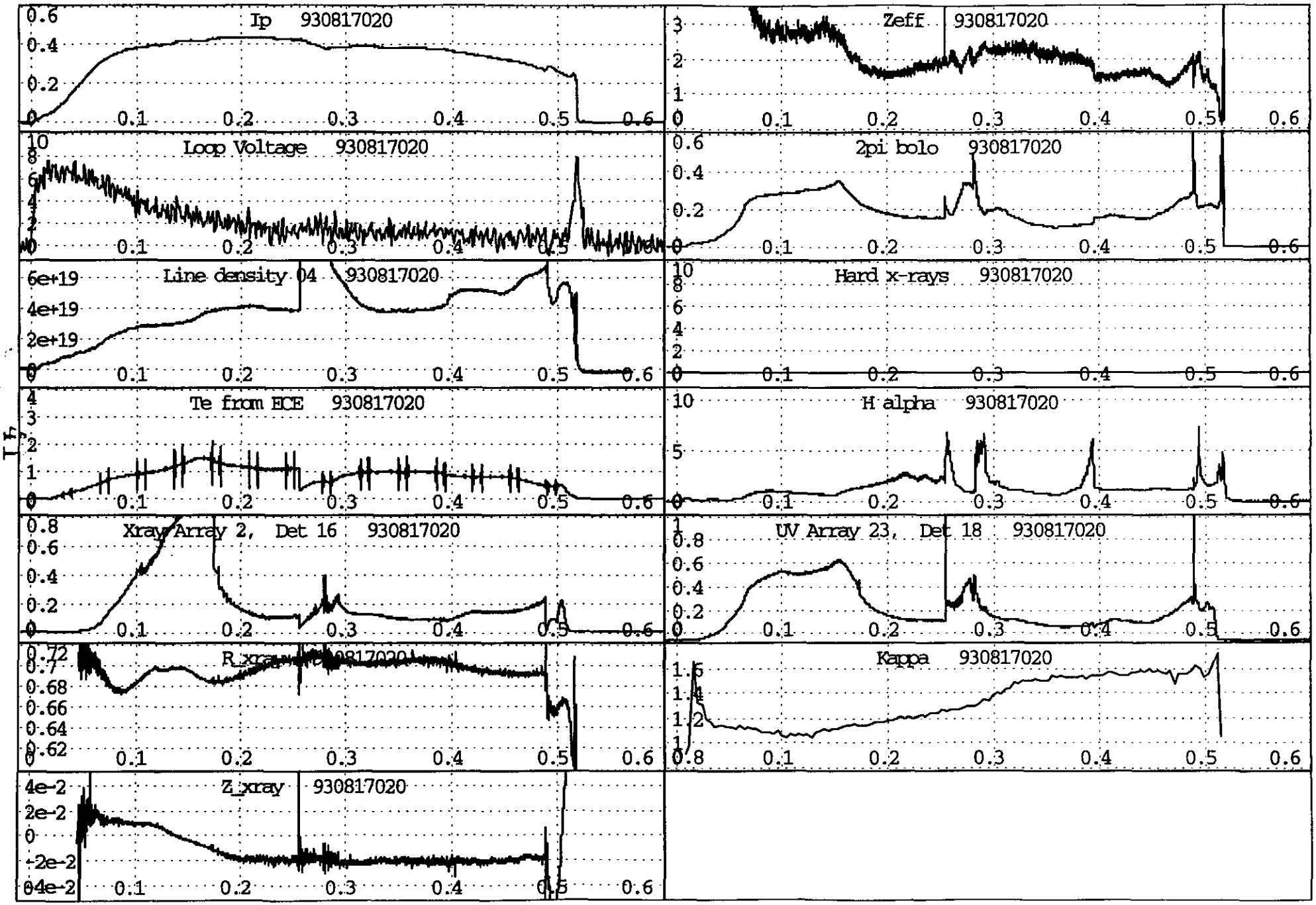
Ip 930817020
Zeff 930817020
Loop Voltage 930817020
2pi bolo 930817020
Line density 04 930817020
Hard x-rays 930817020
Te from ECE 930817020
H alpha 930817020
Xray Array 2, Det 16 930817020
UV Array 23, Det 18 930817020
R xray 930817020
Kappa 930817020
Z xray 930817020

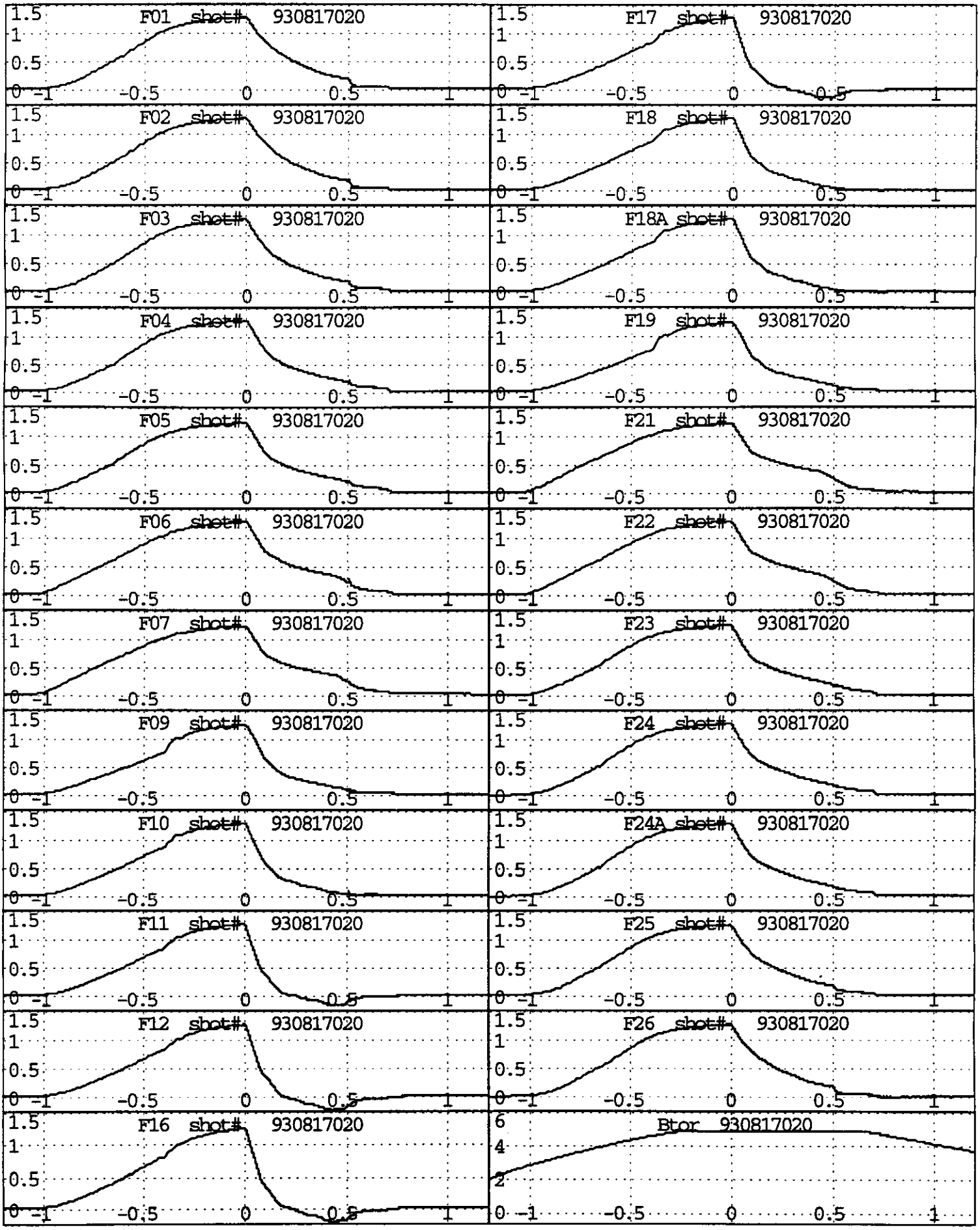
F01 shot# 930817020
F02 shot# 930817020
F03 shot# 930817020
F04 shot# 930817020
F05 shot# 930817020
F06 shot# 930817020
F07 shot# 930817020
F09 shot# 930817020
F10 shot# 930817020
F11 shot# 930817020
F12 shot# 930817020
F16 shot# 930817020
F17 shot# 930817020
F18 shot# 930817020
F18A shot# 930817020
F19 shot# 930817020
F21 shot# 930817020
F22 shot# 930817020
F23 shot# 930817020
F24 shot# 930817020
F24A shot# 930817020
F25 shot# 930817020
F26 shot# 930817020
Btor 930817020

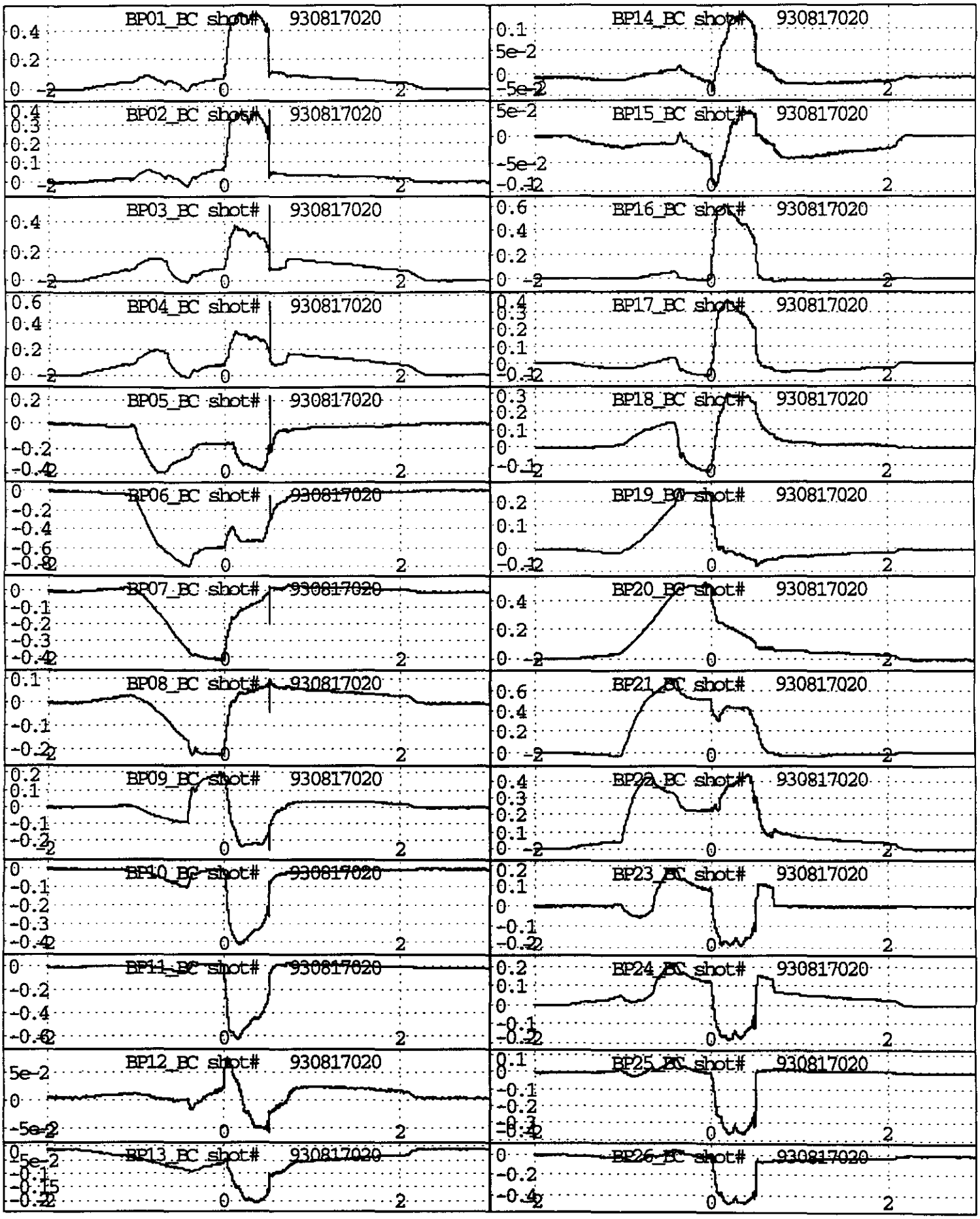
BP01_BC shot# 930817020
BP02_BC shot# 930817020
BP03_BC shot# 930817020
BP04_BC shot# 930817020
BP05_BC shot# 930817020
BP06_BC shot# 930817020
BP07_BC shot# 930817020
BP08_BC shot# 930817020
BP09_BC shot# 930817020
BP10_BC shot# 930817020
BP11_BC shot# 930817020
BP12_BC shot# 930817020
BP13_BC shot# 930817020
BP14_BC shot# 930817020
BP15_BC shot# 930817020
BP16_BC shot# 930817020
BP17_BC shot# 930817020
BP18_BC shot# 930817020
BP19_BC shot# 930817020
BP20_BC shot# 930817020
BP21_BC shot# 930817020
BP22_BC shot# 930817020
BP23_BC shot# 930817020
BP24_BC shot# 930817020
BP25_BC shot# 930817020
BP26_BC shot# 930817020

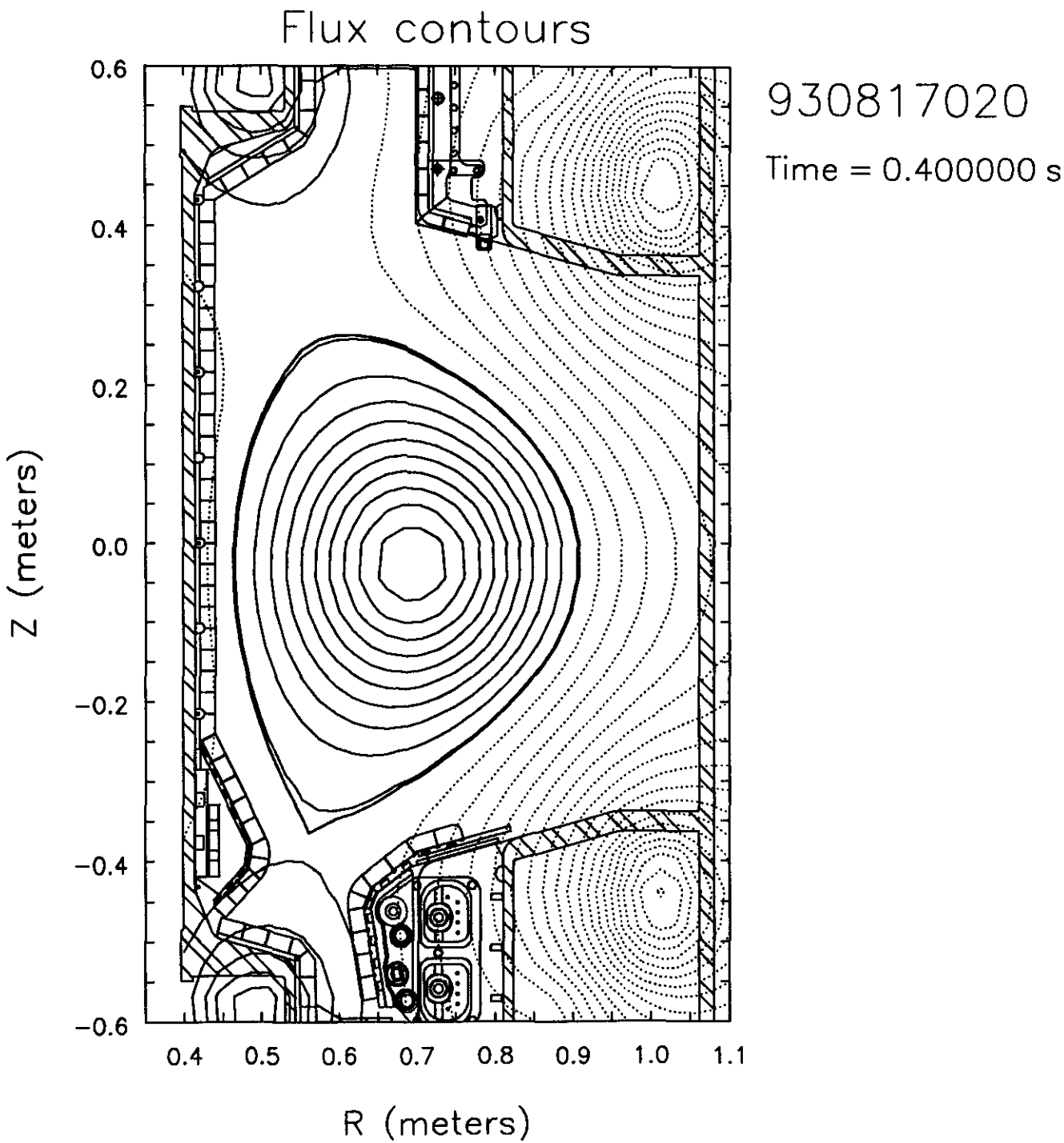
Flux contours
930817020
Time = 0.400000 s
Z (meters)
R (meters)
0.6
0.4
0.2
0.0
−0.2
−0.4
−0.6
0.4
0.5
0.6
0.7
0.8
0.9
1.0
1.1

A Scholarly Discourse on the Problem of Plasma Surface Reconstruction from Magnetic Data

J. P. Freidberg

MIT

June 1991

Collaborators:

S. P. Hakkarainen

B. Lane

S. Horne

J. Wei

R. Betti

Introduction

1. The problem:

   Given:

   A. A toroidal plasma surrounded by a vacuum chamber

   B. Poloidal magnetic data on the vacuum chamber

   C. Vacuum between wall and plasma edge

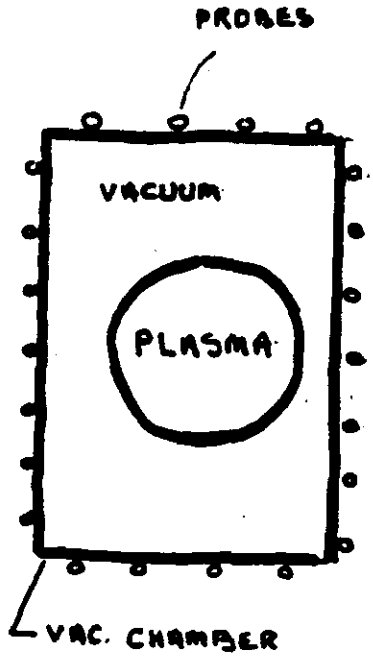

   Find:

   A. The shape of the plasma surface

   B. The poloidal magnetic field on the surface

2. This is a classic problem

3. Problem is inherently ill posed math[illegible]

Outline

1. Formulate the problem mathematically
2. Discuss problems
   A. Industrial strength ill posedness
   B. The dangers of Macho-matics
3. New, improved method of solution
   A. A surprisingly practical application of Green's theorem
4. Application to real experiments: Alcator C-Mod

Mathematical Formulation

1. Geometry

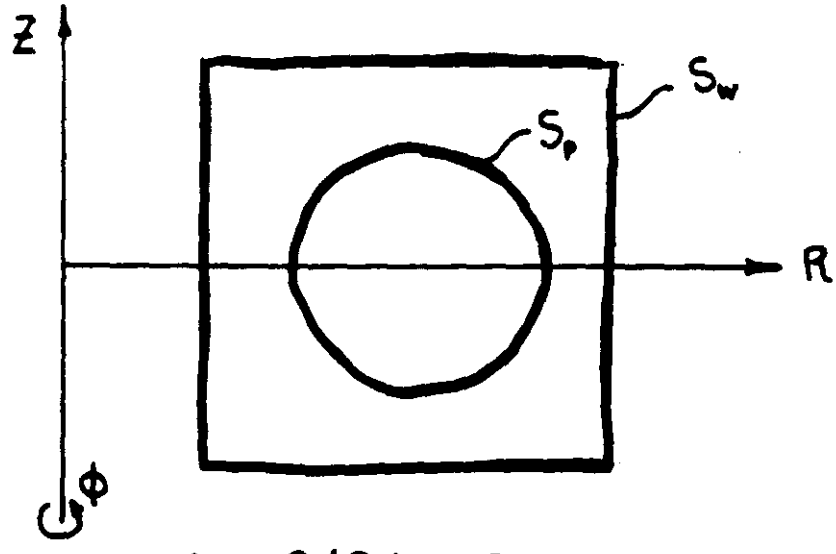

2. Axisymmetric: $\partial/\partial\phi = 0$

3. In vacuum: $\nabla \cdot \mathbf{B} = 0$, $\nabla \times \mathbf{B} = 0$

4. Poloidal field: $\mathbf{B}_p = \nabla\psi \times \mathbf{e}_\phi/R$

5. Probes: measure $\psi(S_W)$,

   $B_t(S_W) = \mathbf{n} \cdot \nabla\psi(S_W)/R(S_W)$

6. Wall is *not* a perfect conductor

7. $\mathbf{n}, \mathbf{t} \rightarrow$ vacuum chamber, not flux surfaces

8. Mathematics problem

Given: $\boxed{S_W, \psi(S_W), \partial\psi(S_W)/\partial n}$

Solve: $\boxed{\Delta^*\psi = 0}$

$$\Delta^*\psi \equiv R^2\nabla \cdot (\nabla\psi/R^2)$$

Find: $\boxed{S_p, \psi(S_p), \partial\psi(S_p)/\partial n}$

9. This is

   A. An elliptic PDE

   B. With Cauchy BC

10. Classic example of an ill conditioned problem

Industrial Strength Ill Posedness

Consider several simple examples

I1. Well posed problem

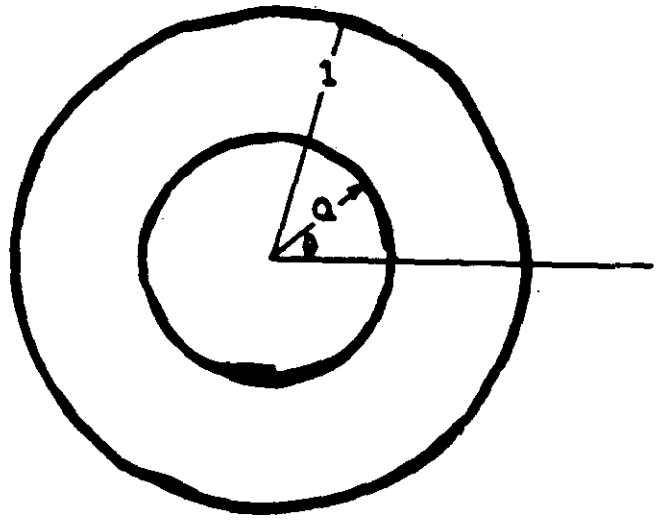

$$\nabla^2\psi = 0$$

$$\psi(1,\theta) = 0$$

$$\frac{\partial\psi}{\partial r}(a,\theta) = \frac{1}{a}\cos m\theta$$

2. Find $\psi(r,\theta)$, evaluate $\psi(a,\theta)$

$$\psi(r,\theta) = \frac{1}{m}\left(\frac{r^m - r^{-m}}{a^m + a^{-m}}\right)\cos m\theta$$

$$\boxed{\psi(a,\theta) = -\frac{1}{m}\left(\frac{1-a^{2m}}{1+a^{2m}}\right)\cos m\theta}$$

3. This is our reference case

II1. Well posed problem with error in data

$$\nabla^2\psi = 0$$

$$\psi(1,\theta) = \underline{\delta \cos m\theta}$$

$$\frac{\partial\psi}{\partial r}(a,\theta) = \frac{1}{a}\cos m\theta$$

2. $\delta \ll 1$ represents a small error

3. Solution:

$$\boxed{\psi(a,\theta) = -\left[\frac{1}{m}\frac{1-a^{2m}}{1+a^{2m}} - \underline{\frac{2a^m\delta}{1+a^{2m}}}\right]\cos m\theta}$$

4. Error: $E \sim 1 + ma^m\delta$

5. Moral: Well posed problems are more than fair.

An error δ on S_W leads to an exponentially small error $ma^m\delta$ on S_p

III1. Ill conditioned problem

$$\nabla^2\psi = 0$$

$$\psi(1,\theta) = 0$$

$$\frac{\partial\psi}{\partial r}(1,\theta) = \frac{2a^m}{1+a^{2m}}\cos m\theta$$

2. Solution: $\psi = \psi$ (reference)

$$\boxed{\psi(r,\theta) = \frac{1}{m}\left(\frac{r^m - r^{-m}}{a^m \quad a^{-m}}\right)\cos m\theta}$$

3. <u>Moral</u>: Ill conditioned problems of this class are OK if there is no error in the boundary data and the equations can be solved analytically (i.e. no numerical errors)

IV1. Ill conditioned problem with error in data

$$\nabla^2\psi = 0$$

$$\psi(1,\theta) = \underline{\delta \cos m\theta}$$

$$\frac{\partial\psi}{\partial r}(1,\theta) = \frac{2a^m}{1+a^{2m}} \cos m\theta$$

2. Solution:

$$\boxed{\psi(a,\theta) = -\left[\frac{1}{m}\left(\frac{1-a^{2m}}{1+a^{2m}}\right) - \left(\frac{1+a^{2m}}{2a^m}\right)\delta\right]\cos m\theta}$$

3. Error: $E \sim 1 + m\delta/a^m$

4. <u>Moral</u>: Ill conditioned problems are unfair. An error δ on S_W leads to an exponentially large error $m\delta/a^m$ on S_p.

5. <u>Moral</u>: Error increases with surface spacing and m number. Large plasmas with low harmonic content in the BC.

V1. Ill conditioned problem, error in data, finite grid

$$\nabla^2\psi = 0$$

$\psi(1,\theta) =$

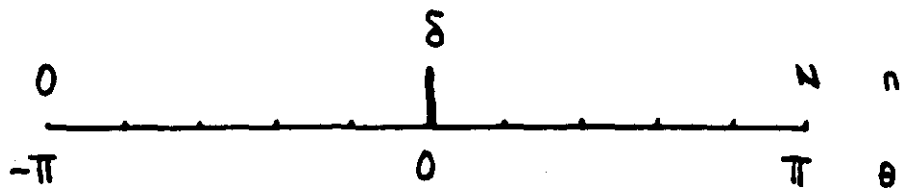

$$\frac{\partial\psi}{\partial r}(1,\theta) = \frac{2a^m}{1+a^{2m}}\cos m\theta$$

2. Fourier analyze

$$\psi = \tfrac{1}{2}\psi_0(r) + \sum_1^{N_T}\psi_n(r)\cos n\theta$$

$$\frac{d\psi_n(1)}{dr} = \begin{cases} \frac{2a^m}{1+a^{2m}} & n = m \\ 0 & n \neq m \end{cases}$$

$$\psi_n(1) = 2\delta/N$$

$0 \leq n \leq N_T$ $\qquad$ N_T = Fourier truncation

$N_T \leq N/2$ $\qquad$ N = number of θ intervals

3. Solution

$$\boxed{\psi(a,\theta) = -\frac{1}{m}\left(\frac{1-a^{2m}}{1+a^{2m}}\right)\cos m\theta + \frac{\delta}{N}\left[1+\sum_{1}^{N_T}\frac{1+a^{2n}}{a^n}\cos n\theta\right]}$$

4. Error: $E \sim 1 + \frac{m\delta}{Na^{N_T}}$

5. <u>Moral</u>: Error is largest when maximum harmonics are kept $N_T = N/2$

6. <u>Moral</u>: Truncate with less than full number of harmonics

7. <u>Moral</u>: Ideal truncation should be a function of spacing $N_T = N_T(a)$

VI1. Same problem, more realistic BC, optimal truncation

$$\nabla^2\psi = 0$$

$$\psi(1,\theta) = 0$$

$$\frac{\partial\psi}{\partial r}(1,\theta) = -\sum_1^\infty \frac{2na^n\epsilon^n}{1-a^{2n}}\cos n\theta$$

$\epsilon < 1 =$ inverse aspect ratio

2. Analytic solution

$$\psi(r,\theta) = \sum_1^\infty \frac{r^n - r^{-n}}{a^n - a^{-n}}\epsilon^n \cos n\theta$$

$$\boxed{\psi(a,\theta) = \sum_1^\infty \epsilon^n \cos n\theta \sim \frac{R_0}{R}}$$

VII1. Numerical problem with error in data

$$\nabla^2\psi = 0$$

$\psi(1,\theta) =$

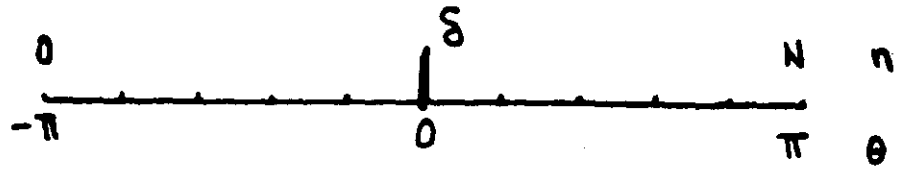

$$\frac{\partial\psi}{\partial r}(1,\theta) = -\sum_1^{N_T} \frac{2na^n\epsilon^n}{1-a^{2n}} \cos n\theta$$

2. Solution

$$\boxed{\psi(a,\theta) = \sum_1^{N_T} \epsilon^n \cos n\theta + \frac{\delta}{N}\left[1 + \sum_1^{N_T} \frac{1+a^{2n}}{a^n} \cos n\theta\right]}$$

3. Error: $E \equiv \langle(\psi_a - \psi_n)^2\rangle / \psi_{a\ max}^2$

$$E = \frac{1}{2}\frac{\epsilon^{2N_T}}{1-\epsilon^2} + \frac{\delta^2}{2\epsilon^2 N^2}\left[\frac{1-a^{2N_T}}{1-a^2}(a^{-2N_T} + a^2) + 2N_T + 2\right]$$

$$E \approx \frac{1}{2}\left[\epsilon^{2N_T} + \left(\frac{\delta}{\epsilon N}\right)^2 \frac{1}{a^{2N_T}}\right]$$

Ill posedness → small N_T

Resolution → large N_T

4. Optimum: $N_T \approx \frac{1}{\ln(\epsilon^2 a^2)} \ln\left(\frac{\delta^2}{\epsilon^2 N^2}\frac{\ln a^2}{\ln \epsilon^2}\right)$

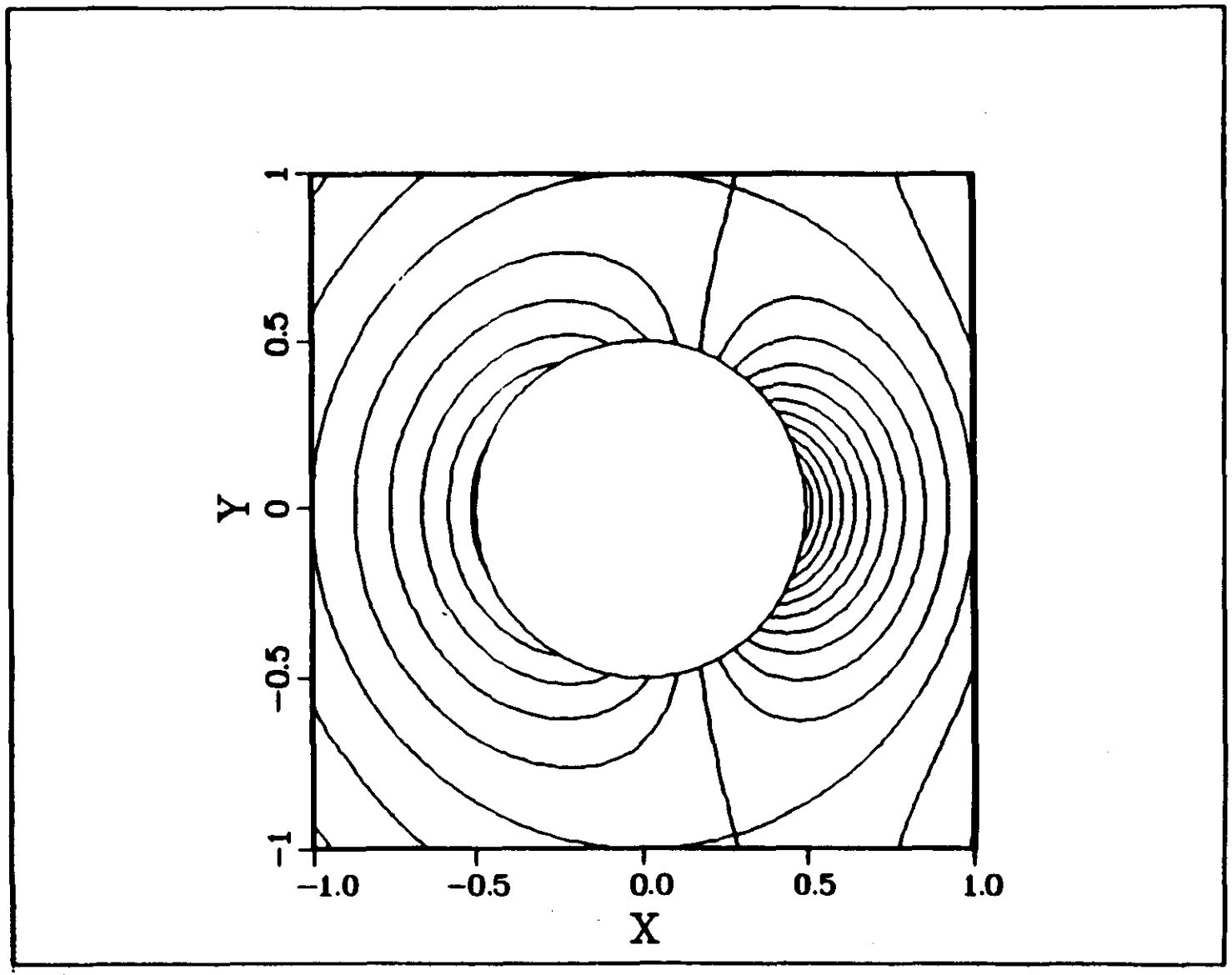

EXACT $\delta = 0$ 'scale'

X
Y
-1.0
-0.5
0.0
0.5
1.0
-1
-0.5
0
0.5
1

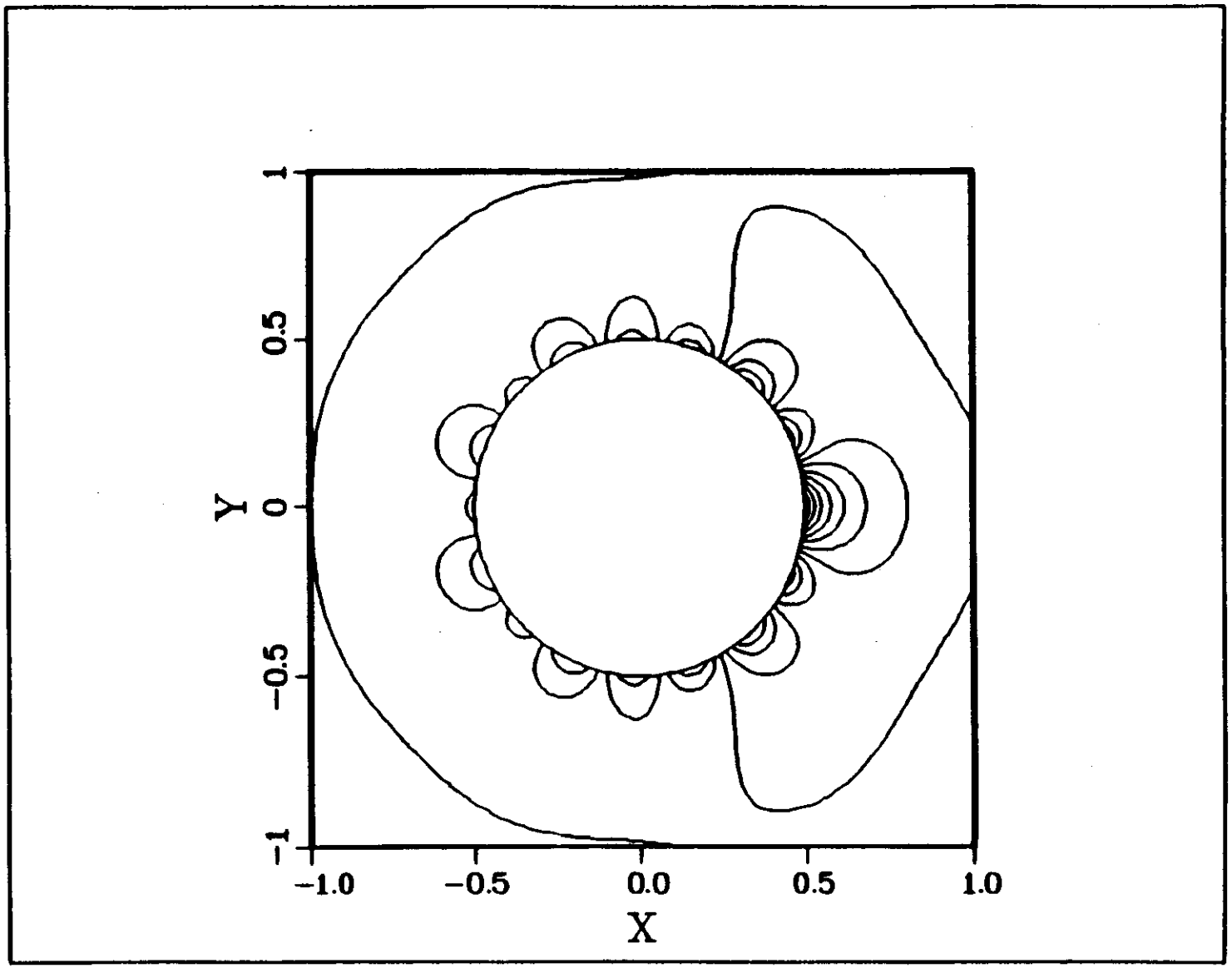

$N_T = 8$

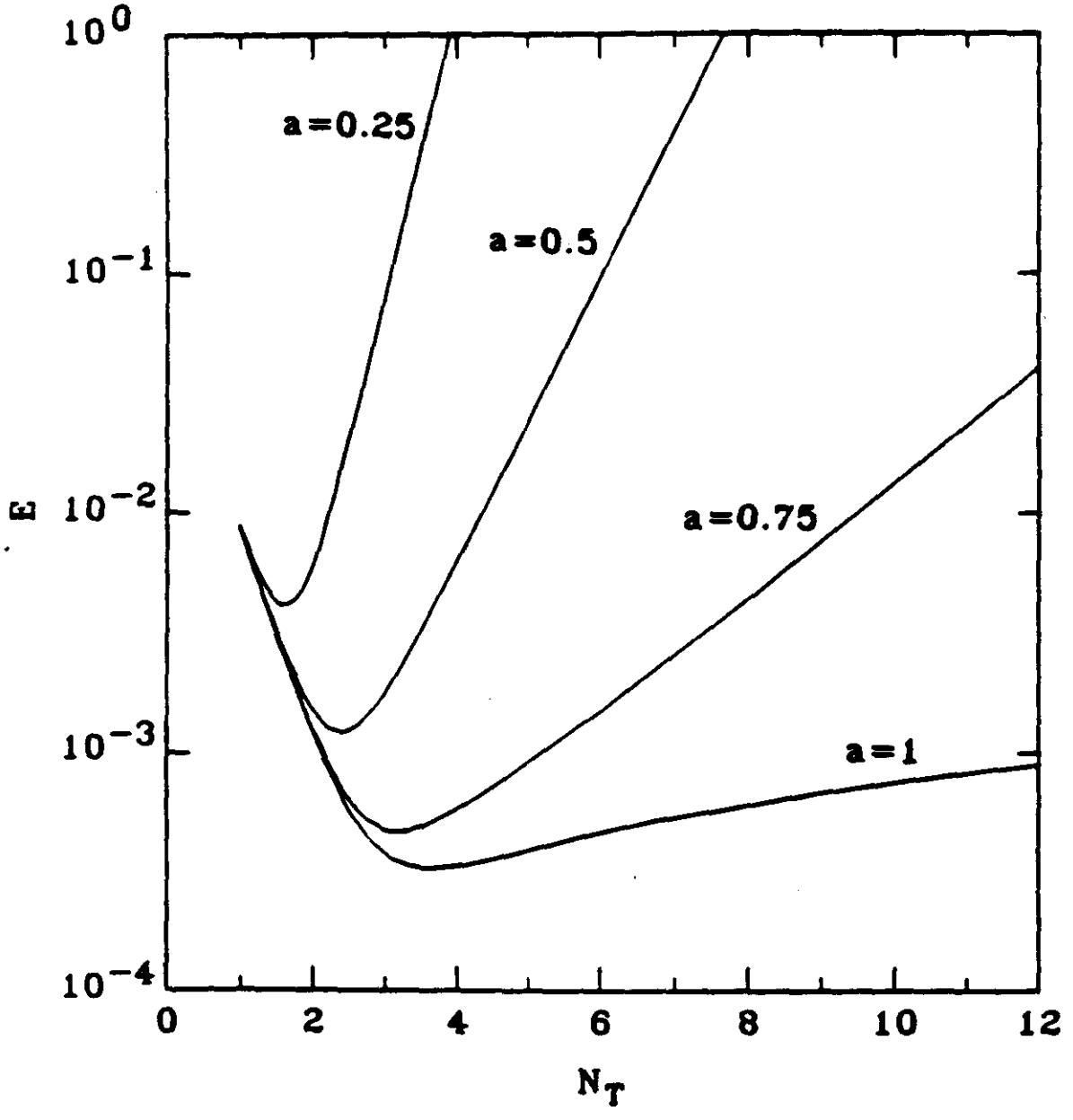
10^0
10^{-1}
10^{-2}
10^{-3}
10^{-4}
E
a=0.25
a=0.5
a=0.75
a=1
0
2
4
6
8
10
12
N_T

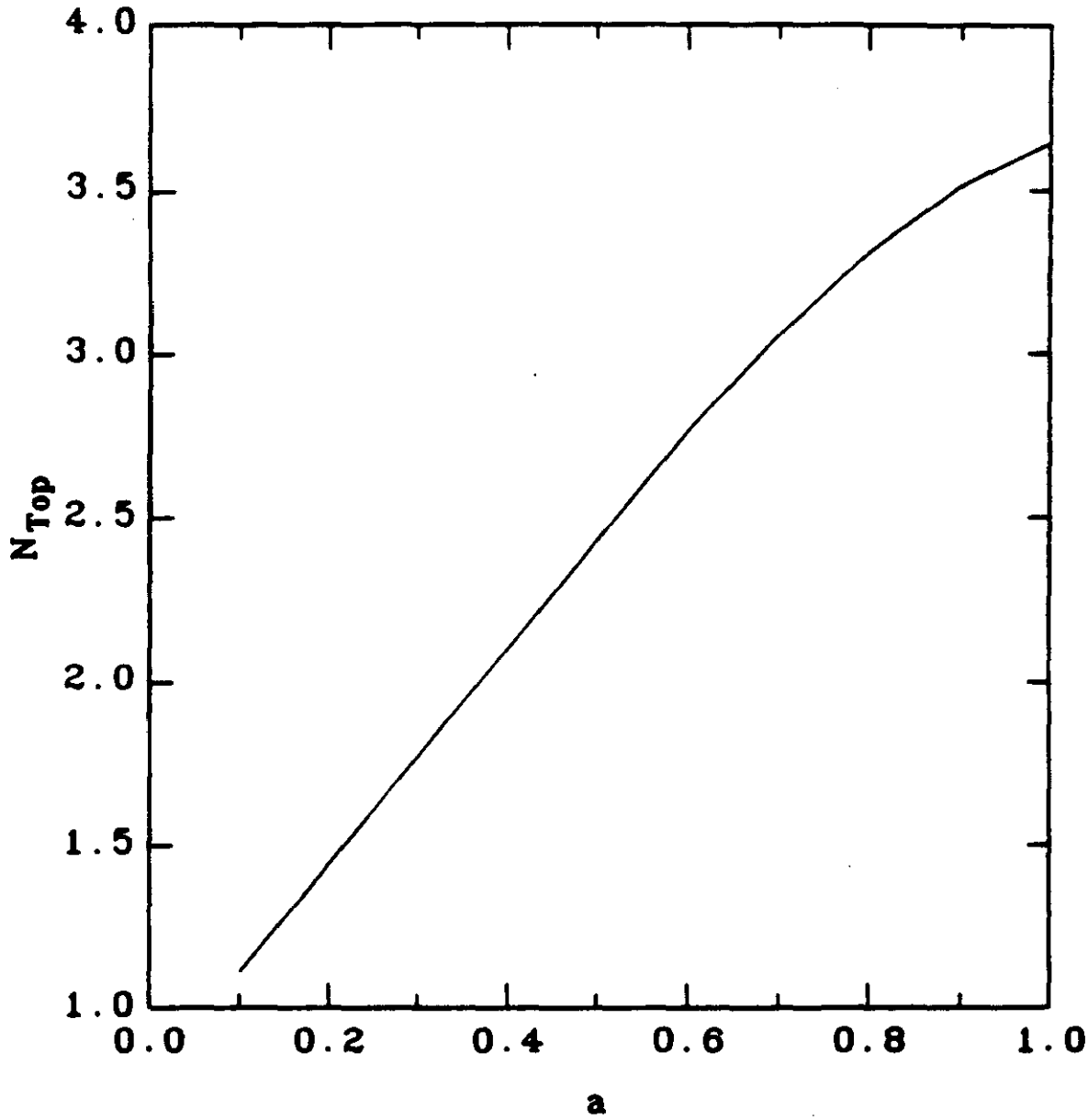
4.0
3.5
3.0
2.5
2.0
1.5
1.0
N_{Top}
0.0
0.2
0.4
0.6
0.8
1.0
a

The Dangers of Macho-matics

1. What is Macho-matics?

   The belief that any math problem can be solved by a combination of bravado, brute force and raw computing power

2. What is the challenge?

   Expansion techniques, using *un-natural* functions, should be a powerful way to solve the problem of interest

3. Plan

   A. Solve a simple problem using natural functions

   B. Generalize the procedure using un-natural functions

   C. Prove theoretically that (B) does not work in general

   D. You will not be convinced – (B) obviously must work

   E. Show what happens if (B) is implemented numerically

1. Simple problem – natural functions

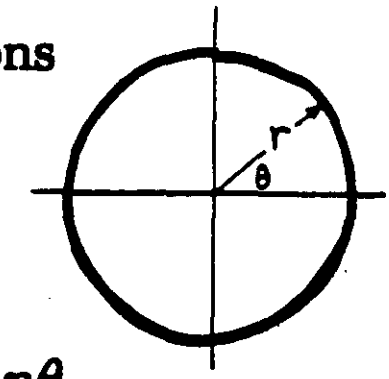

$\nabla^2\psi = 0$

$\psi(\infty, \theta) = 0$

$\frac{\partial\psi}{\partial r}(1, \theta) = f(\cos\theta) = \sum_1^\infty A_n \cos n\theta$

2. Natural functions: $r^m \cos m\theta, r^{-m} \cos m\theta$

3. Natural because r = constant corresponds to the plasma boundary

4. Exact solution

$\psi = \sum_1^\infty a_n r^{-n} \cos n\theta$

$$\boxed{\overleftrightarrow{\mathbf{M}} \cdot \mathbf{a} = \mathbf{A}}$$

$$\begin{bmatrix} 1 & & & \\ & 2 & & \\ & & 3 & \\ & & & \ddots \end{bmatrix} \begin{bmatrix} a_1 \\ a_2 \\ a_3 \\ \vdots \end{bmatrix} = \begin{bmatrix} A_1 \\ A_2 \\ A_3 \\ \vdots \end{bmatrix}$$

$$a_n = -A_n/n$$

1. General procedure – un-natural functions

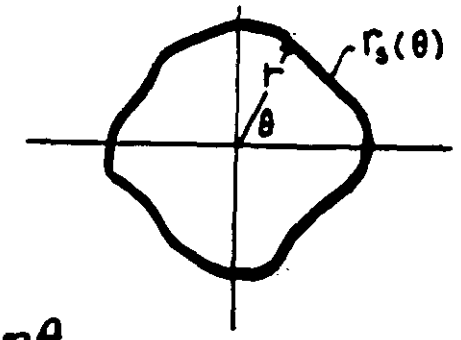

$$\nabla^2\psi = 0$$

$$\psi(\infty, \theta) = 0$$

$$\frac{\partial\psi}{\partial r}(r_s, \theta) = f(\cos\theta) = \sum_1^\infty A_n \cos n\theta$$

2. Solution regular at ∞, satisfying $\nabla^2\psi = 0$

$$\psi = \sum_1^\infty a_n r^{-n} \cos n\theta$$

3. Fourier analyze

$$\boxed{\overleftrightarrow{\mathbf{M}} \cdot \mathbf{a} = \mathbf{A}}$$

$$M_{mn} = \frac{1}{\pi}\int_0^{2\pi} r_s^{-n}(\theta) \cos n\theta \cos m\theta d\theta$$

4. Solution: $\mathbf{a} = \overleftrightarrow{\mathbf{M}}^{-1} \cdot \mathbf{A}$

5. Un-natural functions: r = constant is not the plasma boundary

1. Counter-example against the general procedure

2. Special case

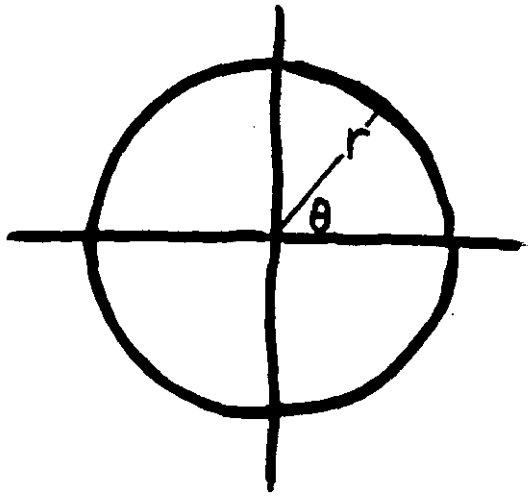

$$\nabla^2\psi = 0$$

$$\psi(\infty, \theta) = 0$$

$$\frac{\partial\psi}{\partial r}(1, \theta) = \cos\theta$$

$$\boxed{\psi(r, \theta) = -\frac{\cos\theta}{r}}$$

3. Shift coordinates by σ

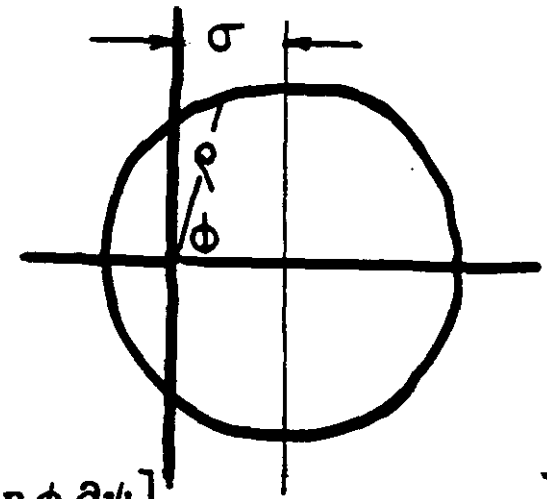

$$\nabla^2\psi = 0$$

$$\psi(\infty, \phi) = 0$$

$$\left[\frac{1}{\rho}(1 - \sigma^2 + \sigma\rho\cos\phi)\frac{\partial\psi}{\partial\rho} + \frac{\sigma\sin\phi}{\rho}\frac{\partial\psi}{\partial\phi}\right]_{\rho_s}$$

$$= \rho_s\cos\phi - \sigma$$

$$\rho_s^2(\phi) - 2\sigma\rho_s(\phi)\cos\phi = 1 - \sigma^2 \qquad \text{shifted circle}$$

4. Expand, satisfying BC at ∞ and $\nabla^2\psi = 0$

$$\boxed{\psi = \sum_1^\infty a_n \rho^{-n} \cos n\phi}$$

5. Exact solution

$$\psi = -\frac{\cos\theta}{r} = \frac{\sigma - \rho\cos\phi}{\rho^2 - 2\rho\sigma\cos\phi + \sigma^2}$$

6. But, using properties of Chebyshev polynomials

$$-\frac{\cos\theta}{r} = \frac{1}{\sigma}\sum_1^\infty \left(\frac{\sigma}{\rho}\right)^n \cos n\phi \qquad \sigma < \rho$$

$$-\frac{\cos\theta}{r} = \frac{1}{\sigma}\sum_0^\infty \left(\frac{\rho}{\sigma}\right)^n \cos n\phi \qquad \rho < \sigma$$

7. Expansion good if $\sigma < \rho$

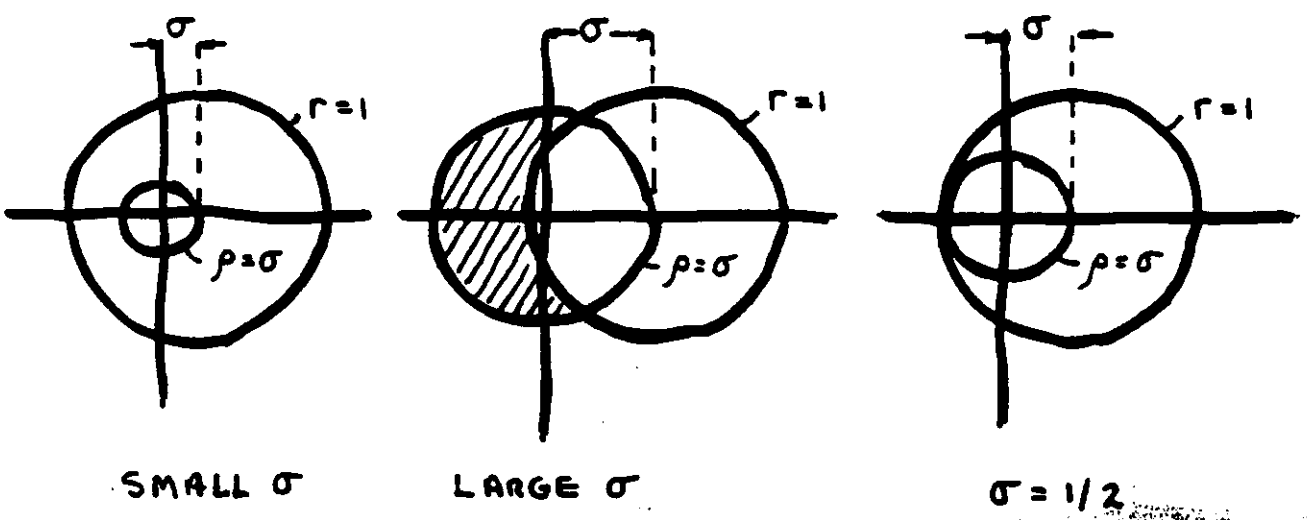

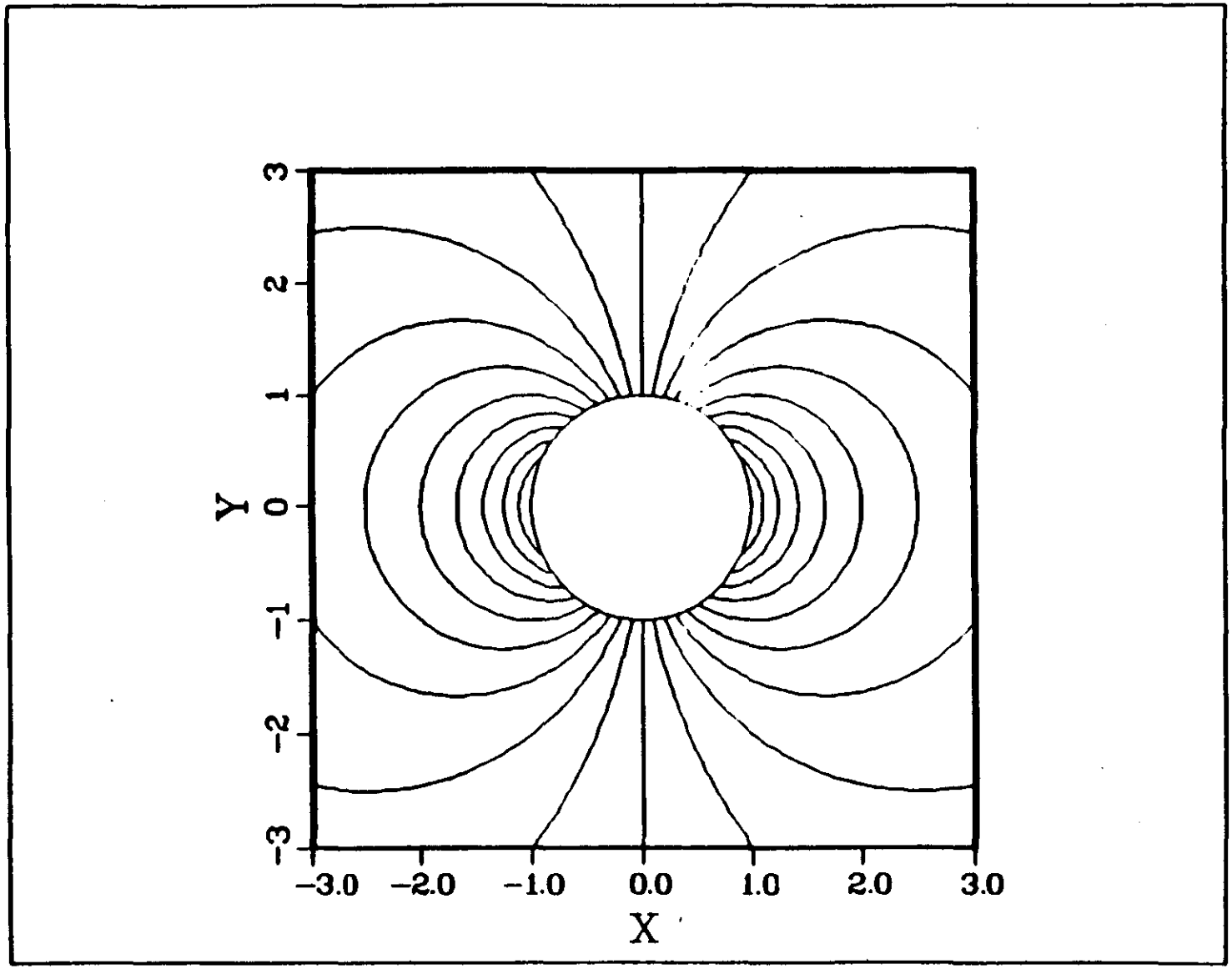

$\sigma = 0$

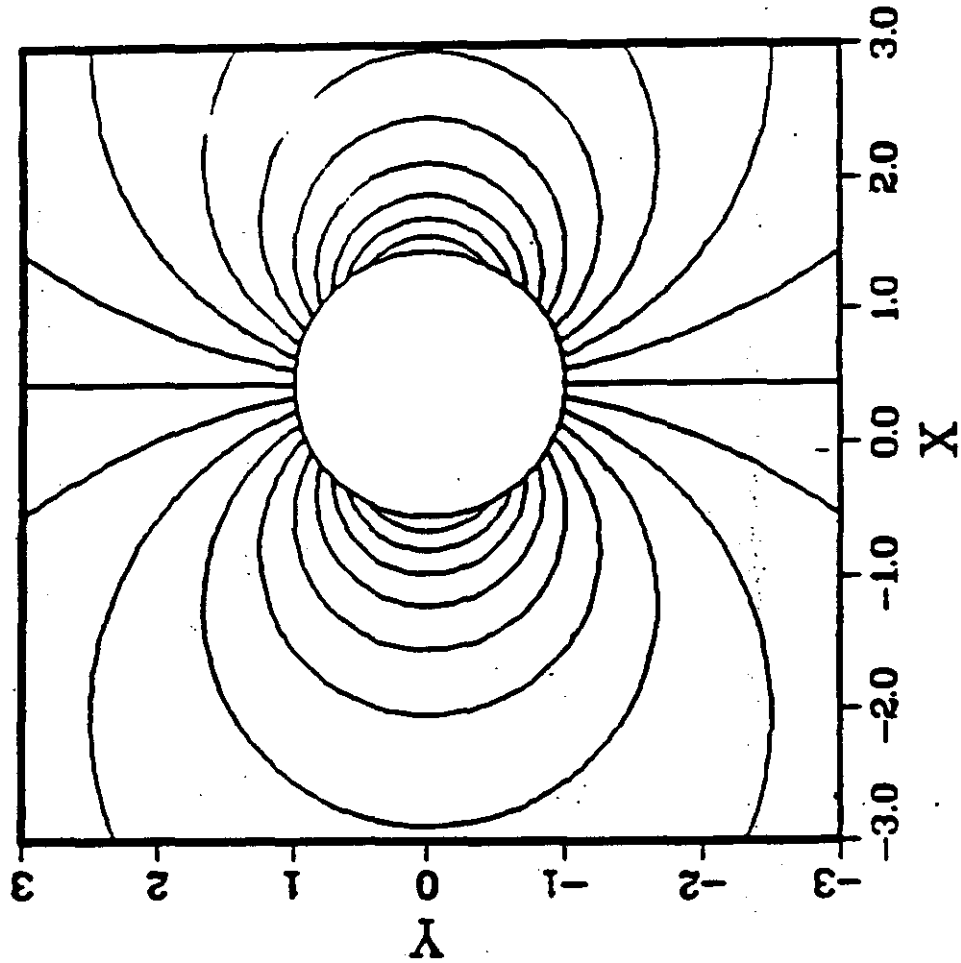
X
-3.0
-2.0
-1.0
0.0
1.0
2.0
3.0
Y
-3
-2
-1
0
1
2
3

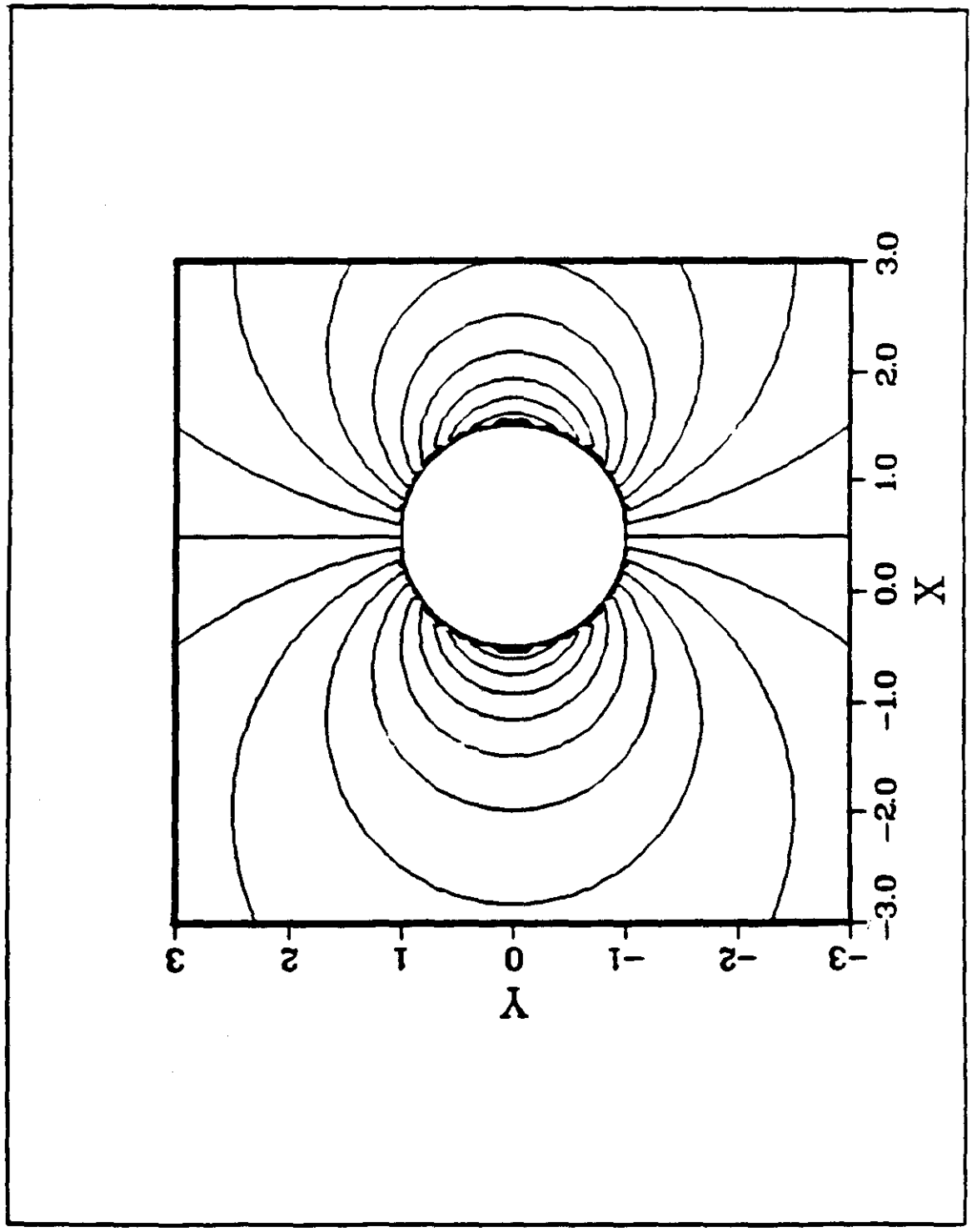

$\sigma = .51$

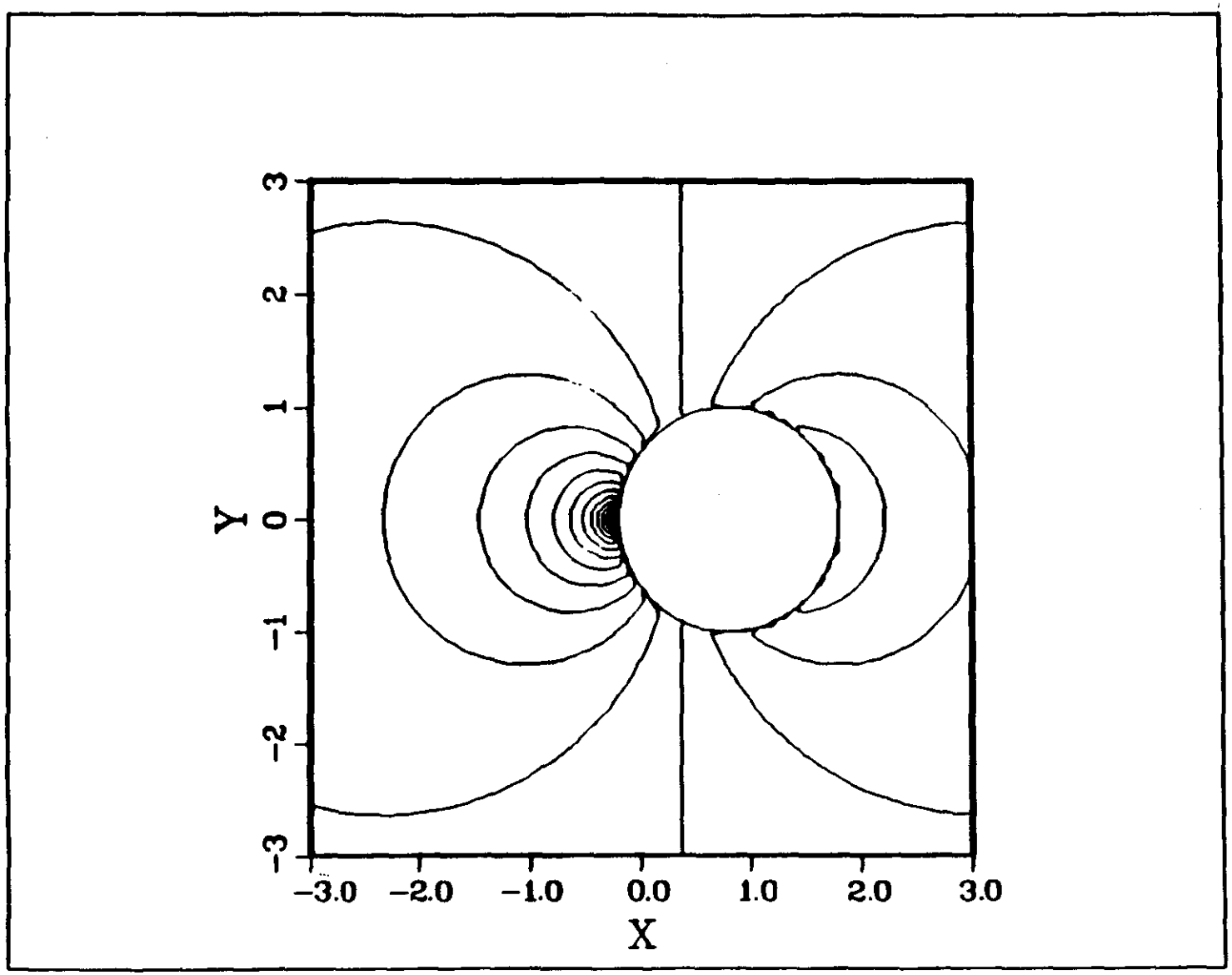

$\sigma = .8$

$\sigma = 0.8$

8. Expansion valid only if $\sigma < 1/2$, not $\sigma \leq 1$!!

9. Moral: For a good expansion, natural functions must be used

10. Moral: It is not possible to easily calculate the "effective σ" for a general cross section

11. Moral: For a general cross section there are not simple, separable, radial-like natural functions

Summary of Insights

1. Problem is easier if plasma is close to the wall: δ/a^m

2. Minimize high harmonic content in data: δ/a^m

3. Truncate Fourier series with $N_T < N/2$: δ/a^{N_T}

4. Optimal truncation: ill posedness vs resolution $N_T = N_T(a)$

5. Do not use un-natural radial expansion functions

New Improved Method of Solution

1. Basic Problem

   $\Delta^* \Psi = 0$

   $\Psi(S_W) = \text{given}$

   $\frac{\partial \Psi}{\partial n}(S_W) = \text{given}$

   Find $S_p, \Psi(S_p), \partial\Psi(S_p)/\partial n$

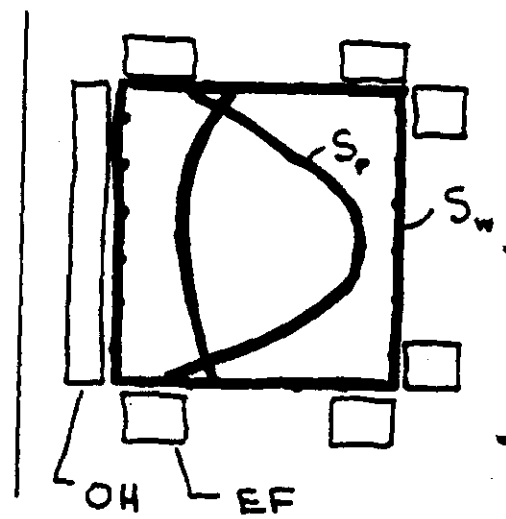

2. First, subtract contributions from PF and OH

   A. This eliminates high harmonics due to close coils

   B. Lowers the magnitude of the residual BC

3. Second, subtract contribution from "plasma filament" at R_0

   A. This can lead to high harmonics if S_W is complicated

4. After subtraction

$$\Psi = \sum_j \mu_0 I_j \Psi_j + \mu_0 I_p \Psi_p + \psi$$

$$\Psi_j = \frac{(RR_j)^{1/2}}{2\pi}\left[\frac{(2-k^2)K(k)-2E(k)}{k}\right] = \text{known}$$

5. Solve reduced problem

$$\boxed{\Delta^* \psi = 0}$$

$$\underline{\psi(S_W)} = \Psi(S_W) - \sum_j \mu_0 I_j \Psi_j(S_W)$$
$$-\mu_0 I_p \Psi_p(S_W) = \underline{\text{given}}$$

$$\underline{\frac{\partial\psi}{\partial n}(S_W)} = \frac{\partial\Psi}{\partial n}(S_W) - \sum_j \mu_0 I_j \frac{\partial\Psi_j}{\partial n}(S_W)$$
$$-\mu_0 I_p \frac{\partial\Psi_p}{\partial n}(S_W) = \underline{\text{given}}$$

6. Same problem as before, but with smaller and smoother boundary data

7. The solution procedure

   A. Define any convenient set of smooth calculation surfaces on which to evaluate the solution. These are *not* flux surfaces.

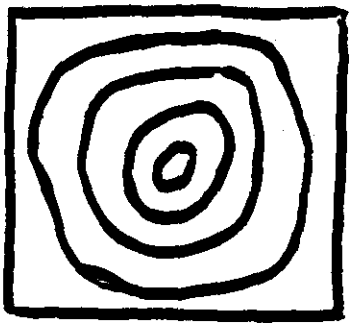

   B. Write down the vector Green's theorem in an axisymmetric torus

$$\boxed{\sigma\psi + \sum_s \int \left(\frac{\psi'}{R'} \frac{\partial H}{\partial n'} - \frac{H}{R'} \frac{\partial \psi'}{\partial n'} \right) dv' = 0}$$

$$H = -\frac{(RR')^{1/2}}{2\pi} \left[\frac{(2-k^2)K - 2E}{k} \right] = \text{known}$$

$\sigma = (1, 1/2, 0)$

$R = R(v), Z = Z(v)$: angle v parameterizes surface

v can be defined differently on each surface

C. Use Green's function twice: on S_c and S_W

$$\boxed{\begin{aligned}&\tfrac{1}{2}\psi_c + \int_{S_c}\left[\frac{\psi'_c}{R'_c}\frac{\partial H_{cc}}{\partial n'_c} - \frac{H_{cc}}{R'_c}\frac{\partial \psi'_c}{\partial n'_c}\right] dv' \\ &- \int_{S_W}\left[\frac{\psi'_W}{R'_W}\frac{\partial H_{Wc}}{\partial n'_W} - \frac{H_{Wc}}{R'_W}\frac{\partial \psi'_W}{\partial n'_W}\right] dv' = 0\end{aligned}}$$

$$\boxed{\begin{aligned}&\tfrac{1}{2}\psi_W + \int_{S_W}\left[\frac{\psi'_W}{R'_W}\frac{\partial H_{WW}}{\partial n'_W} - \frac{H_{WW}}{R'_W}\frac{\partial \psi'_W}{\partial n'_W}\right] dv' \\ &+ \int_{S_W}\left[\frac{\psi'_c}{R'_c}\frac{\partial H_{cW}}{\partial n'_c} - \frac{H_{cW}}{R'_c}\frac{\partial \psi'_c}{\partial n'_c}\right] dv' = 0\end{aligned}}$$

D. We know $\psi'_W, \partial\psi'_W/\partial n'_W$ from measurement data.

We know $H, \partial H/\partial n$ on each surface – Green's function

E. These equations are two equations in the two 1-D unknowns $\psi_c(v)$ and $\partial\psi_c(v)/\partial n$ evaluated on S_c

F. Solve these equations by means of a truncated Fourier series: $\mathbf{a}, \mathbf{b}$ unknown, $\hat{\mathbf{a}}, \hat{\mathbf{b}}$ known

$$\psi_c(v) = \sum_{-N_c}^{N_c} \underline{a_n} e^{inv} \qquad \psi_W = \sum_{-N_W}^{N_W} \underline{\hat{a}_n} e^{inv}$$

$$\frac{1}{R_c}\frac{\partial \psi_c(v)}{\partial n} = \sum_{-N_c}^{N_c} \underline{b_n} e^{inv} \quad \frac{1}{R_W}\frac{\partial \psi_W(v)}{\partial n} = \sum_{-N_W}^{N_W} \underline{\hat{b}_n} e^{inv}$$

G. This leads to a linear matrix problem

$$\overleftrightarrow{\mathbf{W}} \cdot \mathbf{Y} = \overleftrightarrow{\mathbf{V}} \cdot \mathbf{X}$$

$$\mathbf{Y} = \begin{pmatrix} \mathbf{a} \\ \mathbf{b} \end{pmatrix} \qquad \mathbf{X} = \begin{pmatrix} \hat{\mathbf{a}} \\ \hat{\mathbf{b}} \end{pmatrix}$$

H. The elements of $\overleftrightarrow{\mathbf{W}}$ and $\overleftrightarrow{\mathbf{V}}$ are the 2-D FFT of $H(v, v')$, $\partial H(v, v')/\partial n'$ on the various surfaces

I. $\overleftrightarrow{\mathbf{W}}$ and $\overleftrightarrow{\mathbf{V}}$ depend on the geometry of S_W and S_c, but not the data. They can be pre-calculated and stored. The solutions on the calculation surface are found by

$$\boxed{\begin{aligned} \mathbf{Y} &= \overleftrightarrow{\mathbf{M}} \cdot \mathbf{X} \\ \overleftrightarrow{\mathbf{M}} &= \overleftrightarrow{\mathbf{W}}^{-1} \cdot \overleftrightarrow{\mathbf{V}} \end{aligned}}$$

Summary of Procedure

1. Pre-calculate and store $\overleftrightarrow{\mathbf{M}}$ for each calculation surface. Typically $\overleftrightarrow{\mathbf{M}} < 20 \times 20$ and there are ten surfaces
2. Subtract PF, OH, and plasma filament contributions from the measurement data
3. Take FFT of reduced data: $\hat{\mathbf{a}}, \hat{\mathbf{b}}$
4. Multiply by $\overleftrightarrow{\mathbf{M}}$ for each surface: $\mathbf{a}, \mathbf{b}$
5. Compute $\Psi = \Psi_{PF} + \Psi_{OH} + \Psi_p + FFT^{-1}(\mathbf{a})$
6. Define plasma edge: $B_p = 0$ or $\psi(R_{lim}, Z_{lim}) \rightarrow \psi_0$
7. Contour plot $\psi = \psi_0$

8. CPU time (VAX Station 2000)

Procedure unoptimized	1.5 sec
Procedure optimized	0.3 sec
Identify plasma surface	1.5 sec
Contour plot of surface	1.0 sec

9. Alcator C-Mod (VAX 3200)

   5–10 times faster

Advantages of Procedure

1. High harmonics analytically eliminated from measurement data

2. Fourier truncation can be optimized separately on each surface

3. Green's function approach eliminates the need for radial expansion functions. Un-natural functions a non-issue

4. Procedure is fast and robust

Application to Real Experiments: Alcator C-Mod

1. Show Alcator C-Mod geometry

2. Compare the procedure with "exact" numerical results

3. Run ASEQ in free boundary mode for typical profiles

4. Use ASEQ solution on the vacuum chamber as input data for the reconstruction code

5. Run the reconstruction code and see if it reproduces the ASEQ free boundary surface

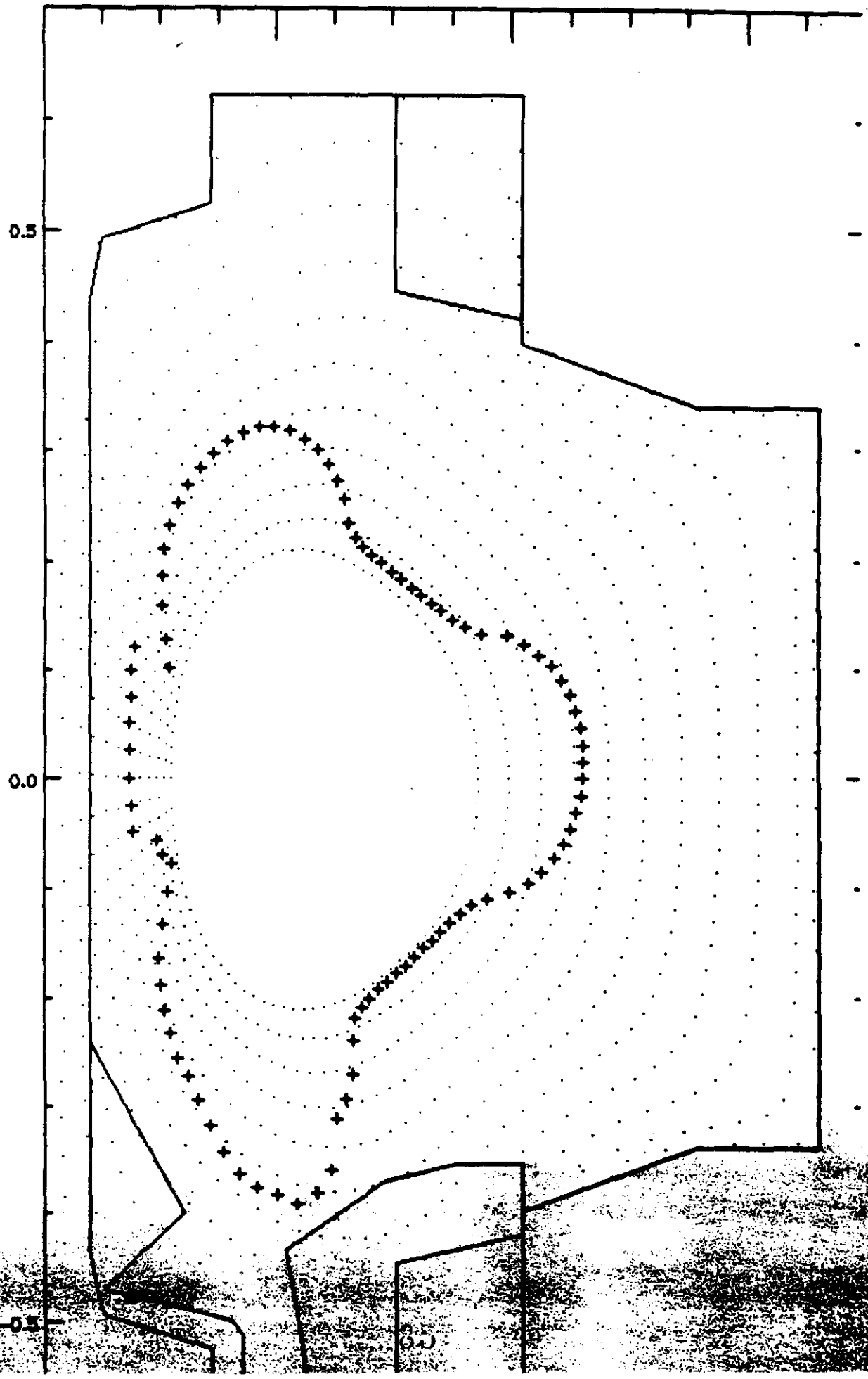
0.5
0.0
-0.5

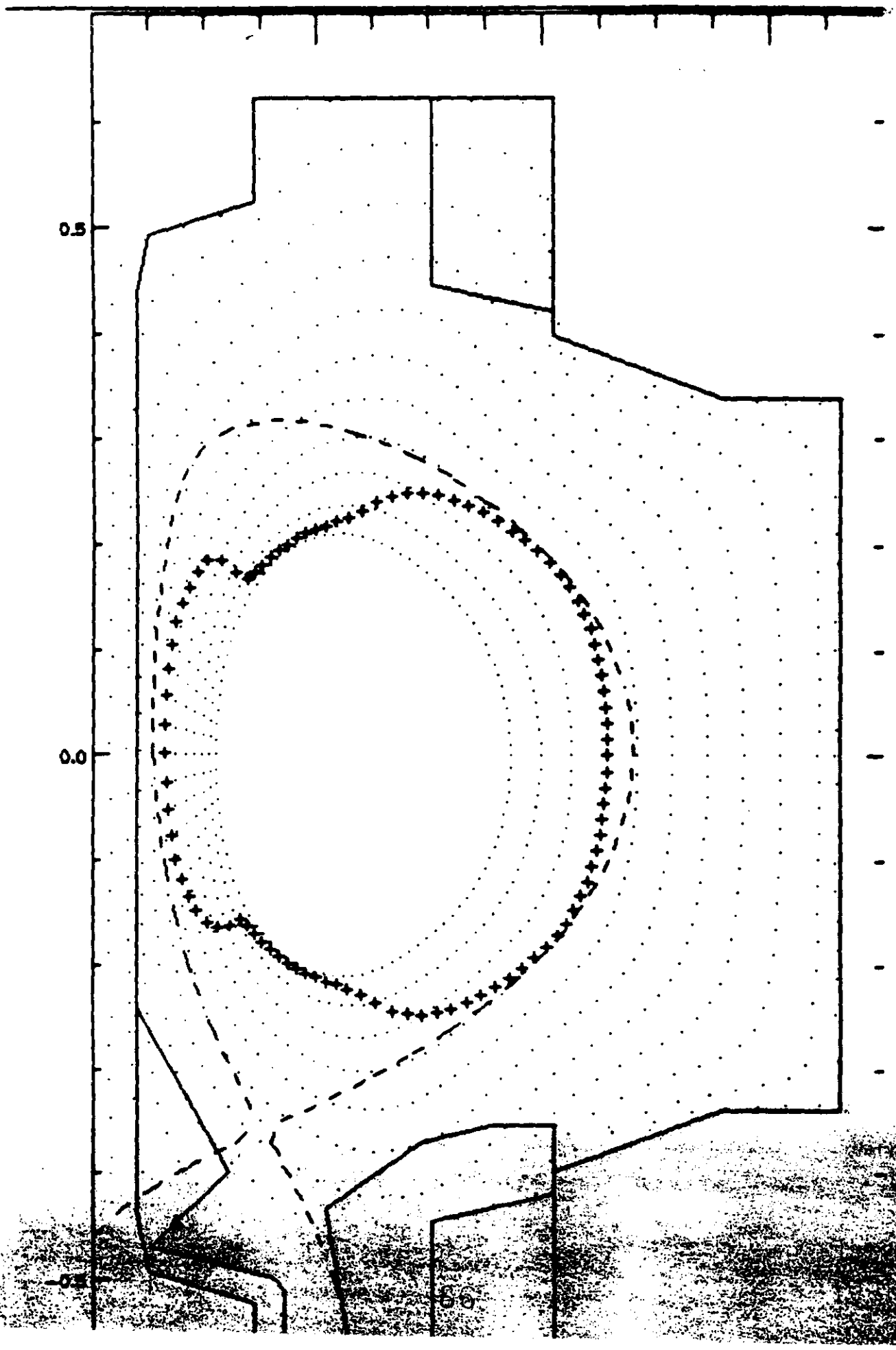
0.5
0.0
-0.5

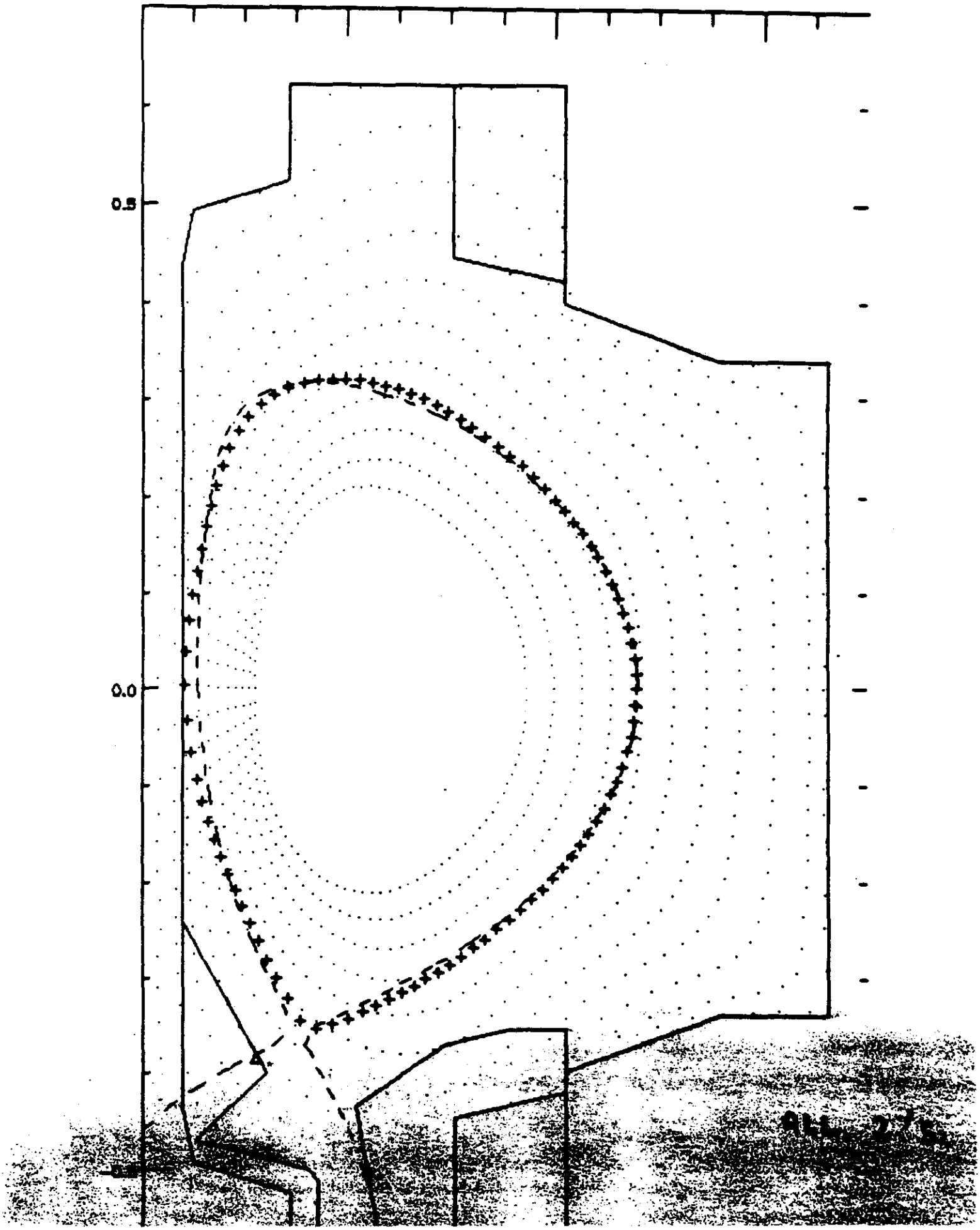
0.5
0.0

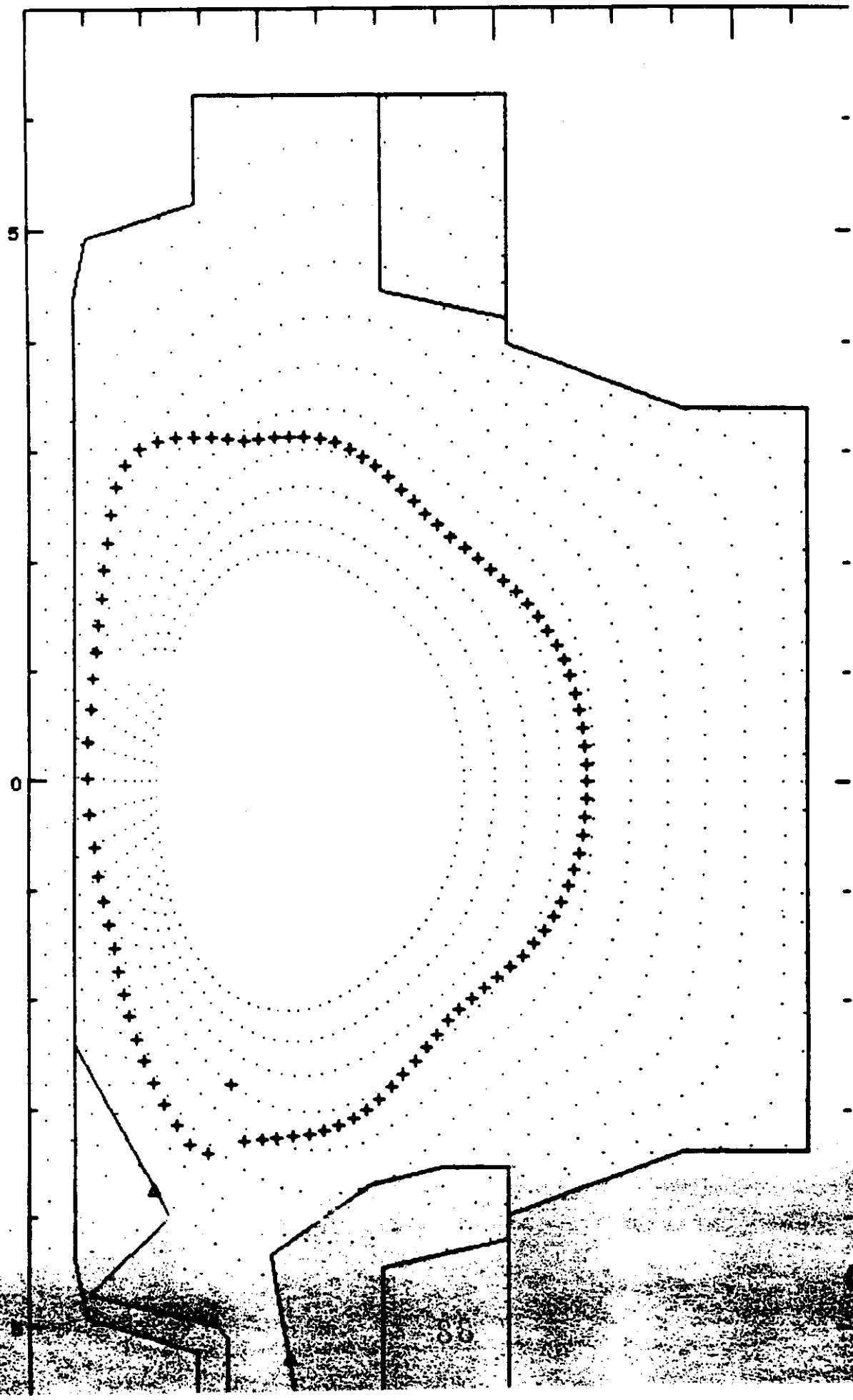
5
0

Conclusion

It appears to be a pretty good method

WORKSHOP ON FIELD MAPPING AND RECONSTRUCTION FOR THE GEM DETECTOR MAGNET

Plasma Fusion Center
MIT

August 20, 1993

R. D. Pillsbury, Jr.

- Fit to an expansion?
  - What basis functions?
  - How many terms?
  - What kind of fit?
- Solve a boundary condition driven pde?
  - Which one?
  - Sources inside the computational grid?
- Solve the inverse problem
  - Known source locations?

CHOICE OF BASIS FUNCTIONS

- Bessel functions
- Legendre polynomials
- Toroidal multipoles
- Field derivatives

CHOICE OF FITS

- Collocation
- Least squares fit
- Total least squares fit

INVERSE PROBLEM

Find the field source locations and strengths required to reproduce the data in a least squares sense.

- **Fixed sources**
  - **Virtual Casing**
    - **Number of unknown currents surrounding the computational domain.**
    - **Can lead to large oscillating currents due to the ill-conditioned matrices.**
  - **Regularization -- introduce a free parameter α and append $\alpha \sum I^2$ to the function being minimized.**
    - **How is α determined?**
  - **SVD**
    - **How is the small diagonal term cut-off determined?**

PROPOSED VIRTUAL SHELL TECHNIQUE

- Subtract computed fields from "best guess" model -- leaving perturbation fields.
- Define virtual shell surrounding region of interest.
- Solve for the currents in the shell.
- Reconstruct total field from "best guess" model and the virtual shell eddy currents.

WHAT NEXT?

- GEM model coil to be tested at Wisconsin in 1994.
- Instrument the bore in a manner similar to the one to be used on GEM.
- Use the same algorithms to map and reconstruct the field.
- N.B. -- The bore will be cold.

GEM Case 700: Rc 9.459, Zc 0.7662-14.955, FFS Rbore 0.35, ⊙9.4-.25

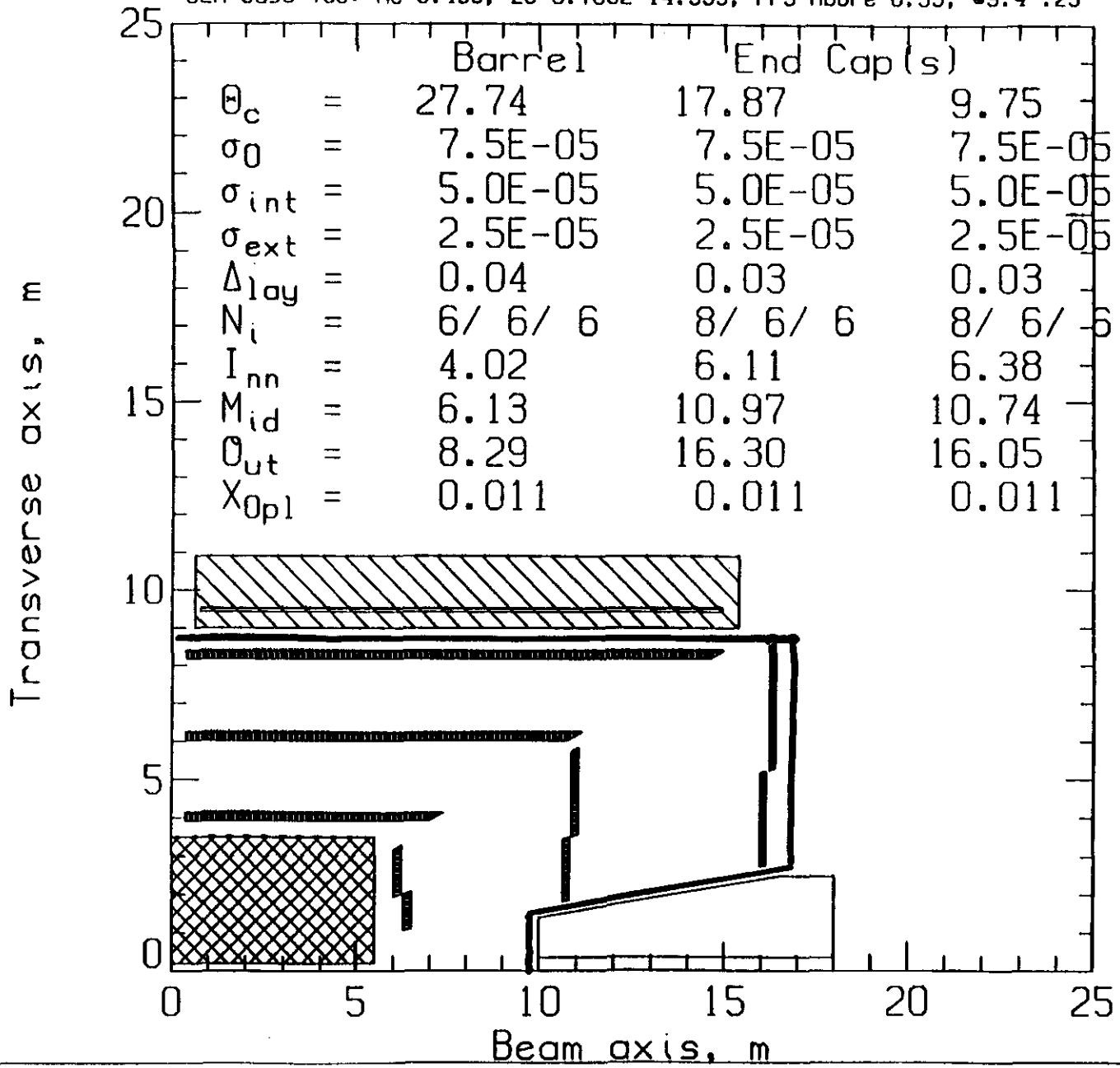

Muon: FN-03Mar93_5a Barrel: 6/6/6 Endcap: 8/6/6 h.6

IEEE Transactions on Magnetics, Vol. MAG-12, No. 6, November 1976

CHARACTERIZATION OF THREE COMMERCIALLY AVAILABLE HALL EFFECT SENSORS FOR LOW TEMPERATURES AND MAGNETIC FIELDS TO 23 T

H. H. Sample*
Physics Department, Tufts University, Medford, Massachusetts 02155

and

L. G. Rubin
Francis Bitter National Magnet Laboratory,* M.I.T., Cambridge, Massachusetts 02139

MS 107

ABSTRACT

Low temperature measurements were made on commercially supplied InAs, InSb, and GaAs Hall probes in magnetic fields as high as 23 T. For fields above ~6 T, the quantum oscillations observed for the GaAs probes were comparable in magnitude to those exhibited by the other two types, i.e., $\lesssim 2\%$. At lower fields, the sensitivities of both the GaAs and InSb sensors were different from their respective high field values; this behavior was absent in the case of the InAs probes. All three types of probes shared the advantage of reasonably good reproducibility with respect to thermal cycling and magnetic field cycling.

INTRODUCTION

In a previous publication, (RNS),[1] a justification was given for the desirability of obtaining detailed performance characteristics of commercially available Hall effect magnetic field sensors for use at high fields and low temperatures. This was followed by a description of the equipment and experimental methods employed to acquire such data on a group of InAs and InSb transverse configuration probes from two suppliers (FWB) and (ETU).[2] With the aid of the same equipment and similar techniques, the studies have been continued on a new group of devices, GaAs probes from a third supplier (CPL).[3] Measurements were made to ascertain the effects on the reproducibility of these sensors (CPL) caused by abrupt thermal cycling and magnetic field cycling, and accurate ($\pm$ 0.1%) determinations were made of the effect of temperature on the sensitivities of the CPL probes. In addition, the output linearity (including quantum oscillation effects) of all three types of sensors was measured in magnetic fields as high as 23 T.

Dimensions of the three probe types are given in Fig. 1. Details of their mounting in the sample holder are given in RNS,[1] together with a description of the probe zeroing circuit, the data acquisition system, and the data analysis procedures.

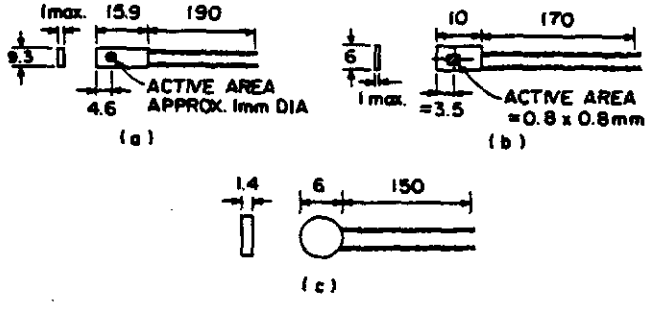

Fig. 1. Physical dimensions of Hall effect transverse probes: (a) FWB Model BHT 921, (b) ETU Model LMK, (c) CPL Model TC-8101.

RESULTS

Figure 2 shows a typical result at 4.2 K for the Hall output voltage, V, of an ETU probe plotted against magnetic field, B. On this plot, V appears to be quite linear with B, except at the highest fields, where wiggles, due to quantum oscillations, become noticeable. For clarity, only about one fourth of all the data points are plotted.

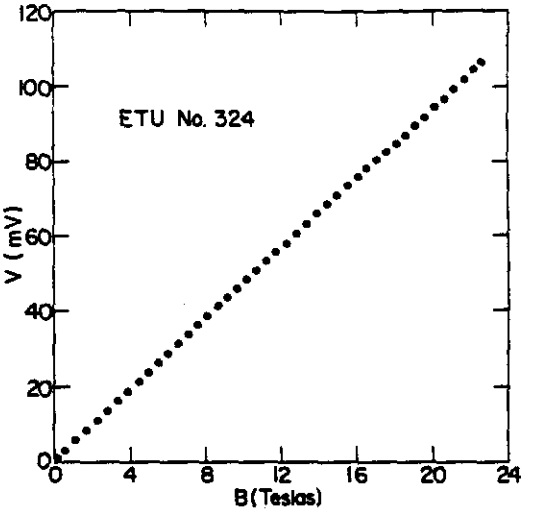

Fig. 2. Hall voltage versus magnetic field for ETU probe No. 324, at T = 4.2 K and a measuring current of 20 mA.

Deviations of the Hall voltage from a linear relationship are examined by fitting the (V, B) pairs to the equation

$$V_{calc} = A \cdot B + C \qquad (1)$$

where the slope A and intercept C are constants. The deviation voltage $\Delta V = V - V_{calc}$ is then computed and plotted against B, as shown in Fig. 3 for several probes at 4.2 K. The slope A and intercept C in Eq. (1) are chosen so as to force the deviation plot to oscillate about the zero line at the higher fields. Using this technique facilitates studying changes in slope (probe sensitivity) as a function of the number of times a probe has been thermally cycled from 300 K to 4.2 K. It also greatly facilitates the observation of the two distinct types of nonlinearity that may be present: quantum oscillations, and/or a change in slope at fields B ~ 3 - 4 T. Both types of deviations are clearly evident in, e.g., Fig. 3, ETU No. 324, but it should be noted that the low field change in slope is imperceptible in Fig. 2, a plot of the "raw" data for the same probe. We suggest that one reason why the second type of nonlinearity is so seldom reported is the difficulty in observing it in a plot such as Fig. 2. For this probe, the slope change is about 2.5%, and occurs at about 4 T. This may be seen by comparing the low field and high field deviation voltages with the solid diagonal lines in Fig. 3, which represents $\pm$1% of the total Hall voltage. Whereas the quantum oscillations decrease in magnitude at 77 K, and are not evident at all at 300 K (see RNS), the change-in-slope type of nonlinearity persists at all temperatures (although the magnitude of the slope change does depend somewhat on temperature).

Copyright © 1976 by The Institute of Electrical and Electronics Engineers, Inc.
Printed in U.S.A. Annals No. 611MA072

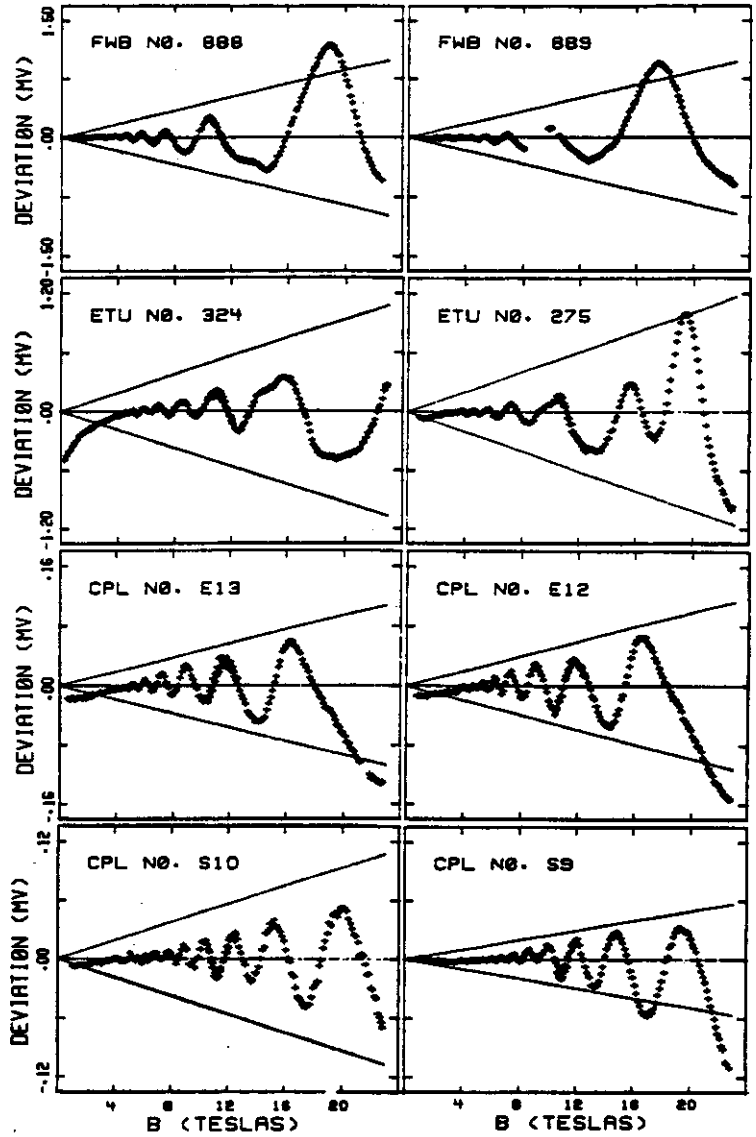

Fig. 3. Deviation, ΔV, of the Hall voltage from a linear relationship Eq. (1) for FWB, ETU, CPL(E), and CPL(S) probes at 4.2 K. The solid lines represent $\pm$ 1% of the total Hall voltage. The measuring currents used were: 60 and 50 mA for FWB Nos. 888 and 889; 20 and 18 mA for ETU Nos. 324 and 275; 20 mA for CPL Nos. E13 and E12; 40 and 35 mA for CPL Nos. S10 and S9.

We have made an approximate analysis of the change in slope at 4.2 K for the CPL probes studied here, as well as for the ETU and FWB probes in RNS. The results are: $\Delta A/A_0$ = - 0.2% to - 1% centered at B ~ 4 T for CPL probes; - 1 to - 3% centered at ~3 T for ETU probes; and < 0.2% for FWB probes. Here ΔA is the high field slope minus the low field slope. Thus, the probes become less sensitive above 3 - 4 T, as shown in Fig. 3.

Figure 3 shows the results for all the probes run to B = 23 T; two each of type FWB, ETU, CPL-E, and CPL-S. From these data and the data on FWB and ETU probes in RNS, we have analyzed the magnitudes of the quantum oscillation nonlinearities. The results are shown in Table I, where we have chosen to compare the height of the quantum oscillation peaks for a particular probe to the 15 T output voltage for that same probe. The 15 T output was chosen as a "normalizing" factor for reasons of practicality, there being few laboratories in the world with higher fields available.

Table I shows that, except for B > 15 T, the quantum oscillations for all types of probes are quite similar in magnitude. It should be emphasized that the quantum oscillation analysis was carried out independently of the change-in-slope nonlinearity for the ETU and CPL probes.

TABLE I. Quantum oscillations of Hall probes at 4.2 K

Probe type		Maximum quantum oscillation correction to linear fit (as a percent of the 15 T Hall voltage)[a] for B less than: 8 T	15 T	23 T
FWB	best	0.1	0.5	1.5
(InAs)	worst	0.2	0.8	1.9
	average	0.1_7^b	0.6^b	1.7^c
ETU	best	0.1	0.2	0.6
(InSb)	worst	0.3	0.7	2.6
	average	0.1_2^b	0.4^b	1.6^c
CPL-E	best	0.1	0.7	1.8
(GaAs)	worst	0.4	0.9	2.1
	average	0.2_4^b	0.8^b	2.0^c
CPL-S	best	0.1	0.5	1.0
(GaAs)	worst	0.1	0.8	3.0
	average	0.1^c	0.7^c	2.0^c

[a]See text for explanation.
[b]Based on the results for six probes.
[c]Based on the results for two probes.

The effect of temperature on the slope for CPL probes is shown in Table II, and is compared with the results from RNS for ETU and FWB probes. It is evident that A is somewhat more sensitive to temperature for CPL probes than for FWB and ETU probes, particularly in the 1.5 - 4.2 K range. Nevertheless, the slope changes are all less than 1%, so that for all three types, a room temperature calibration is sufficient to determine the 4.2 K value of the slope to ~1%.

TABLE II. Percent change in slope with temperature for CPL, FWB, and ETU Hall probes.

Probe Type	Slope change from 4.2 K value (%) T=1.5 K	T=4.2 K	T=77 K	T=300 K
CPL-E	-0.5	0	-0.3	+0.4
FWB	0	0	+0.4	-0.2
ETU	0	0	+0.5	+0.2

A series of thermal cycling tests was carried out on the six CPL probes. The same techniques were used as in RNS,[4] where the probes were fit to Eq. (1) and A and C were chosen to match the deviation plot to that obtained on an initial run. Except for one probe, this deviation plot matching could always be done within the experimental precision of the measurements (< 0.1% of full scale). Changes in slope as a function of thermal cycling were determined for each probe, and an average slope change for all six CPL probes was calculated as in RNS. The results are displayed in Fig. 4, along with the previous results for FWB and ETU probes.[1] From the figure, it is clear that for small numbers of thermal cycles, the CPL probes have a slope stability similar to that of the ETU probes. As they continue to be cycled, their stability is better than for the ETU's, but worse than for the FWB probes.

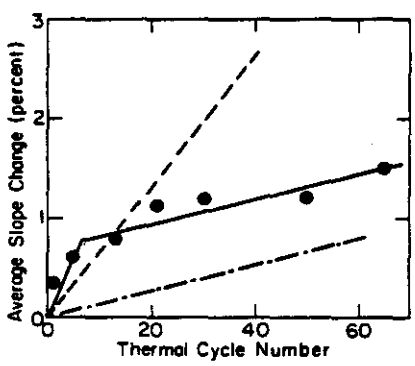

Fig. 4. Average change in slope with thermal cycling for CPL(E) probes (•, - - -), FWB probes (— - —) and ETU probes (— — —). The details of the results for FWB and ETU probes are described in RNS, as is the method of computing the average slope change.

It is useful to compare the sensitivity (defined by the constant "A" in Eq. (1)) of the sensors we studied. At a normalized current of 60 mA, the values were: FWB = 4.2 - 5.2 mV/T; ETU = 7 - 17 mV/T; CPL(E) = 1.3 - 1.5 mV/T; CPL(S) = 0.4 - 0.7 mV/T. While sensitivity alone is not the most important of the many parameters to be considered in choosing a probe, it can become critical if its value becomes too low. In an operational sense, "too low" might be defined as the point below which thermal emf's in the measuring circuit become a factor. We suggest that an output of ~10 mV, corresponding to the maximum field of the experiment, is such a lower limit; and furthermore, should be attainable at probe power dissipation levels of no more than tens of milliwatts.

For the purpose of summarizing the results, we begin with an assumption that a user has calibrated a probe in situ against a magnetometric standard and has determined the deviation plot to the required accuracy. What are the errors to be expected in subsequent measurements and how may they be guarded against?

(1) A mechanical movement or readjustment of the probe or its holder almost certainly will lead to a change in probe orientation with respect to the field. This can produce a quite large error.

(2) There will be a slope change whose magnitude is a function of thermal cycling and the type of probe. This error can range from tenths of a percent to several percent. The recommended corrective action for both (1) and (2) is a periodic in situ recalibration at two or more field points.

(3) If a direct linear readout of the sensor is desired, e.g., a DVM used with a probe adjusted for 1.000 or 10.00 mV/T sensitivity, then the only error (after recalibration) is strictly a function of the quantum oscillation effects above ~6 T and/or the change-in-slope nonlinearity below ~4 T (for some probe types). Since both of these nonlinearities appear to reproduce within ±0.1% F.S., it is simple to correct for this error by using the deviation plot. While on the subject of quantum oscillations, it is worth noting that their effect on probe linearities was the same (within a factor of two) for all types studied, including those sensors ostensibly designed to minimize such an effect.

In the "ideal" case of a sensor mounted in a fixed position in a magnet, and maintained at a constant temperature for long periods of time, there is good reason to believe that a magnetometric accuracy of < 0.2% is achievable.

It is a pleasure to acknowledge the contributions of Joseph Daigle, Donald Nelson and Frank Silva to this work. We thank Mr. K. Kasai of Copal Corp. of America for his generous assistance.

REFERENCES

* Supported by the National Science Foundation.

1. L. G. Rubin, D. R. Nelson, and H. H. Sample, "Characterization of two commercially available Hall effect sensors for high magnetic fields and low temperatures," Rev. Sci. Instrum. 46, 1624-31 (1975).
2. Model BHT 921 from the F. W. Bell Co. (FWB) 4949 Freeway Dr., Columbus, OH 43229. These InAs devices are obtainable directly from the manufacturer and also from a distributor: Lake Shore Cryotronics, Inc., 9631 Sandrock Rd., Eden, N. Y. 14057. Model LMK are InSb units and are made at the Electrotechnicky Ustav (ETU), Bratislava, Czechoslovakia. They are obtainable from Cryophysics SA, 39 Rue Rothschild, 1202 Geneva, Switzerland, and also from Canada Superconductor and Cryogenics Co., Ltd., P.O. Box 280, St. Lambert, Quebec, Canada J4P 3N8.
3. Model TC-8101 from the Copal Co., Ltd. (CPL) Tokyo, Japan are also transverse configuration probes. They are available in the USA from Copal Corp. of America, 58-25 Queens Blvd., Woodside, NJ 11377. The great majority of our measurements were performed on the standard off-the-shelf series of CPL probes, designated series "E". Subsequently, the manufacturer supplied us with several series "S" probes, presumably designed to minimize quantum oscillation effects. Where no designation is specified in the text, it should be understood as referring to series "E".
4. A magnetic field cycling procedure similar to that described in RNS for the FWB and ETU devices was also carried out on the CPL probes. However, unlike the previous studies, we considered it impractical to test for possible effects of probe current on probe stability, viz., the effects of internal $\vec{j} \times \vec{B}$ forces.

Characterization of two commercially available Hall effect sensors for high magnetic fields and low temperatures

L. G. Rubin and D. R. Nelson

Francis Bitter National Magnet Laboratory, Massachusetts Institute of Technology, Cambridge, Massachusetts 02139*

H. H. Sample*

Physics Department, Tufts University, Medford, Massachusetts 02155

(Received 30 June 1975; in final form, 15 September 1975)

A series of measurements were performed on two groups of transverse-configuration Hall effect sensors, each group consisting of devices available from a particular commercial supplier. The Hall voltage output of the probes was measured as a function of magnetic field to 18 T at temperatures of 300, 77, and 1.5–4.2 K; at the same time, the probes were subjected to a program of abrupt thermal cycling and magnetic field cycling. With the aid of computer analysis of the data the following conclusions could be drawn: (1) the outputs of one group of probes were linear with magnetic field within a worst-case value of $\sim \pm 1\%$ up to 8 T, and for the second group, to within $\pm 0.5\%$ up to 8 T and $\pm 1.4\%$ up to 18 T; (2) statement (1) was true for any of the selected temperatures; in general, variations of sensor output with temperature proved to be an unimportant factor; (3) the degree of measurement repeatability between thermal cycles varied somewhat from probe to probe within a group, but was significantly different between the two groups; (4) for a limited number of thermal cycles (~ 25), it is clear that a simple calibration procedure would suffice to maintain a field measurement accuracy of $\pm 0.2\%$ up to 14 T, at least for one group of probes.

I. INTRODUCTION

The use of Hall effect magnetic field sensors has been extended to high fields (>2.5 T) and often to liquid helium temperatures by many investigators.[1–14] Although there is much useful information in these papers, less than half of them report on *commercially available* devices; none of the latter included detailed data on performance above 5 T.

For those with the happy combination of the necessary resources, along with an inclination to use them for "rolling their own," homemade Hall probes seem to present a viable alternative. Typical of this approach was the work of Woollam *et al.*,[12] who reported the results of measurements on Bi_2Se_3 probes that were fabricated from their own single crystals. They observed a linearity of $\pm 0.8\%$ to fields of 8 T and temperatures between 1.1 and 300 K. However, it is quite likely that the average experimenter who wishes to exploit the several advantages of Hall effect sensors to solve a field measurement problem would face some obvious difficulties in trying to duplicate probes such as those described by Woollam *et al.*

The impetus for the present work was provided by (1) a recognition of the advantages offered by off-the-shelf devices as opposed to homemade probes; (2) the realization that very promising probes were available from at least two suppliers[15]; (3) a desire to settle the often conflicting claims made in the literature concerning the advantages of various semiconductor materials for use in low temperature, high field Hall probes: in particular, how FWB InAs sensors would compare with the ETU InSb devices[16]; and (4) the constant stream of requests to one of the authors (LGR) for answers to a variety of questions involving high field measurement problems, many of which turned out to be solved through the use of probes the same as, or similar to, the ones described in this paper.

Specifically, measurements were made to ascertain the effects—if any—on sensor reproducibility caused by abrupt thermal cycling, magnetic field cycling, and/or internal $\mathbf{j} \times \mathbf{B}$ forces within the probes. With the help of digital data acquisition, processing, and analysis, Hall voltage output vs magnetic field to 18 T was carefully examined at 300, 77, and 1.5–4.2 K. From such data, it was expected that accurate ($\pm 0.2\%$) determinations could be made of probe linearity, quantum oscillation effects, and the effect of temperature on probe sensitivities.

II. EXPERIMENTAL

A. Samples

The bulk of the experimental data was collected on seven each of the FWB and ETU[15] transverse probes (see Fig. 1). The decision to restrict the measurements to sensors mounted in the transverse configuration was taken for two reasons. In the first place, there would be one less variable involved in delineating probe performance. Secondly, earlier work in our laboratory with both axial and transverse probes from both suppliers indicated a higher reliability for the latter[17];

 Copyright © 1975 by the American Institute of Physics

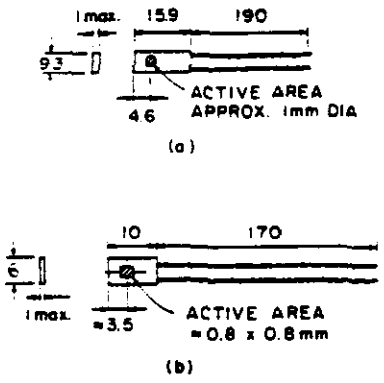

FIG. 1. Mechanical specifications of Hall effect transverse probes: (a) FWB model BHT 921; (b) ETU model LMK.

the differences seemed to be strictly of a constructional nature, since the sensors themselves appeared to be electrically identical.

B. Sample holder

A sample holder was constructed that was capable of mounting four probes simultaneously, but isolated from one another (see Fig. 2). The sensors were carefully protected from normal handling hazards such as mechanical shocks and bumps. The use of cements or epoxies to hold them in place was avoided in order to prevent sensor stresses upon cooldown. The holder was designed to fit comfortably within the 4.2 cm diam inner tail of a standard double-walled metal cryostat. The latter provided a constant temperature environment at 300, 77, and the 1.5–4.2 K range, the temperatures being chosen for their convenience in obtaining values of the temperature coefficient of the Hall voltage output.

The vertical axis of the sample holder coincided with the magnetic field axis of a water-cooled Bitter magnet. Most of the measurements were taken in a 15 T-5 cm bore magnet; several runs were also made in the Magnet Lab's 18 T-5 cm bore solenoid. In the near future, there are plans to extend the range of the measurements to 23 T, using the 3 cm bore 10 MW magnet routinely available for this purpose.

Careful machining was responsible for minimizing alignment errors in the pitch (critical) and yaw (not critical) angles of the probe with respect to the field (see Fig. 2). Reasonable care was then exercised to adjust the roll angle to as close to zero as possible; once inserted, the probe was kept by its close fit in the holder from moving as the runs progressed. This procedure meant that an error in the *absolute* calibration could—and almost certainly did—exist, due to the lack of perfect perpendicularity between field and probe. However, as long as the probe was not removed from the sample holder, the results could be compared from run to run within the limits of precision set by the remainder of the apparatus. As will be discussed shortly, this was about ±0.1%, compared to the several percent error that could be expected if, for example, a sensor were removed from the holder, carefully reinserted, and the before-and-after results compared.

C. Measurement apparatus

The four leads from each of the four sensors were brought up along the sample holder and out of the cryostat in sets of twisted shielded pairs. The leads from the sensor being measured terminated in a box which included the zero offset correction circuit[18] (see Fig. 3 for details and an explanation), and switches and terminal points for connection to the current supply and voltmeter.

A Keithley model 225 was used as a constant current source. Although absolute accuracy of current was never a factor in the experiment, it was important that the originally selected value of current be repeated from one run to the next; for this purpose, a precision resistor of suitable value was placed in series with the sensor to monitor the current. To measure the voltage across the monitor resistor and the Hall voltage V from the sensor, a Keithley model 140 amplifier was used. Its 10 V full scale output was fed into a 4½ digit digital panel meter (DPM). This combination easily achieved a precision of 0.02% of full scale; currents through the sensors were selected so that at least 50% of full scale output was achieved at the maximum magnetic field (either 15 or 18 T, depending on the magnet).

A second DPM was employed to measure a voltage proportional to the instantaneous current through the magnet. The digital outputs of the two DPMs were read out on command into a Teletype through a serializer-code converter module. A minimum of 40 paired data points were taken for each run, the pairs consisting of a five digit word for magnet current and one for sensor Hall voltage.

At the beginning of a set of runs, and sometimes at the end, a magnet calibration was performed. For this purpose, a magnetometer was placed in the magnet and its output recorded as a function of magnet current on the DPM channel otherwise used for the Hall probes. The magnetometer, an analog coil-integrator system, was sufficiently linear and stable so that it was almost an order of magnitude more precise than the overall limit of error of the entire system.

The individual sensors, after being zeroed, were always vertically adjusted for a maximum signal at some convenient field. This ensured their placement at a repeatable location in the magnet, i.e., at its magnetic center (see Fig. 2).

D. Data analysis

The data were analyzed by feeding the paper tapes for the various runs into a PDP-11 computer which was equipped with an oscilloscope display screen for plotting the results of fits to the data. The final fit to a given run could be photographed with a Polaroid camera attachment. Appropriate software was developed to analyze the data as described below.

Before a Hall probe measurement could be analyzed, the magnet calibration appropriate to that day had to be determined. For this purpose, the magnet calibration tape (consisting of magnet current, I_M, and magnetometer reading, B, pairs) was stored in the computer in tabular form.

A Hall probe tape (consisting of I_M and Hall voltage, V, pairs) was then read into the computer and analyzed in the following manner:

(1) I_M values were converted to B values by interpolation of the magnet calibration table.

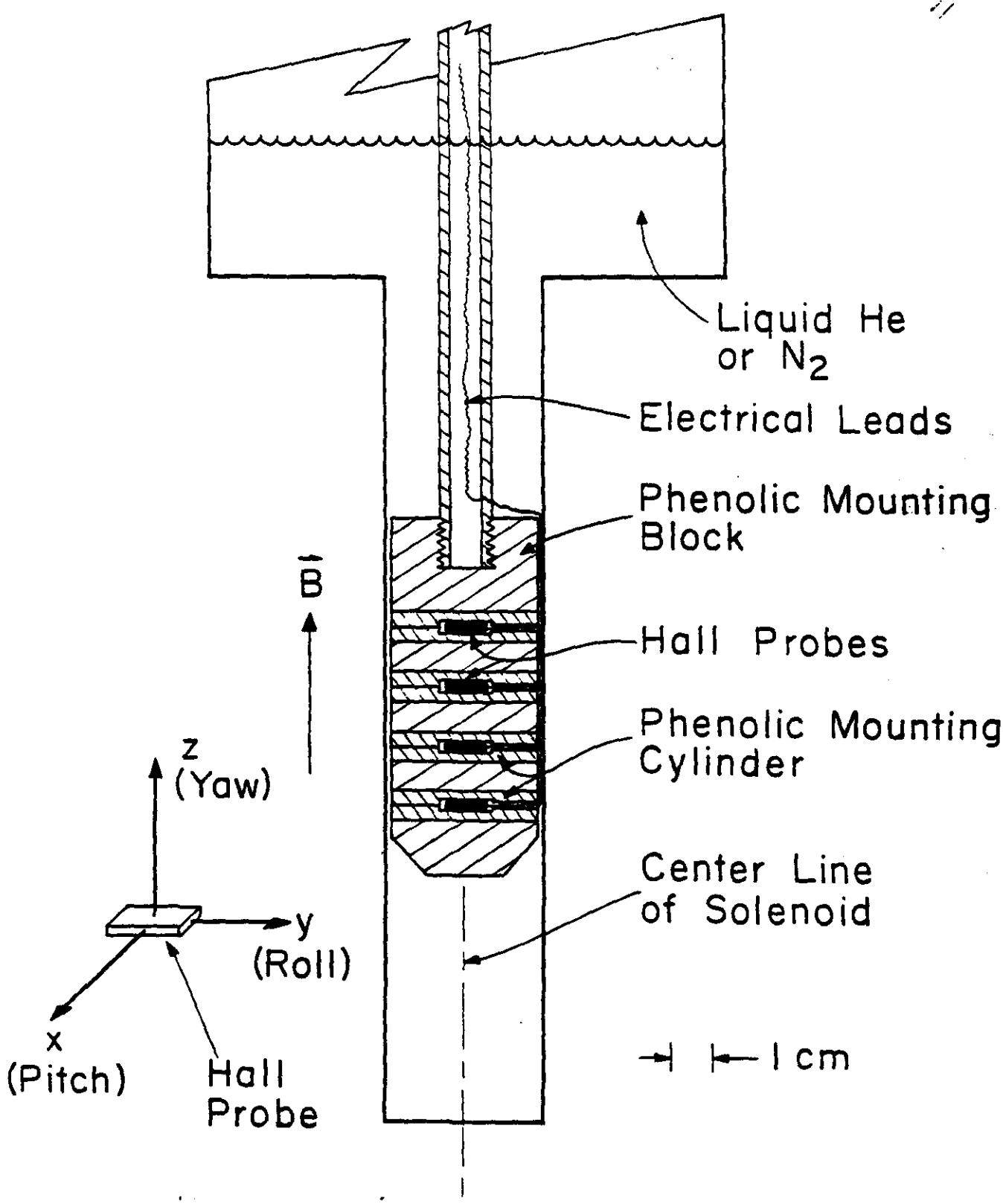

FIG. 2. Lower portion of the sample holder shown inserted in the tail of the liquid He Dewar. The sample holder can be adjusted in the z direction to position each probe in the maximum field. The pitch, roll, and yaw angles (discussed in the text) are defined as rotations about the x, y, and z axes, respectively.

(2) Hall voltage data were fitted to the simple equation

$$V_{calc} = A \cdot B + C, \quad (1)$$

where the slope A and intercept C are constants.

(3) A calculation was made of the deviation plot,

$$\Delta V = V - V_{calc},$$

[where V_{calc} is defined by Eq. (1)] vs B.

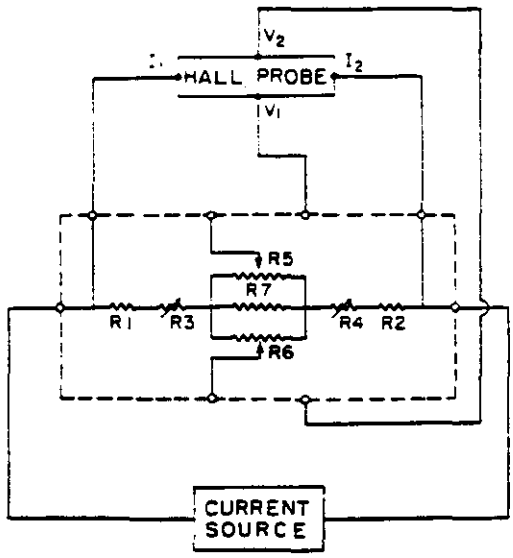

FIG. 3. Zeroing circuit. Typical values: R_1, R_2—1 kΩ; R_3, R_4—1 kΩ adjustable; R_5, R_6—100 Ω adjustable; R_7—2 Ω. The voltmeter is first connected between V_1 and the arm of R_5, and with the current on. R_5, R_6, and R_5 are adjusted to zero the voltmeter. V_1 may then be tied to the arm of R_5 at what represents an equipotential point (no current flows between them). The voltmeter is then connected to its normal measuring position between V_2 and the arm of R_6. Once the latter is adjusted for zero (at zero field, of course), the sensor–voltmeter system is capable of measurement over the full field range without the problem of a magnetoresistive zero shift. It should be noted that the shunting effect of the zeroing circuit on the ~1 Ω probe is <0.05%.

(4) The constants A and C were arbitrarily adjusted in an attempt to match previous deviation plots for the probe, after which the new deviation plot was recalculated.

It was necessary to include a nonzero intercept C in the analysis for two reasons. First, as described below, it was observed that the ETU probes exhibited a behavior corresponding to a change in slope A at higher fields. Since we were primarily interested in the high-field behavior, a best fit to these high field data according to Eq. (1) requires a large nonzero value of C. Second, we found that during the course of many of the runs an unpredictable zero shift in the magnet current was apt to occur; this often amounted to 0.02 T and occasionally reached 0.05 T. Such a zero shift between the respective times the magnet calibration and Hall probe measurement were performed would cause a spurious offset (nonzero intercept) in the deviation plot, unless a nonzero value of C was chosen in Eq. (1). These relatively small spurious C values (appropriate to the FWB probes) were ignored when comparing deviation plots from one run to the next on a given probe.

E. Reproducibility test procedures

The 12 probes which were tested for reproducibility (six FWB and six ETU) were run in batches of four. The first batch contained four virgin (i.e., not previously thermally cycled by us)[19] FWB probes. Two of these probes were run with measuring currents of 80 mA and two with 8 mA, to check for measuring current effects. The second batch consisted of two FWB probes (one of which had been previously thermally cycled six times and one virgin probe) and a similar pair of ETU probes. For this second batch, the measuring currents were 80 mA for the FWB probes and 20 mA for the ETU probes. The third batch contained four virgin ETU probes, two of which were run at 30 mA and two at 3 mA. Each batch of probes remained in the sample holder untouched until the series of runs on that batch was complete.

Two methods of taking data were employed:

(1) the step method, whereby the magnet current I_m was manually adjusted to the desired value and at least two (I_M, V) pairs read onto the tape after waiting a short time for equilibrium (~5 sec), and

(2) the sweep method, in which (I_M, V) pairs were automatically read every 2 sec while sweeping the field from zero to the maximum B and back to zero at a rate of about 4 T/min.

The step method yielded very precise data as indicated in Fig. 4, which shows plots of the deviation of the Hall voltage from a linear relationship. In these figures, the solid lines represent ±1% deviations; it can be seen that for these examples (and generally, for all sensors) the precision of the step method data is better than ±0.1% of the maximum Hall voltage.[20] The sweep method was somewhat less precise (~±0.1–±0.2% of the maximum Hall voltage), but yielded a much larger number of data points. This method also had the advantage of being faster and more convenient.

The probes were tested in the following manner. First, an initial run was made at 4.2 K on each of the probes, usually in the 18 T solenoid, using the step method of taking data. This allowed a precise value of the slope and deviation plot to be obtained for comparison with later runs.

The remainder of the runs was usually made using the less precise swept field method to 15 T.[21] Each of these runs consisted of a measurement on each of the four probes, followed by approximately 20 field cycles to 15 T at a rate of ~10 T/min (with the probes still at 4.2 K and carrying their normal currents). The procedure was concluded by a remeasurement of each probe.

Between each run on a given batch of probes, the sample holder was thermally cycled from room temperature to 4.2 K, usually seven or eight times. The thermal cycling procedure consisted of cooling to 4.2 K in about 5 min and warming to room temperature in about 15–20 min. It should be emphasized that during the thermal cycling procedure, the probes remained in fixed positions in the sample holder, and care was taken to eliminate all moisture from the sample holder before cooling again. These precautions were important to ensure that observed changes in the probe calibrations were not due to orientation effects or strains produced by ice formation.

To compare the results for a given probe to the initial results (those from the initial run to 18 T), each set of data was analyzed by choosing the slope so that the corresponding deviation plot best matched the initial deviation plot at the higher fields (greater than ~5 T). The uncertainty in the slopes so obtained was about ±0.1%. Except for one ETU probe, the deviation plot matching procedure was valid to within that error, even when the slope had changed by a few percent. This is illustrated in Fig. 5 for an ETU probe. Here, the data points are the results of the initial run, and

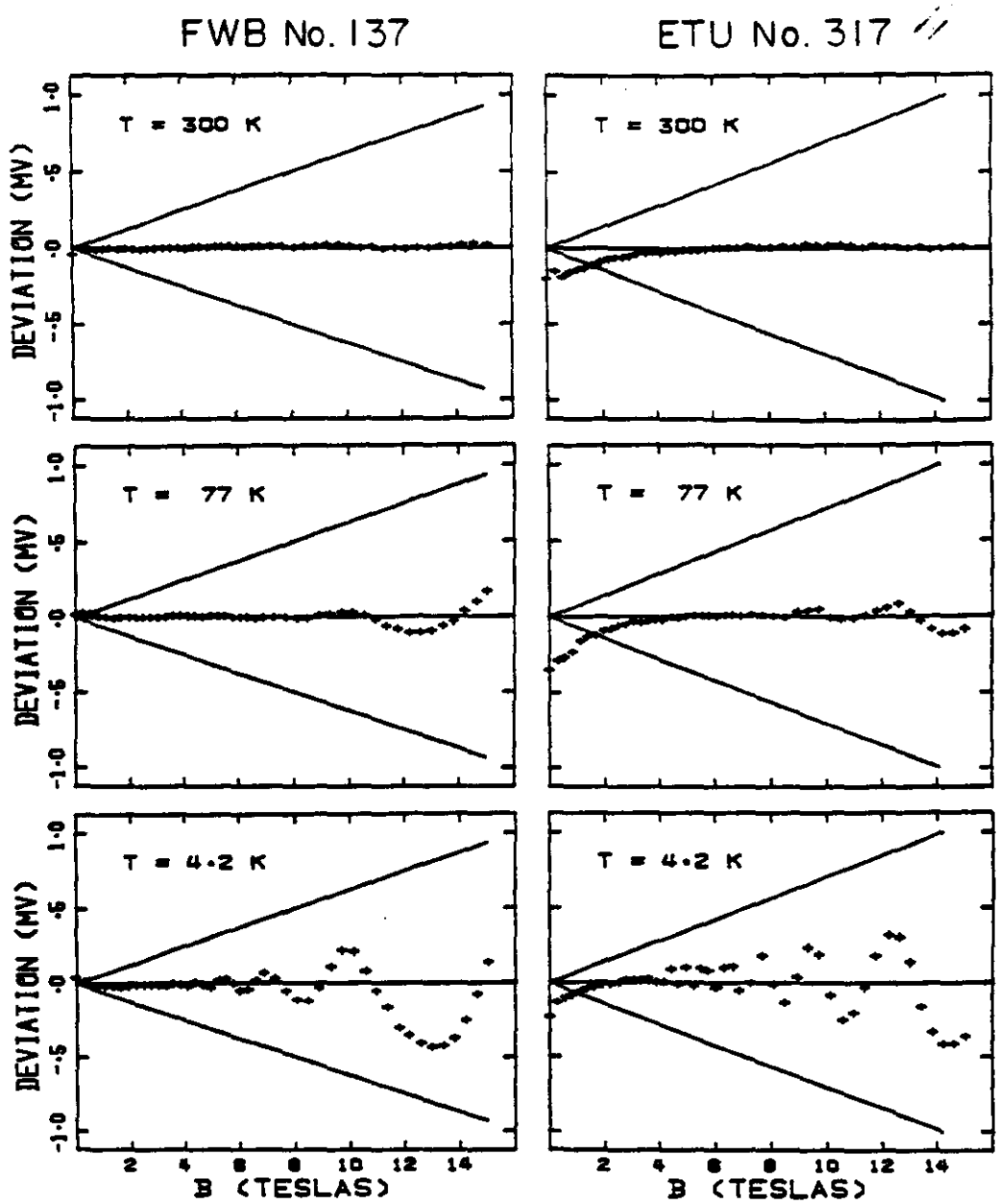

FIG. 4. Deviation of the Hall voltage from the linear relationship defined by Eq. (1) for an FWB and an ETU probe at 300, 77, and 4.2 K. The solid lines represent ±1% of the total Hall voltage. For the FWB probe, the slopes used in calculating the deviation plots were 6.215, 6.250, and 6.225 mV/T at 300, 77, and 4.2 K, respectively, using a measuring current of 80 mA. For the ETU probe, the slopes were 7.070, 7.088, and 7.055 mV/T at 300, 77, and 4.2 K, respectively, at 60 mA.

the solid line is the computer-smoothed behavior of a later swept field run where the slope had changed by about 2%.

III. RESULTS AND DISCUSSION

A. Effects of temperature

The two types of probes were examined for effects of temperature on the probe calibration. Part of this test consisted of mounting a virgin FWB and a virgin ETU probe in the sample holder and making step method runs to 15 T on each at 300, 77, and 4.2 K without warming the sample holder between runs. These results are displayed in Fig. 4, where the development of the quantum oscillations in the Hall voltage with decreasing temperature is clearly evident. A nonzero intercept is evident in Fig. 4 for the ETU probe at all temperatures. This type of behavior was characteristic of all ETU probes and is discussed below.

The second part of the test consisted of examining another ETU probe and another FWB probe at 4.2 and 1.5 K during

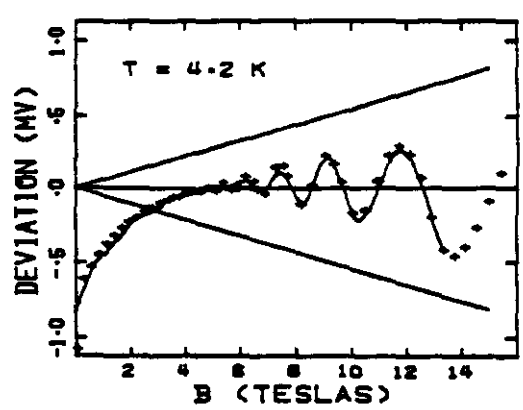

FIG. 5. Deviation of the Hall voltage from the linear relationship defined by Eq. (1) for ETU probe No. 324. The points are from the initial run, where the slope was 5.430 mV/T at 30 mA, and have been truncated at ~16 T to simplify the comparison. The drawn curve is the computer-smoothed result of a subsequent run using the swept field method, where the slope was 5.320 mV/T at 30 mA, or a change of about 2%. The straight lines represent ±1% of the total Hall voltage.

TABLE I. Percent change in slope with temperature for FWB and ETU probes.

Probe type	Slope change from 4.2 K value (%) $T=1.5$ K	$T=4.2$ K	$T=77$ K	$T=300$ K
FWB	0	0	−0.4	−0.2
ETU	0	0	−0.5	−0.2

the same run using the step method to 15 T. These results are not shown; however, for both probes, the 4.2 and 1.5 K slopes and deviation plots were identical to within the experimental precision.

The temperature effect results are summarized in Table I. Both types of probes behave in a similar manner: between 1.5 and 4.2 K, there is no change in slope; between 4.2 and 77 K the slope (e.g., probe sensitivity) increases; and between 77 K and room temperature, the slope decreases again. It should also be noted that for both types of probes, the room temperature value of the slope is within 0.2% of the 4.2 K value.

B. Deviations from linearity

All probes tested showed deviations from a linear Hall voltage vs magnetic field relationship at 4.2 K, as illustrated in Figs. 4 and 5. These deviations could be classified into two distinct categories: (1) quantum oscillations and (2) a change in slope at higher magnetic fields.

The results for all the initial runs at 4.2 K using the step method were fit to a linear relationship whose slope was chosen so that the resulting deviation plot oscillated about the deviation plot zero line at higher magnetic fields (see Figs. 4 and 5 for example). This choice of slope was arbitrary to some extent due to the asymmetric and/or irregular nature of the oscillations for most of the probes. The maximum magnitudes of the oscillations for fields B less than 8, 14, and 18 T were then determined for each probe, as a percentage of the Hall voltage output. This was easily accomplished with the deviation plots by measuring the height of an oscillation compared to the height of the 1% line at that field. This analysis was carried out only for B greater than ~5 T, the field for which quantum oscillations became clearly evident.

TABLE II. Quantum oscillations of Hall probes at 4.2 K.

Probe	Maximum percent quantum oscillation correction to linear fit,[a] for B less than: 8 T	14 T	18 T
FWB least (No. 888)	0.3	0.5	0.9
FWB greatest (No. 43)	0.5	0.8	1.4
FWB average (seven probes)	0.3	0.6	1.2[b]
ETU least (No. 323)	0.2	0.2	0.3
ETU greatest (No. 247)	0.6	1.5	1.5
ETU average (seven probes)	0.3	0.5	0.6[b]

[a] See text for explanation.
[b] The deviation plots for some of the probes were extrapolated from lower fields in calculating this average.

Table II summarizes the results of the above analysis, listing the FWB and ETU probes having the largest and smallest oscillations, and the average values for the seven probes of each type studied. It is clear that while the ETU probes have somewhat smaller quantum oscillations than the FWB probes at the highest fields (>14 T), the oscillations are quite similar in magnitude at lower fields for the two types of probes.

The second type of deviation from nonlinearity, the change in slope at higher magnetic field, occurred only for the ETU probes. This behavior is best illustrated in Fig. 5, where the deviation plot shows a large nonzero intercept on the $B=0$ axis and a kink (equivalent to a slope change) centered at about 3 T. It should be noted that *all* the ETU probes had large nonzero intercepts on the $B=0$ axis (much greater than those allowed by possible zero shifts in the magnet current) when the high field data were forced to oscillate about the deviation plot zero line by appropriate choices of the fit constants A and C in Eq. (1). The ETU probe deviation plots could, of course, have been forced to go through the origin by choosing a smaller magnitude of the constant C (consistent with possible shifts in the magnet current), but this would have made the deviation plots at the higher fields oscillate about a line running diagonally downwards; this again amounts to a change in slope A, of the unit at higher fields. For many ETU probes, this change in slope might not be apparent unless data were taken at fields greater than 6–8 T. That is, the data below these fields could be fitted using a different value for the slope (one close to the low field value), such that the resulting deviation plot would still remain within ±1% of the linear relationship. The magnitude of the slope changes were determined for each of the ETU probes by comparing the low field behavior to the 1% error line in the deviation plot. The field at which the slope change occurs was determined by extrapolating the low field slope to the point of intersection with the zero line of the deviation plot. Since neither of these procedures is very precise, the results listed in Table III should be taken only as a rough measure of the ETU probe behavior.

We emphasize that this second type of nonlinearity was not evident in any of the FWB probes. Moreover, as seen in Fig. 4, this nonlinearity is evident in the ETU probe at 77 and 300 K, as well as at 4.2 K. The magnitude of the slope change does change, however, in going from room temperature to 4.2 K.

TABLE III. Difference in slope at low and high fields for ETU probes at 4.2 K.

Probe	Slope difference[a] (%)	Field at which slope change occurs[b] (tesla)
ETU least (No. 275)	−1	2.0
ETU greatest (No. 324)	−3	4.0
ETU average (seven probes)	−2.8	2.6

[a] High field slope minus low field slope, accuracy ±0.5%. See text for explanation.
[b] Accuracy ±0.5 T. See text for explanation.

112

C. Reproducibility tests

The results of the reproducibility tests (described in Sec. II E) on the six FWB and six ETU probes are summarized in Fig. 6. In this figure, (a) and (b) are the FWB and ETU probes which exhibited the smallest slope changes with thermal cycling, whereas (c) and (d) represent more typical slope changes for each type of probe. As illustrated in Fig. 6, different values of the slope were often observed before and after magnetic field cycling during the same run (i.e., at a single thermal cycle number). This "spread" in the slope almost always developed *after* the magnitude of the slope had been observed to change on a previous thermal cycle. We thus feel that the shaded bands in Fig. 6 are a measure of the uncertainty in the value of the slope which will be obtained after a given number of thermal cycles. The bands include the ~0.1% slope measurement uncertainty.

As illustrated in Fig. 6, the slopes of the FWB probes are more stable than those of the ETU probes with regard to thermal cycling. In fact, only two of the FWB probes had changed their slopes after eight thermal cycles, whereas all the ETU probes had changed slope by nine thermal cycles.

The average slope stabilities for the six FWB and six ETU probes are indicated in Fig. 6 (e) and (f), respectively. Since all the probes of a given type were not studied at the same thermal cycle numbers, this average was taken to be the maximum magnitude of the slope change observed during all previous thermal cycles. Again, the FWB probes are much more stable than the ETU probes, which can be seen by comparing (e) and (f) at 25 thermal cycles: the ETU probe average amounts to a slope change of 1.5%, whereas the average for the FWB probes is 0.4%. In addition, none of the FWB probes changed slope by more than 1%, even after 60 thermal cycles, while three of the ETU probes changed by 2% or more after just 25 cycles.

For the FWB probes, there was no correlation between probe current and slope stability. In the case of the ETU probes, however, the two probes that carried low currents (3 mA) underwent slope changes of 0.5% or less after 25 thermal cycles. The four probes which carried high currents (20–30 mA) had slope changes of 0.9, 2.0, 2.6, and 2.6% after 25 cycles. Thus there may be a significant correlation between high measuring current and poor slope stability for the ETU probes, quite possibly due to $\mathbf{j}\times\mathbf{B}$ forces.

In preliminary measurements on both FWB and ETU probes, we noted a significant failure rate for probes under thermal cycling. The probe failures (characterized by open circuiting of the leads or very large changes in sensitivity or zero offset) appeared to be correlated with frequent mounting and demounting in the sample holder between runs. Unfortunately, no precise records of the handling of probes between runs were kept at that time.

In the present series of measurements on 14 probes, we observed *no* failures after the initial thermal cycling for the first measurement, even though significant zero offset changes sometimes occurred. The zero adjustment circuit described in Fig. 3 was very useful in compensating for these changes. It is safe to say that its incorporation into a measuring circuit will extend the useful life of almost all probes.

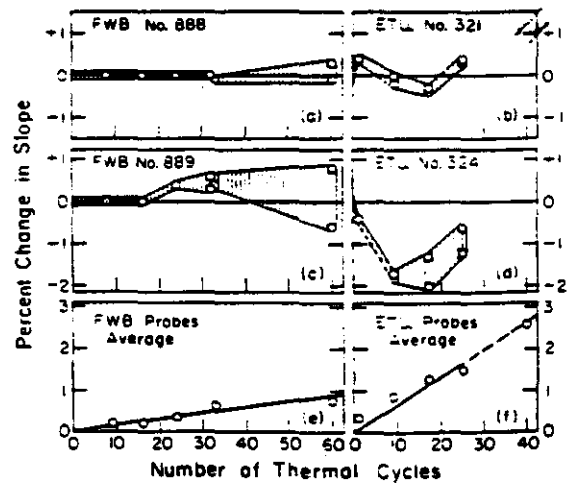

FIG. 6. Change in slope with thermal cycling for FWB and ETU probes. (a) and (b) show the results for the FWB and ETU probes with the smallest observed slope change, whereas (c) and (d) represent more typical behavior of each type. More than one datum point at a given number of thermal cycles indicates that different values of slope were observed before and after field cycling on that run. The shaded areas represent the uncertainty in the slope, including the ~0.1% measurement uncertainty. (e) and (f) give the average slope changes for the six FWB and six ETU probes studied, as explained in the text. The point at 40 thermal cycles in (f) is based on the results for only two probes.

We did observe one FWB and one ETU probe failure on the first cooldown (immediately following mounting in the sample holder). Thus, it may be that probe failures are induced *entirely* by mechanical strains during mounting, since it is well known that the probes are very delicate.

The question of reliability and "long life" is undoubtedly an important one, but it is not unusual for there to be tradeoffs and compromises made when the pros and cons of transducer performance are considered. Granting that in the worst case of repeated and abrupt cooldowns, one might find probe failures after 50 or even 25 cycles, that still represents a cost of only $3–$8 per run, based on the present price of $150–$200 per sensor. Since liquid helium is almost always consumed in these same runs, one should consider the *relative* costs involved.[22]

In summary, the FWB probes are calibratible and repeatable under thermal cycling to better than ±1%. Moreover, if only a 1% field measurement is desired, then a simple two-point calibration can be performed at *room temperature* and the quantum oscillations can be ignored up to 14 T. It is possible that if the probes are not thermally cycled, the calibration stability is much better than 1%. Indeed, we were unable to detect any changes in calibration for both an FWB and ETU probe which were magnetic field cycled about 20 times on four different days, where the sample holder was maintained at 77 K or below. But in any event, an FWB probe which has been thermally cycled $\lesssim$25 times can apparently be calibrated to about ±0.2% by determining the slope from a two-point calibration at 4.2 K and using a previously determined deviation plot.

The ETU probes have the disadvantage of exhibiting a slope change at higher fields which *requires* a deviation plot to be used for even a 1% calibration to 14 T. For fields less than ~8 T, however, these sensors can probably be fitted to a linear relationship at room temperature, and the same

calibration used at 4.2 K to better than 1% accuracy. But one must be aware of the somewhat poorer slope stability of the ETU probes on thermal cycling.

Both types of probes possess the convenient features of no detectable change in output over the 1.5–4.2 K temperature range and sufficiently high sensitivity (~10 mV/T at currents ranging from 20 to 90 mA), so that direct readout with a digital panel meter is straightforward and inexpensive. By comparison the probes described by Woollam *et al.*[12] had a sensitivity of ~0.3 mV/T at 300 mA.

The sensors described in this paper have a number of very attractive advantages when compared to other magnetometers: (1) small size; (2) low power dissipation (from either sensor heating or, with proper lead configuration, cryostatic heat leaks); (3) high sensitivity; (4) low source impedance; (5) reasonably good reproducibility and linearity, which are directly responsible for the ease with which these devices may be calibrated and subsequently checked; (6) inexpensive readout instrumentation, which is a direct result of (3), (4) and (5).

ACKNOWLEDGMENTS

We are indebted to Joseph Daigle and Frank Silva for their contributions to this work. We sincerely thank Kenneth Geiger of Cryophysics, SA and Jeff Dierker of F. W. Bell, Inc. for their help in providing some probes on loan and also expediting shipment on the remainder.

*Supported by the National Science Foundation.

[1]M. S. Lubell and B. S. Chandrasekhar, Rev. Sci. Instrum. 35, 906 (1964).
[2]D. A. Hill and C. Hwang, J. Sci. Instrum. 43, 581 (1966).
[3]I. Hlásnik, F. Chovanec, and M. Polák, Cryogenics 6, 89 (1966).
[4]K. G. Günther and H. Freller, Cryogenics 7, 49 (1967).
[5]J. E. Simpkins, Rev. Sci. Instrum. 39, 570 (1968).
[6]B. G. Lazarev, L. S. Lazereva, S. I. Goridov, and S. G. Shul'man, Sov. Phys. Dokl. 13, 696 (1969).
[7]V. G. Veselago, M. V. Glushkov, V. M. Ivanov, and S. G. Shul'man, Instrum. Exp. Tech. 1970, 1580.
[8]M. Polák and I. Hlásnik, Solid-State Electron. 13, 219 (1970).
[9]G. W. Donaldson, Adv. Cryog. Eng. 18, 416 (1973).
[10]A. A. Kolmakov, R. V. Parien'ev, V. I. Pogodin, and G. A. Yur'eva, Instrum. Exp. Tech. 1971, 289.
[11]G. K. Yagola, Y. I. Kazantsev, and E. N. Lysenko, Meas. Tech. 1973, 1535.
[12]J. A. Woollam, H. A. Beale, and I. L. Spain, Rev. Sci. Instrum. 44, 432 (1973).
[13]P. Kordoš, L. Janšak, and V. Benč, Cryogenics 13, 313 (1973).
[14]M. Polák, Rev. Sci. Instrum. 44, 1794 (1973).
[15]Model BHT 921 from the F. W. Bell Co. (FWB), 4949 Freeway Dr., Columbus, OH 43229. These are obtainable directly from the manufacturer and also from a distributor: Lake Shore Cryotronics, Inc., 9631 Sandrock Rd., Eden, NY 14057. Model LMK made at the Electrotechnicky Ustav (ETU), Bratislava, Czechoslovakia are obtainable from Cryophysics SA, 39 Rue Rothschild, 1202 Geneva, Switzerland, and also from Canada Superconductor and Cryogenics Co., Ltd., P. O. Box 280, St. Lambert, Quebec, Canada J4P 3N8.
[16]GaAs has also been suggested for this purpose, but to our knowledge, the only published report on its high field performance is that of Kordoš *et al.* (Ref. 13). It has only very recently come to our attention that GaAs probes are now commercially available from Copal Co. (Japan). Preliminary measurements on one such probe indicated a behavior similar to that of the ETU probe but with less than one-tenth the latter's sensitivity. We expect to report the results of more complete measurements on these probes in a separate publication.
[17]This impression was strengthened in the case of the FWB transverse units by favorable reports from other users who have calibrated their probes at our laboratory.
[18]F. Kuhrt, Siemens Z. 28, 370 (1956).
[19]Both suppliers subject their probes to some thermal cycling before shipping.
[20]Since the solid lines in Fig. 4 represent ±1% of the total Hall voltage, then ±0.1% of the *maximum* Hall voltage is simply one-tenth the vertical distance between the two solid lines at the highest field. The scatter of the data points from a smooth curve may be seen to be less than this amount. Such results were representative of all the step method data.
[21]The choice between the 15 T (5 MW) and 18 T (7.5 MW) solenoids for these runs was based mostly on availability of the respective magnets. It seemed logical for us to concentrate on the technologically important region below 15 T, particularly since future plans do include extension of the work to higher fields.
[22]This would appear to be an appropriate place for the standard disclaimer that the results or opinions presented in this paper in any way constitute an endorsement of any manufacturer or product. It is suggested that a careful evaluation be made by prospective users of all the factors involved before possibly refusing consideration of the probes under discussion *solely* because of their finite life under some sets of conditions.

My Effort is 3 Pronged

- Generate the field with enough precision using Tosca
- Determine the number of coefficients necessary to adequately represent the field
- Determine the minimum number and placement of magnetic probes to adequately determine the field

B_φ should be zero in the symmetry plane

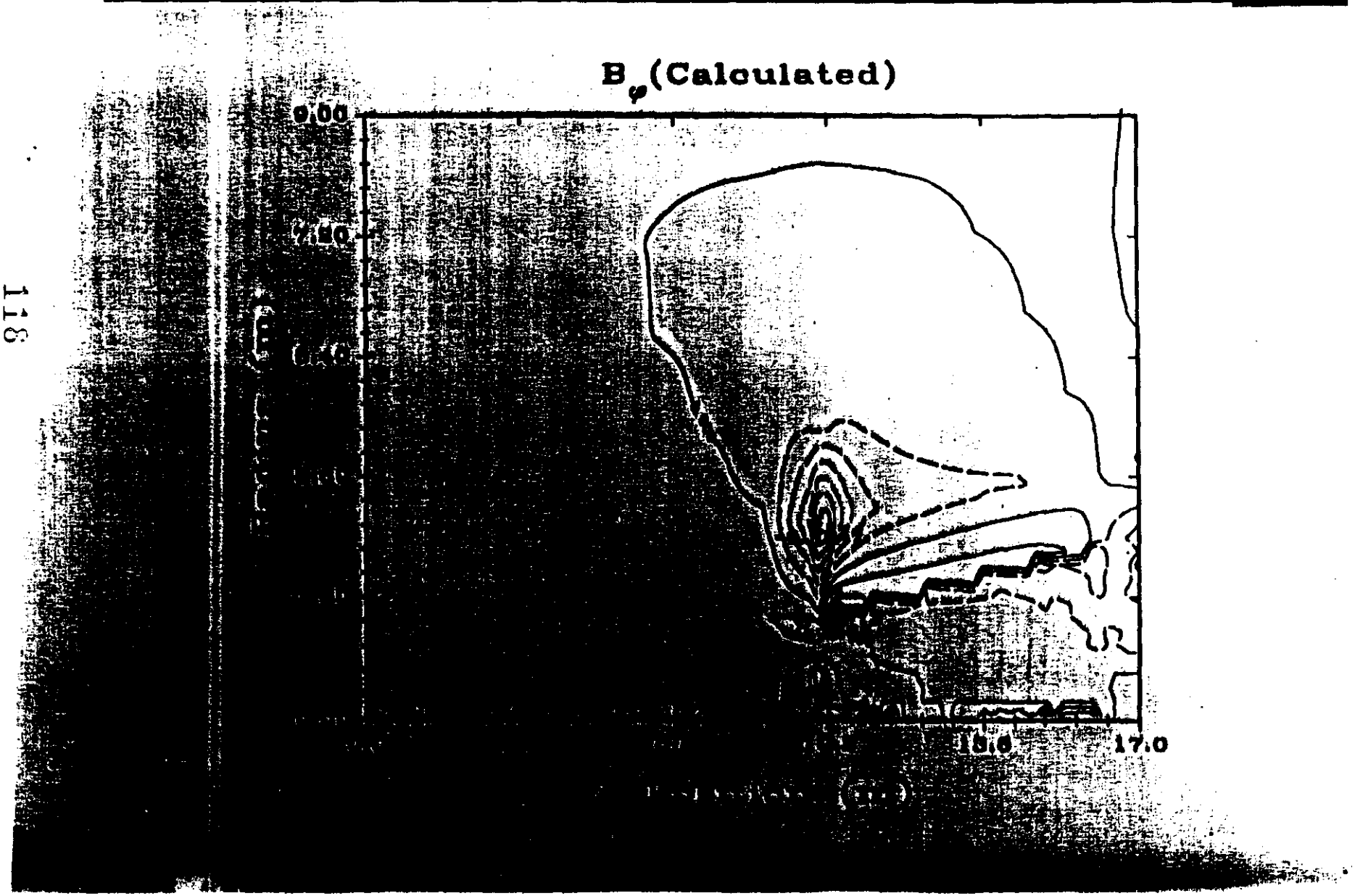

B_r is not well behaived near the field shapper

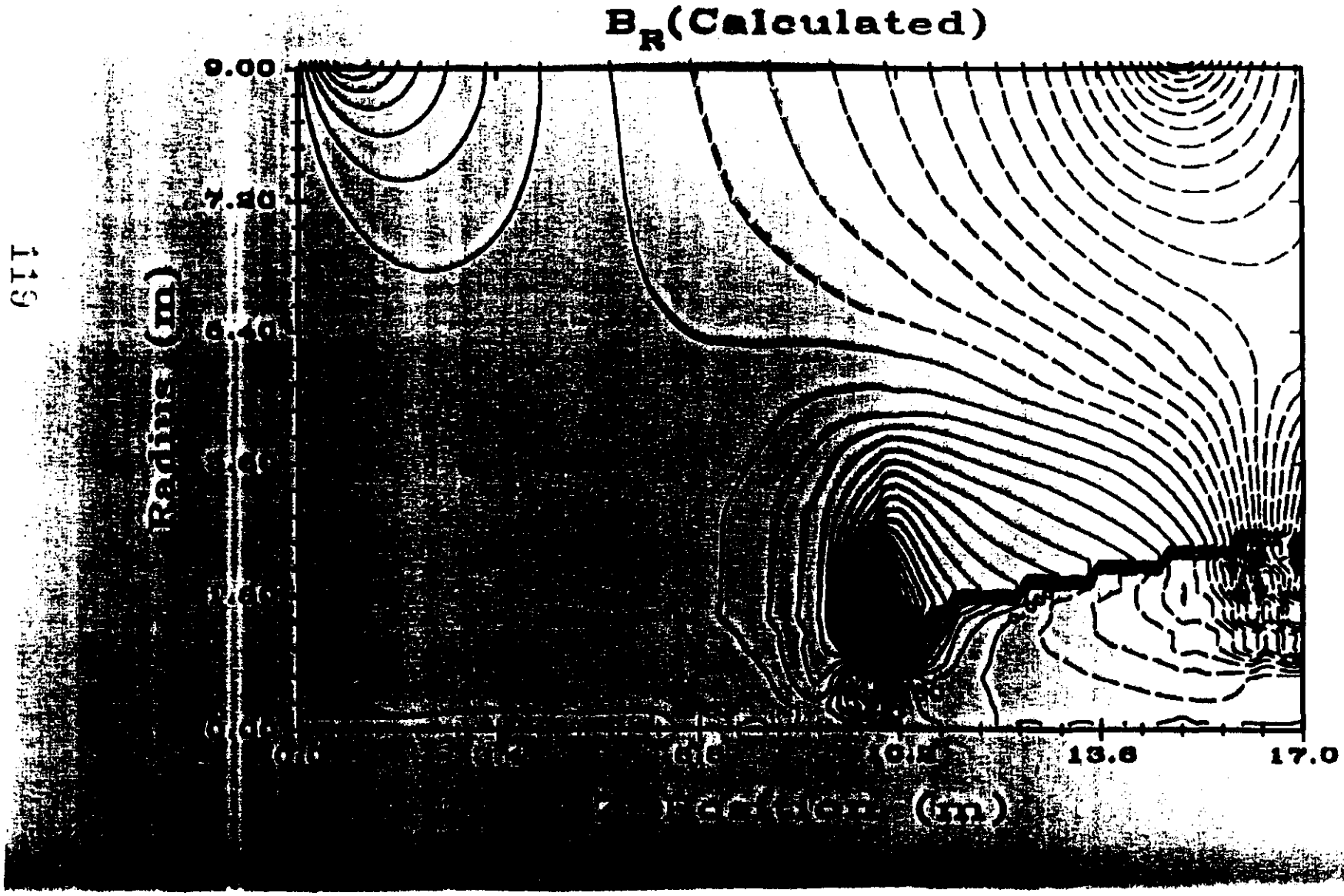

B_z is not well behaived near the field shapper

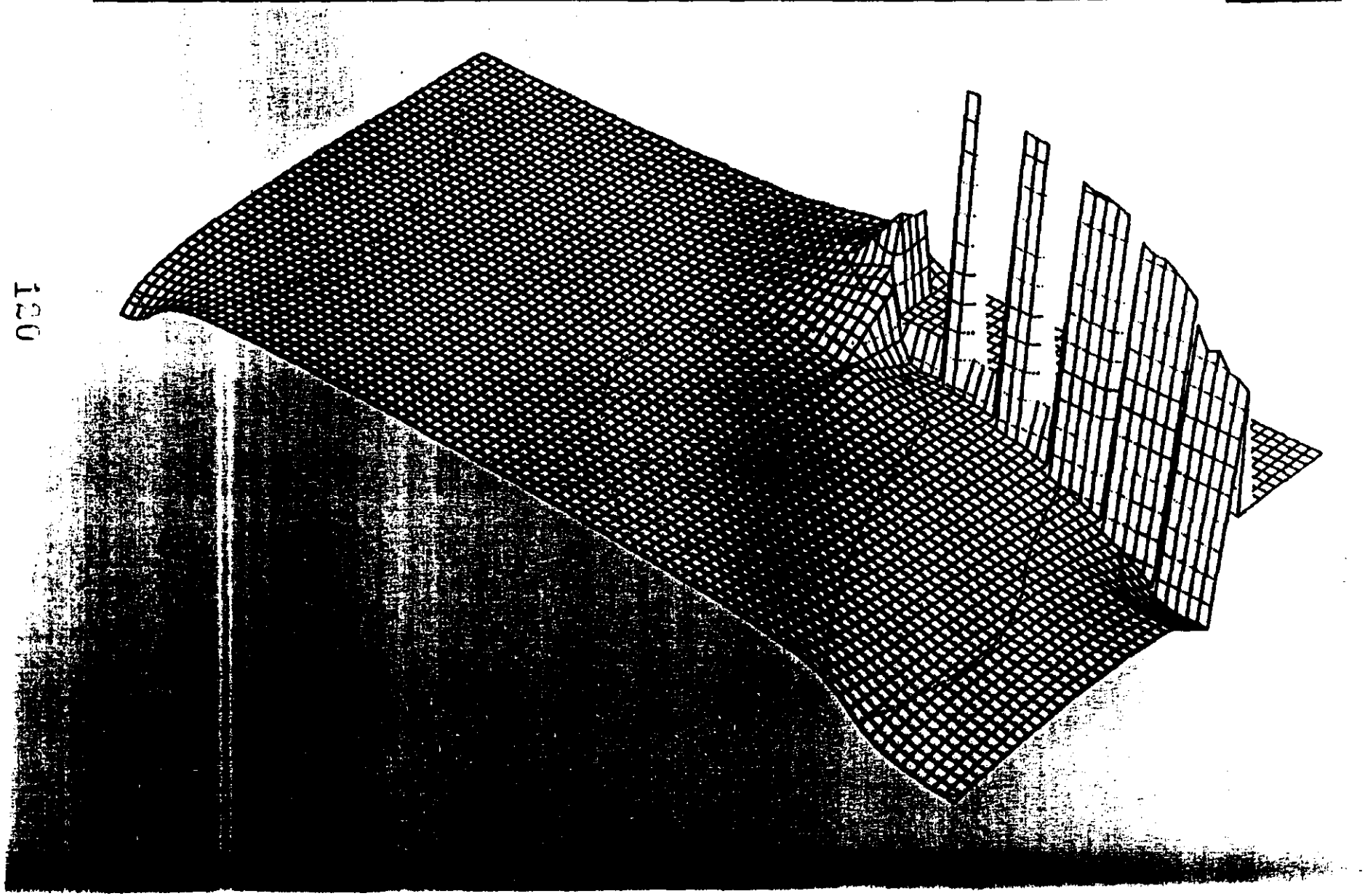

Fitting Procedure

- 2-d problem first
  - First fit to the entire ~4000 point array to determine the number of terms necessary to adequately represent the field
  - Using this number of terms, minimize the number of and optimize the probe placement to reproduce the field--Ultimately the placement and measurement accuracy must be included
- Expand the problem to 3-d and repeat the previous procedure
- One can play some fitting tricks

Fitting Procedure

- **Expand the solution of Laplace's equation in cylindrical coordinates**

$$B_r = \sum_{i=1}^{N} \left\{ \frac{a_i}{c_i} \sinh\left(\frac{z}{c_i}\right) J_1\left(\frac{r}{c_i}\right) + \frac{b_i}{d_i} \sin\left(\frac{z}{d_i}\right) I_1\left(\frac{r}{d_i}\right) \right\}$$

$$B_z = B_0 - \sum_{i=1}^{N} \left\{ \frac{a_i}{c_i} \cosh\left(\frac{z}{c_i}\right) J_0\left(\frac{r}{c_i}\right) + \frac{b_i}{d_i} \cos\left(\frac{z}{d_i}\right) \right.$$

B_Z(Calculated) - B_Z(Fitted)

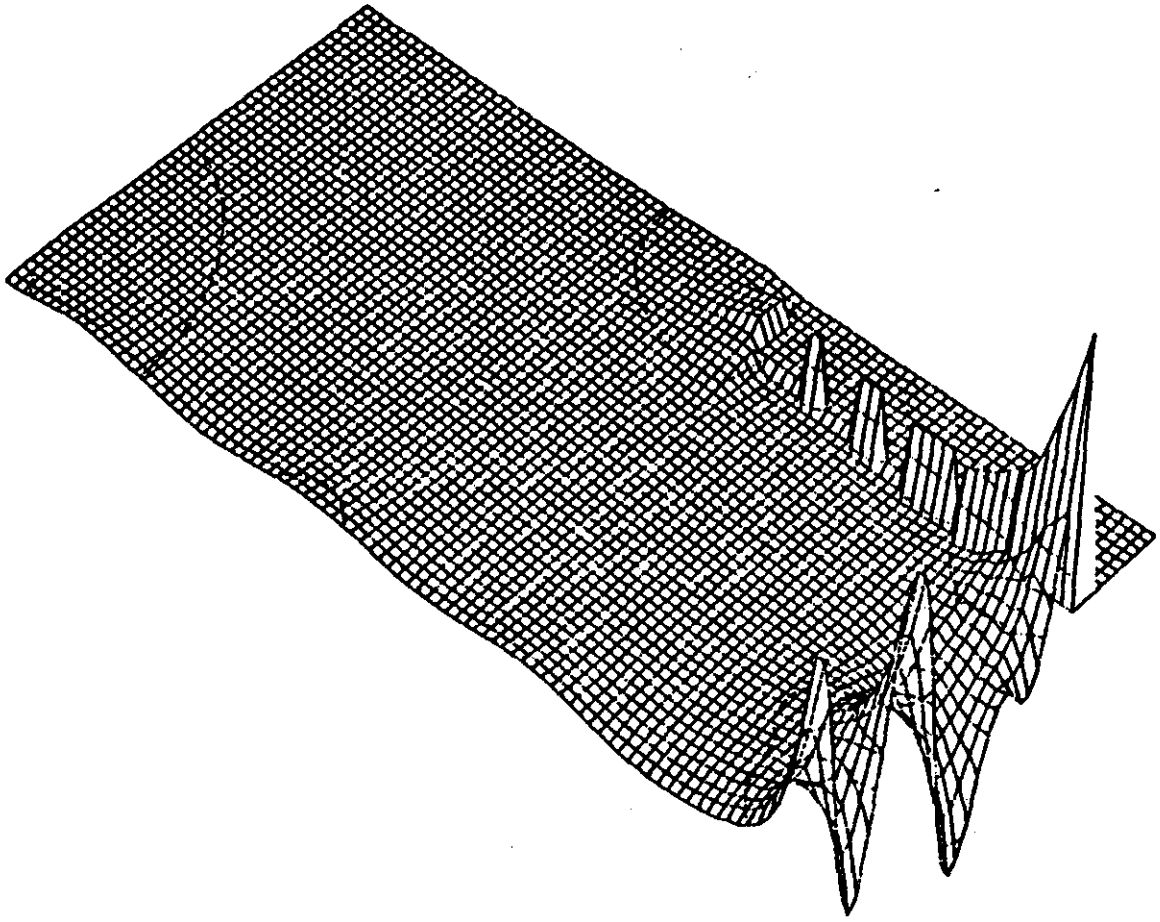

B_r(Calculated) - B_r(Fitted)

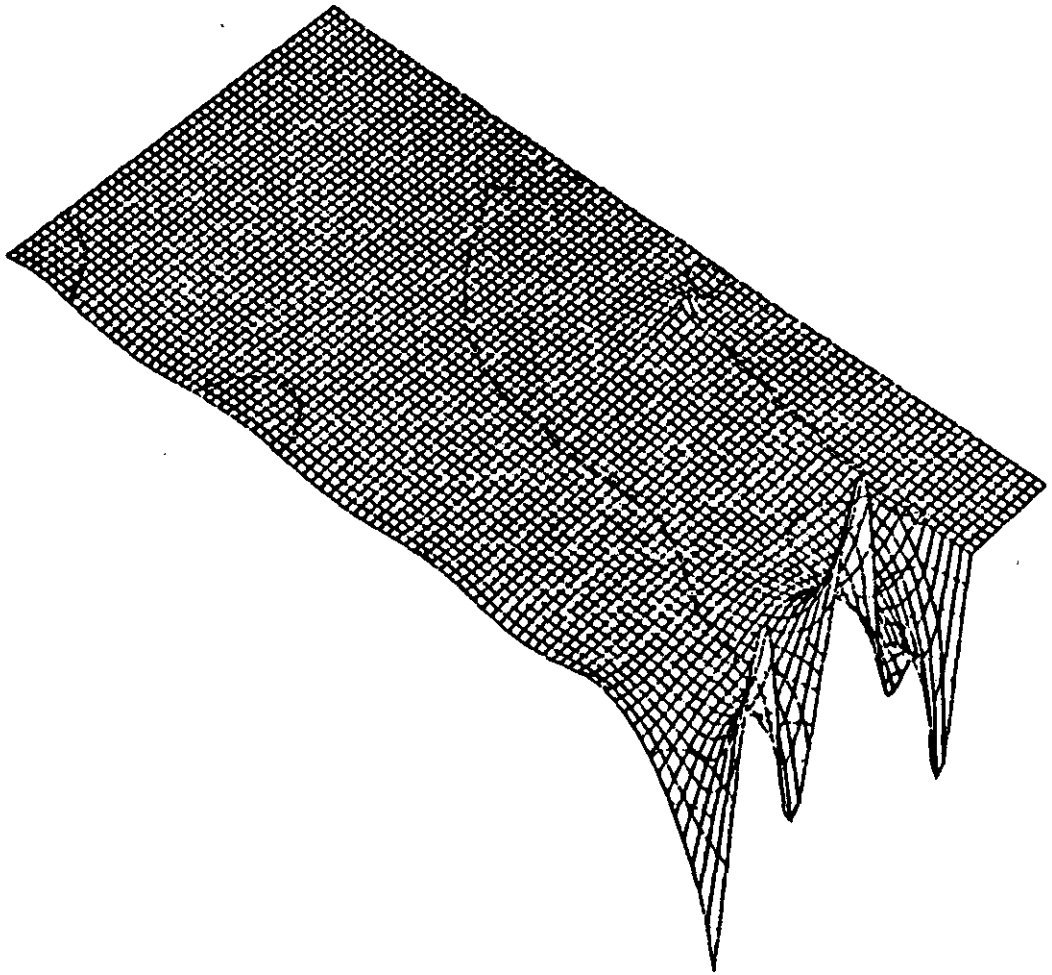

GEM

M.I.T. Workshop on Magnetic Measurements

Distributed *(Virtual)* Source Approach

August 20, 1993

J.D. Sullivan
MIT/PFC NW22-247, (617)253-7537
MIT/LNS 24-522, (617)253-7596

L3 Magnetic Field Measuring:

Nominal field: 0.5 T in 1200 m^3 volume

Required knowledge: 0.4%

Measurement system: 992 magnetoresistors spaced 40 G apart on muon chambers and 5 NMR probes monitor the absolute value of the field.

Reconstruction algorithm: B_ϕ (assumed) negligble

1. Assume full cylindrical symmetry, fit truncated Bessel function and a zero-order modified Bessel function (14 parameters) Residuals of 50 G were obtained.
2. Adjust the parameters of *virtual* octagonal, coaxial coils in conjunction with an approximate theoretical field map. This uses full 3-D spatial positions. Two approaches were adopted: First, a constant B_z was assumed and the currents of 17 virtual octagonal coils adjusted to fit the measured B_z-values and a priori field measurements. Second, a 2-D field map (from POISSON) is assumed and four virtual coils used (14 parameters in total). This only uses magnetoresistor data. Both approaches give residuals of 20 G.

Problems: Calibration, limited dynamic and operational ranges, only one component.

GEM Field — Remarks on Mapping :

GEM has a large volume 7668 m^3, inhomogeneous, possibly non-azimuthally symmetric magnetic field which probably is also not mirror symmetric about the mid-plane. This field is generated by superconducting coils (solenoids) and massive conical iron wedges to shape the field and is modified by some nearby magnetic support structures.

Knowledge of the field is needed

- within the tracker volume
- for the muon spectrometer
- along the beam path
- external to the detector in the hall (and on the surface)

Questions

- Needed accuracy?
- Which reconstruction algorithim? What fit method — LS or TLS?
- Number of sensors? What kinds? Where located? What errors (tolerances) are acceptable?
- How much redundancy?

Reconstruction Algorithims — Survey:

- Orthogonal function fit to measured field values but does not necessarily satisfy Maxwell's equations. However, if grid is fine enough, even a linear polynomial fit should work.
- Magnetic potentials (expansions in orthogonal functions)
  - scalar potential — needs only one field component on convex surface
  - vector potential — use Green's function expansion but vector field on (concave) surface
- Direct modeling of sources, e.g., conductor and iron but the inversion may be ill-conditioned.
- Direct modeling of *virtual* sources, e.g., coils and current sheets, for the difference field (from nominal)

Virtual Sources — Advantages:

Why *virtual* sources?

- Most (all known) azimuthal asymmetry is removed with a near complete real source model.
- Automatically satisfies Maxwell's equations
- Permits operational field reconstruction
- Successful on L3 and SLD

Field Mapping — Number of Measurements:

Assume field source modeling —

Source	Specification	Total/half-GEM
Coil	10 parameters $\times$ 12 segments	120
Interconnects	2×11	22
Current return	6×2	12
FFS	$3(\vec{M}) \times 3(\rho) \times 12(\phi) \times 16(z)$	1728
Cryostat	$12(\phi) \times 12(z)$	144
External legs, etc.		74
SUM		2100

This implies 700 vector sensors per half GEM. Note that this is the number of parameters and consequently the minimum number of measurements required for this approach.

Field Mapping — Number of Measurements:

Naive volume scaling from L3 gives total of 6338 or 3169 for half-GEM. However, the GEM field is more complex.

Assume L3-like modeling on muon chambers every 100 G in $|\vec{B}|$ or B_z —

Location	Specification	Total/half-GEM 30°-sector
Barrel chambers	outer	70
	middle	14
	inner	3
Endcap chambers	inner	3
	middle	14
	outer	35
$\eta = 9.75$		137
SUM		276

Thus, 3312 per half-GEM. Note that this is not the number of paramters so that there is a high degree of redundancy. The *eta* strings replace the a priori L3 measurements. Finally, azimuthal symmetry is not assumed.

Assume L3-like modeling on inclosing space frame every 100 G in $|\vec{B}|$ or B_z — 251 per sector or 3012 per half-GEM.

Field Mapping — NMR Probe Number and Location:

NMR probes are needed to

- Accurate field magnitude (tuning to 0.8 T)
- Check common axes and tracker field
- Provide fixed calibration for other probes.

Their placement could be

- two triplets on outside of tracker (extreme z)
- four triplets on each field shaper
- two triplets on space frame

This gives 36 NMR probes in total (L3 used 5 and volume scaling might suggest 32).

Sensor Requirements — Comments:

Clearly (as for L3) the sensors must be

- Physically small ($\leq$ 3 cm)
- Inexpensive
- Accurate and stable
- Not complex (minimum number of leads)

Hall probes seem almost ideally suited given the linearity, sensitivity, temperature coefficient, and calibration required. Of course the number of leads may be a problem (4 per axis and 2 if a thermistor is required); magnetoresistors require only 2 for an axis but are not vector measuring which is important for our inhomogeneous field. Only radiation hardness need be verified but in the muon detector volume this does not seem to pose a problem. In the central tracker volume and other high radiation volumes, NMR probes will suffice.

GEM Case 700: Rc 9.459, Zc 0.7662-14.955, FFS Rbore 0.35, ø9.4-.25

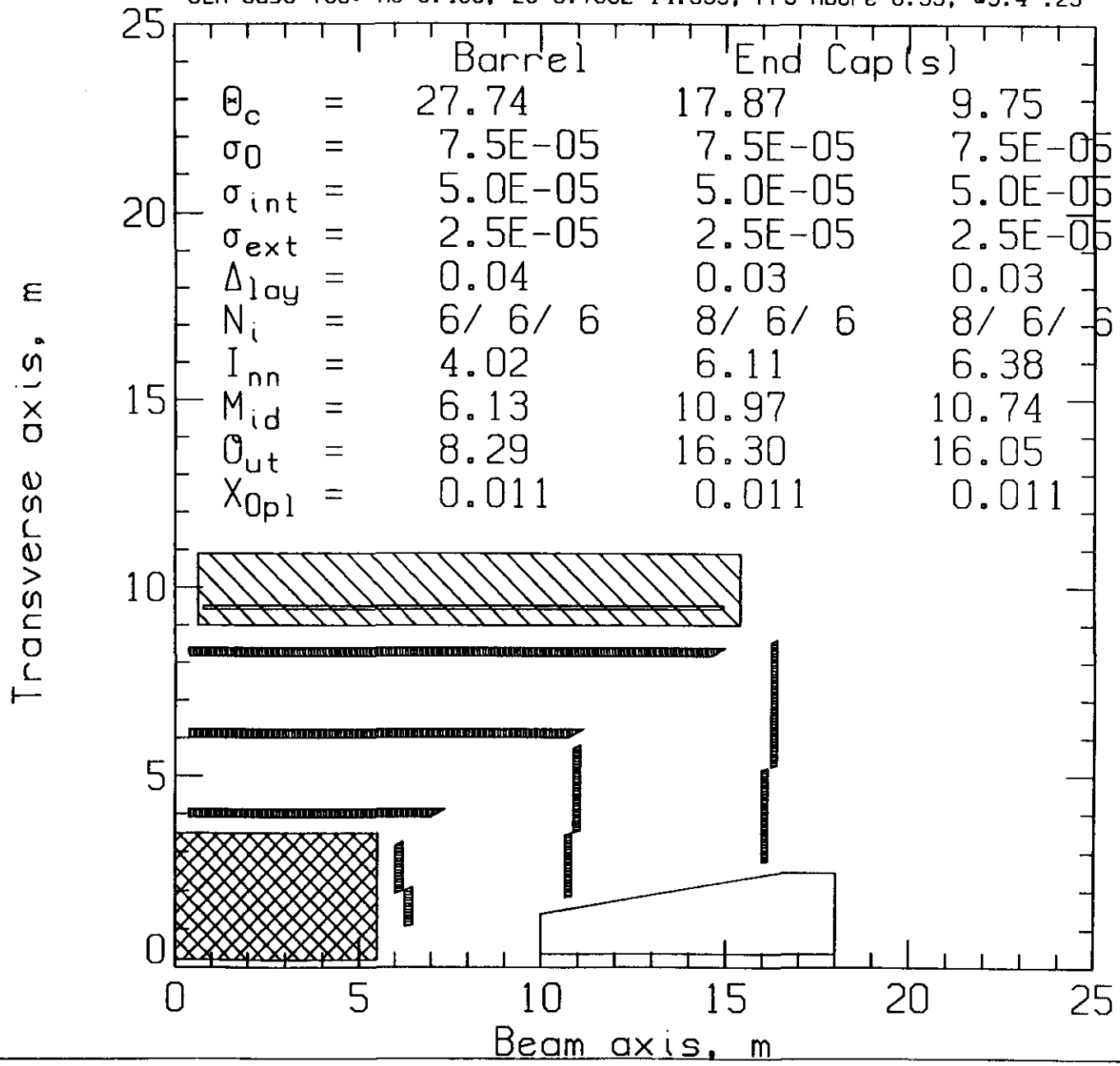

Muon: FN-03Mar93_5a Barrel: 6/6/6 Endcap: 8/6/6 h.6

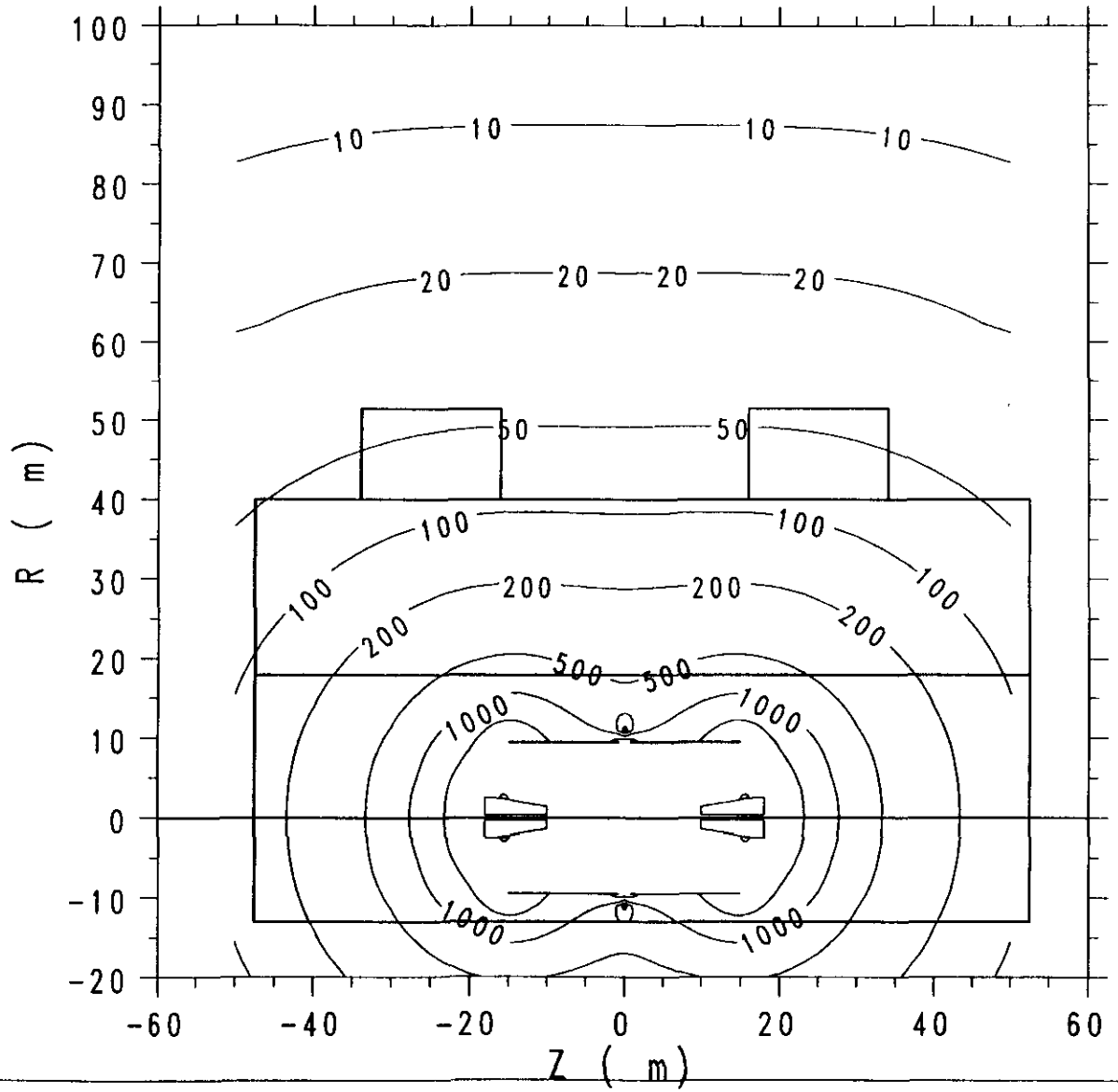
R (m)
Z (m)
100
90
80
70
60
50
40
30
20
10
0
-10
-20
-60
-40
-20
0
20
40
60
10
20
50
100
200
500
1000

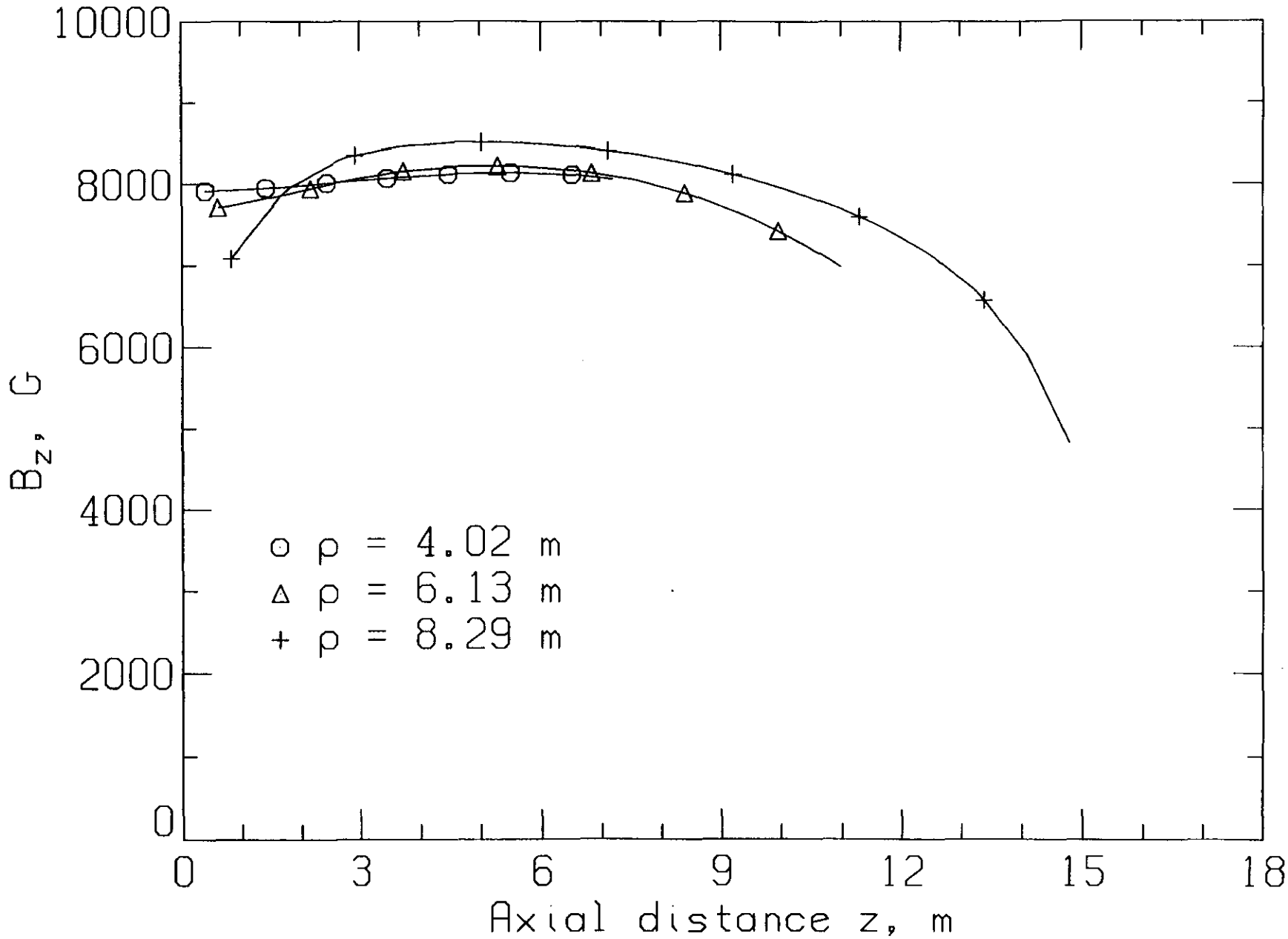
10000
8000
6000
4000
2000
0
B_z, G
0
3
6
9
12
15
18
Axial distance z, m
o ρ = 4.02 m
Δ ρ = 6.13 m
+ ρ = 8.29 m

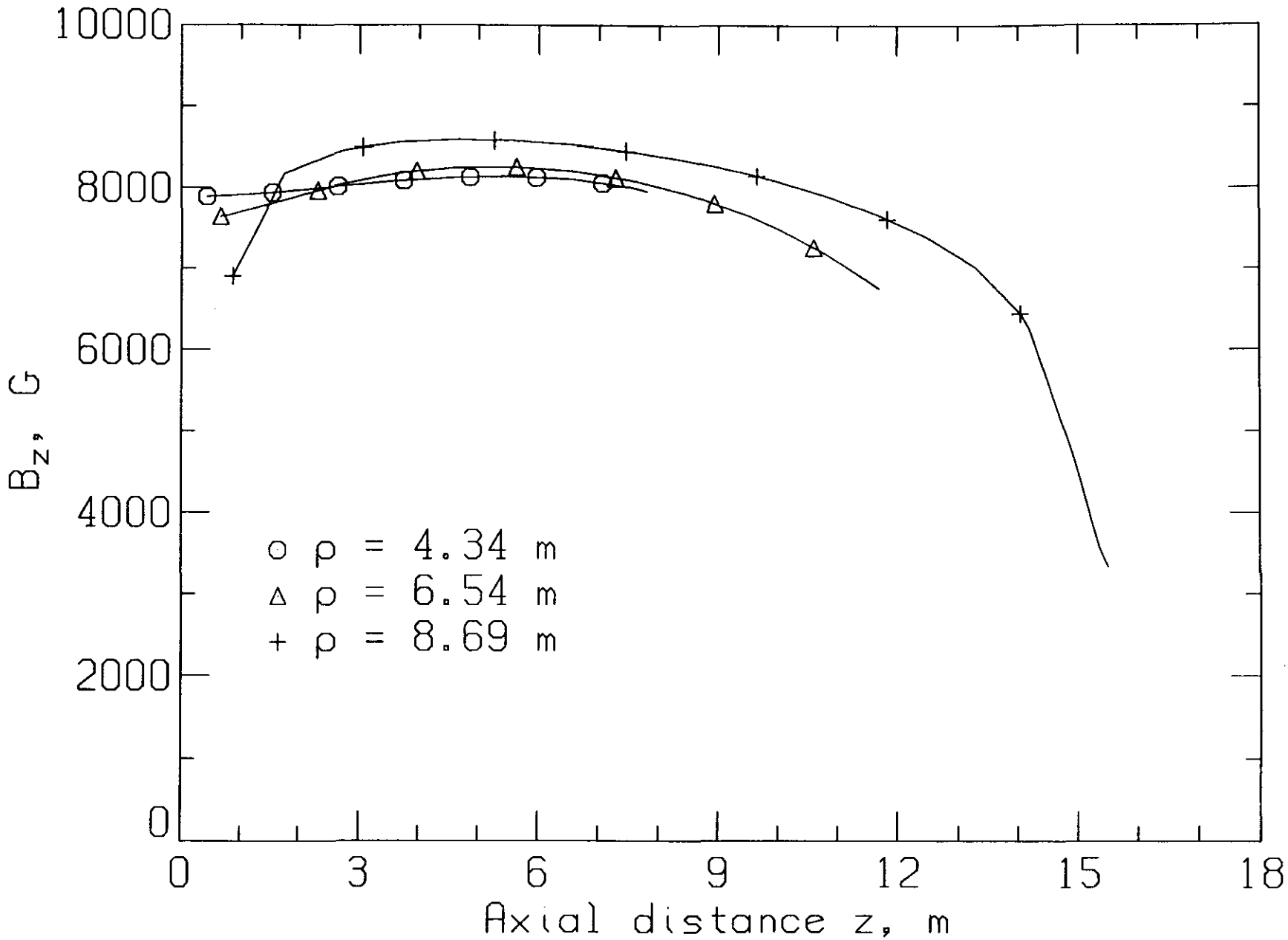
10000
8000
6000
4000
2000
0
B_z, G
0
3
6
9
12
15
18
Axial distance z, m
o ρ = 4.34 m
Δ ρ = 6.54 m
+ ρ = 8.69 m

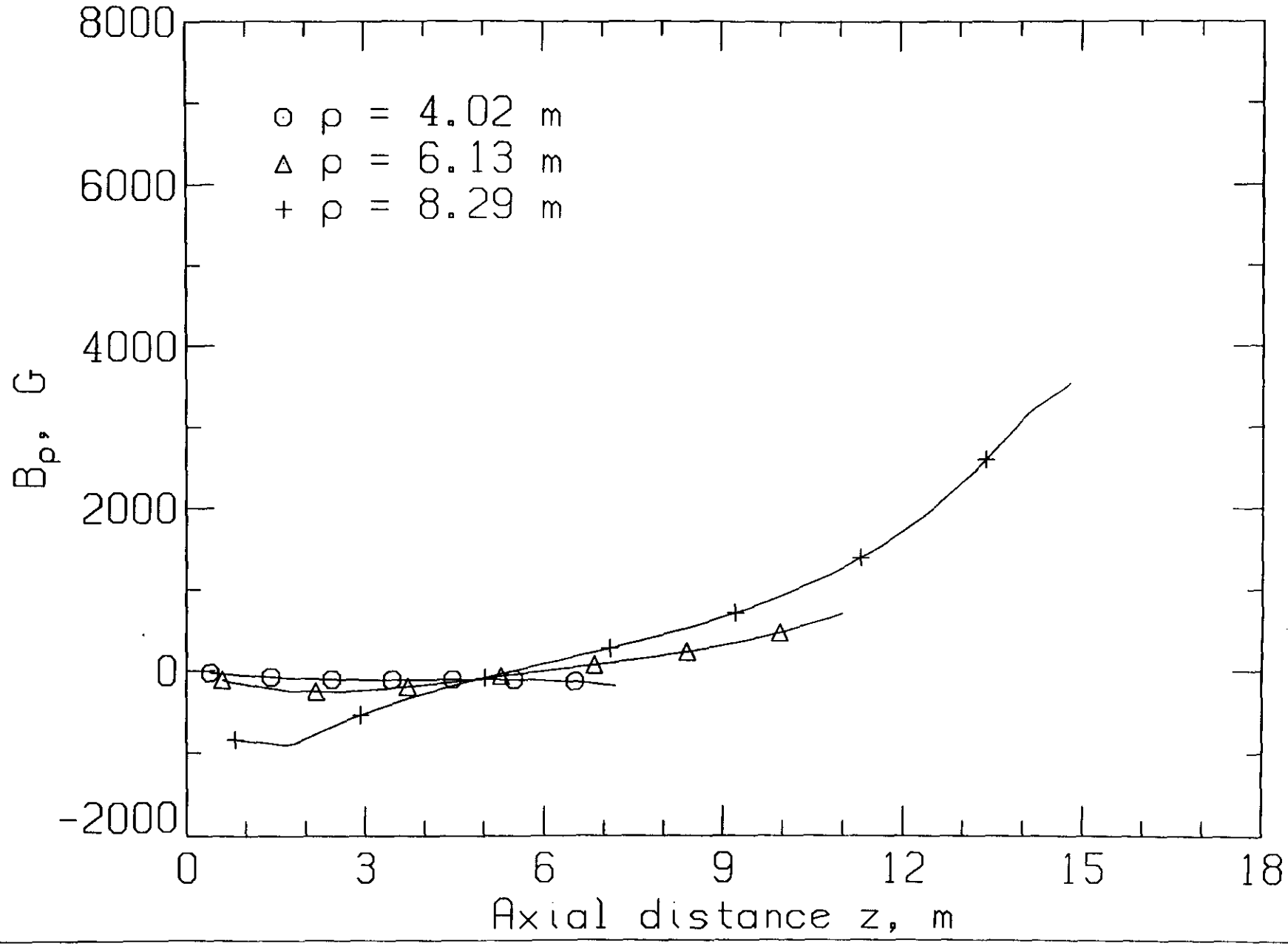
8000
6000
4000
2000
0
-2000
B_ρ, G
○ ρ = 4.02 m
△ ρ = 6.13 m
+ ρ = 8.29 m
0
3
6
9
12
15
18
Axial distance z, m

Fig. 10

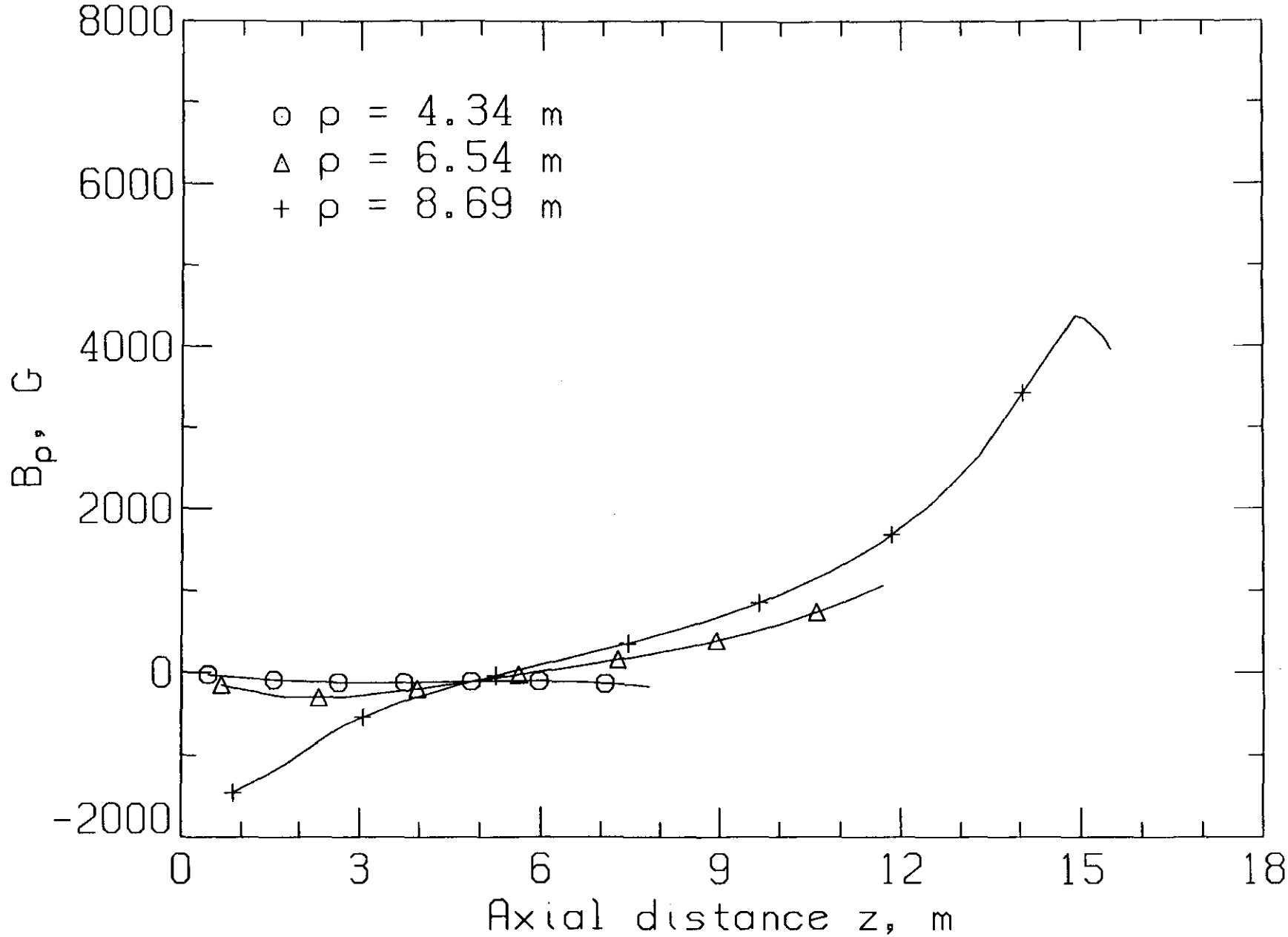
8000
6000
4000
2000
0
-2000
B_ρ, G
o ρ = 4.34 m
Δ ρ = 6.54 m
+ ρ = 8.69 m
0
3
6
9
12
15
18
Axial distance z, m

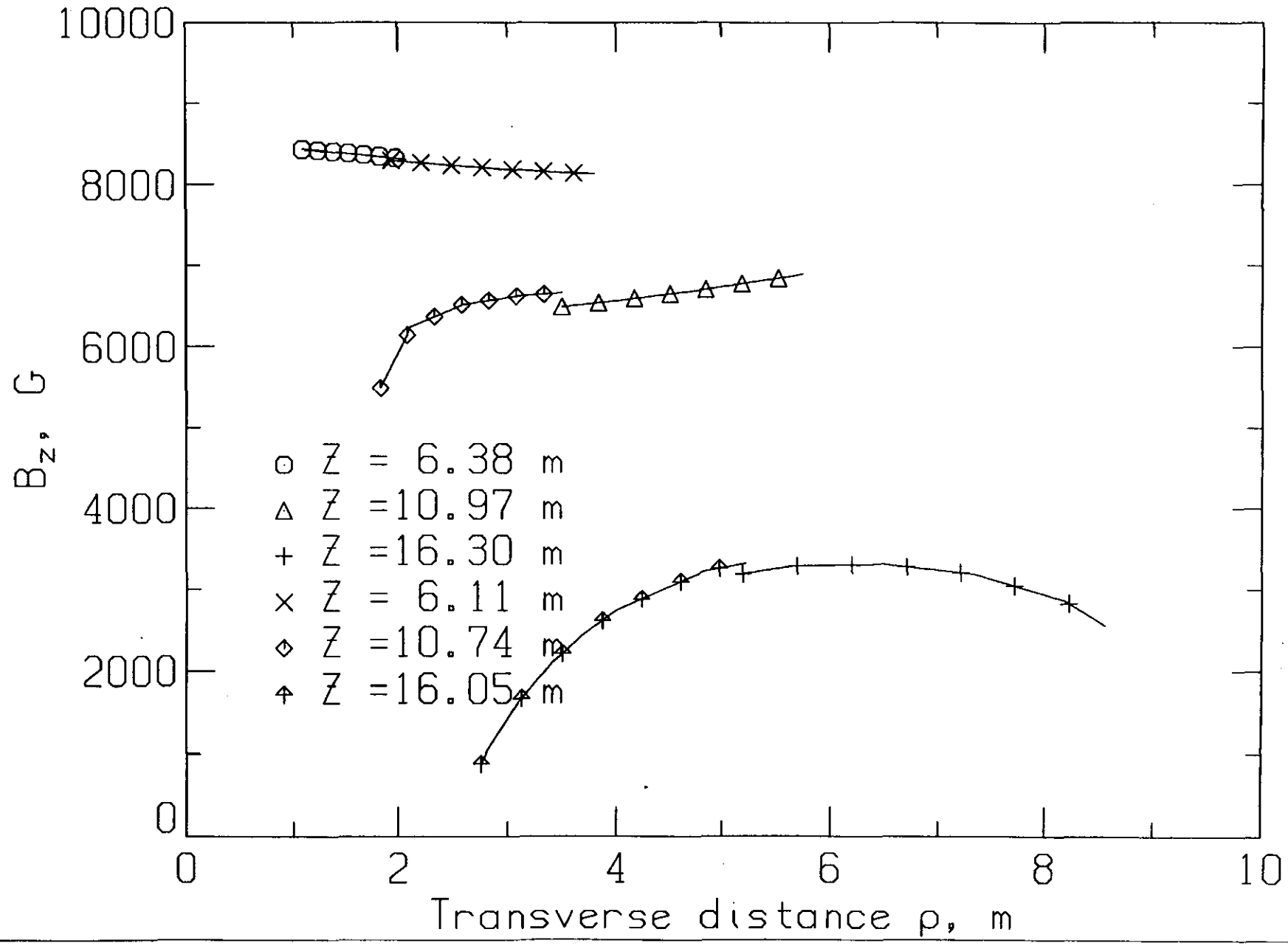
10000
8000
6000
4000
2000
0
B_z, G
0
2
4
6
8
10
Transverse distance ρ, m
Z = 6.38 m
Z =10.97 m
Z =16.30 m
Z = 6.11 m
Z =10.74 m
Z =16.05 m

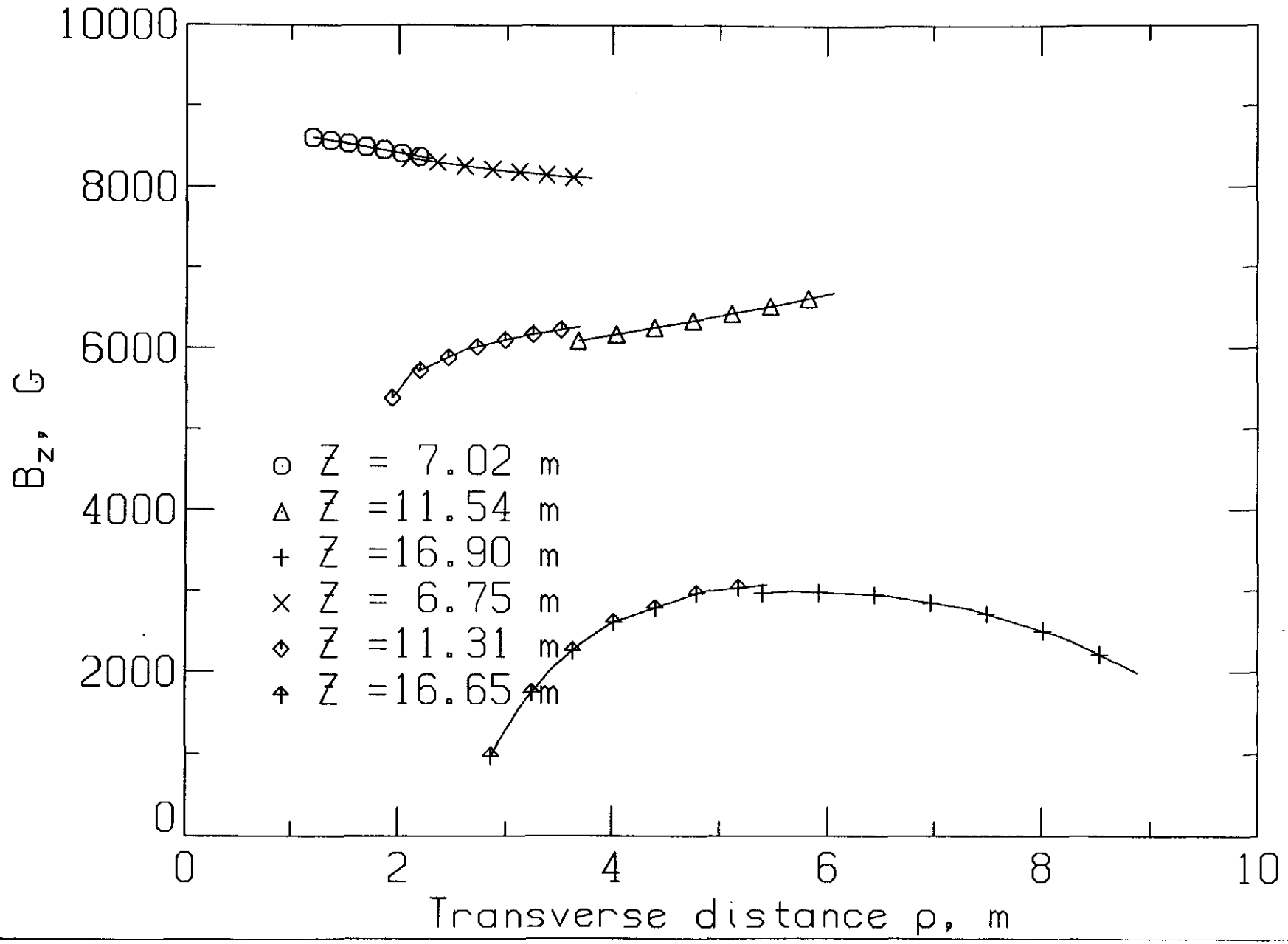
10000
8000
6000
4000
2000
0
B_z, G
0
2
4
6
8
10
Transverse distance ρ, m
Z = 7.02 m
Z =11.54 m
Z =16.90 m
Z = 6.75 m
Z =11.31 m
Z =16.65 m

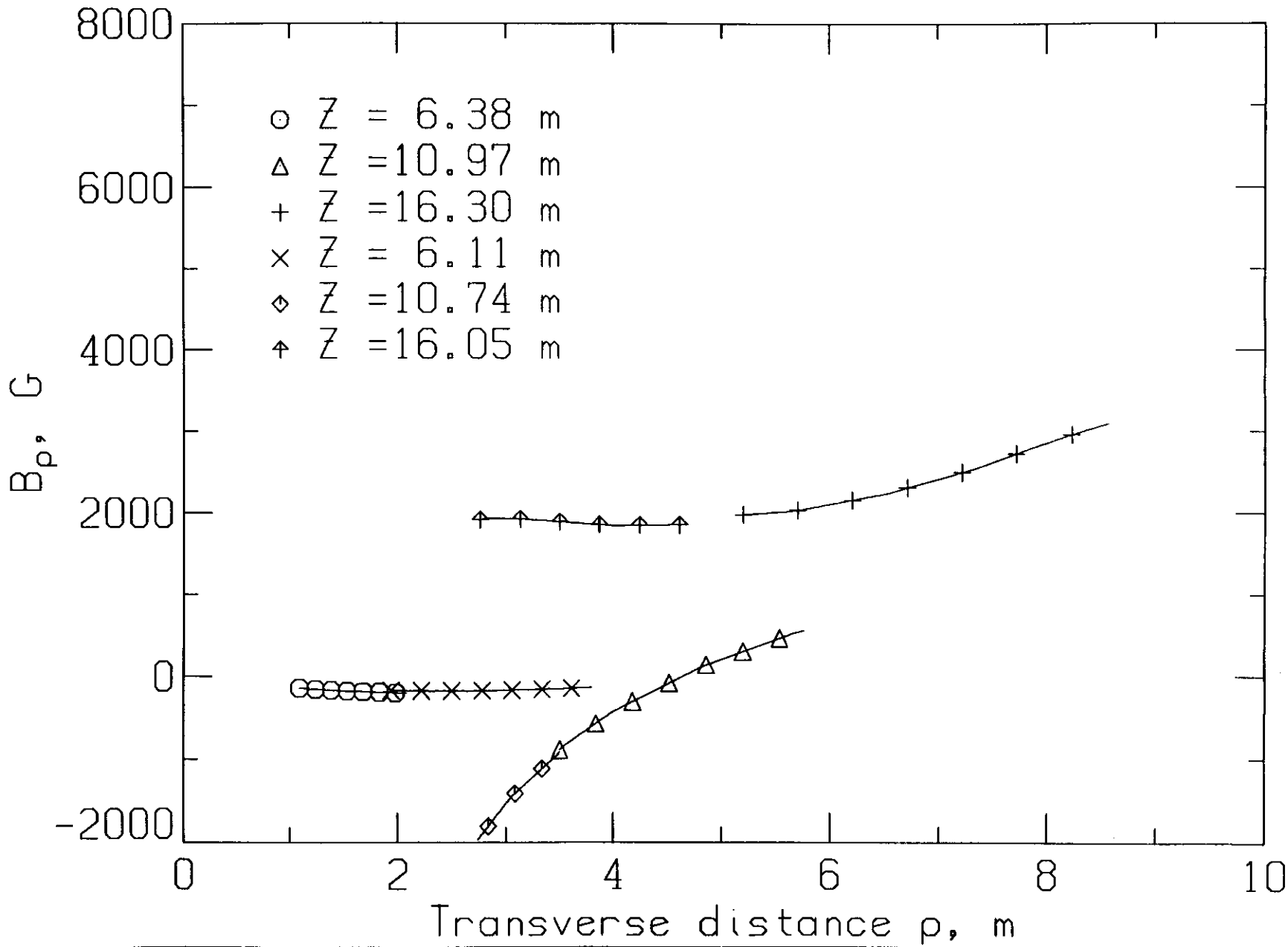
8000
6000
4000
2000
0
-2000
B_ρ, G
0
2
4
6
8
10
Transverse distance ρ, m
○ Z = 6.38 m
△ Z =10.97 m
+ Z =16.30 m
× Z = 6.11 m
◇ Z =10.74 m
↑ Z =16.05 m

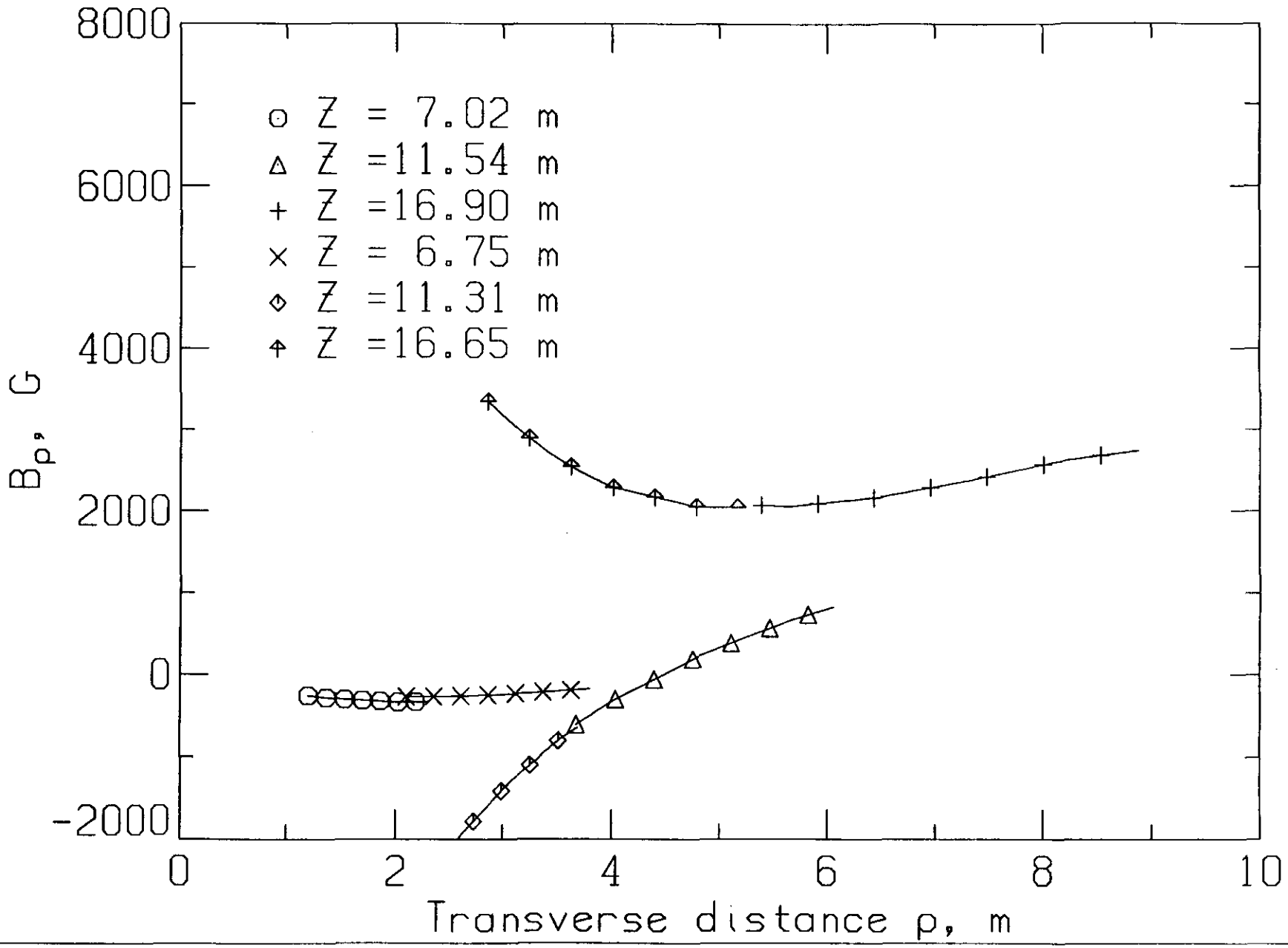
8000
6000
4000
2000
0
-2000
B_ρ, G
0
2
4
6
8
10
Transverse distance ρ, m
Z = 7.02 m
Z =11.54 m
Z =16.90 m
Z = 6.75 m
Z =11.31 m
Z =16.65 m

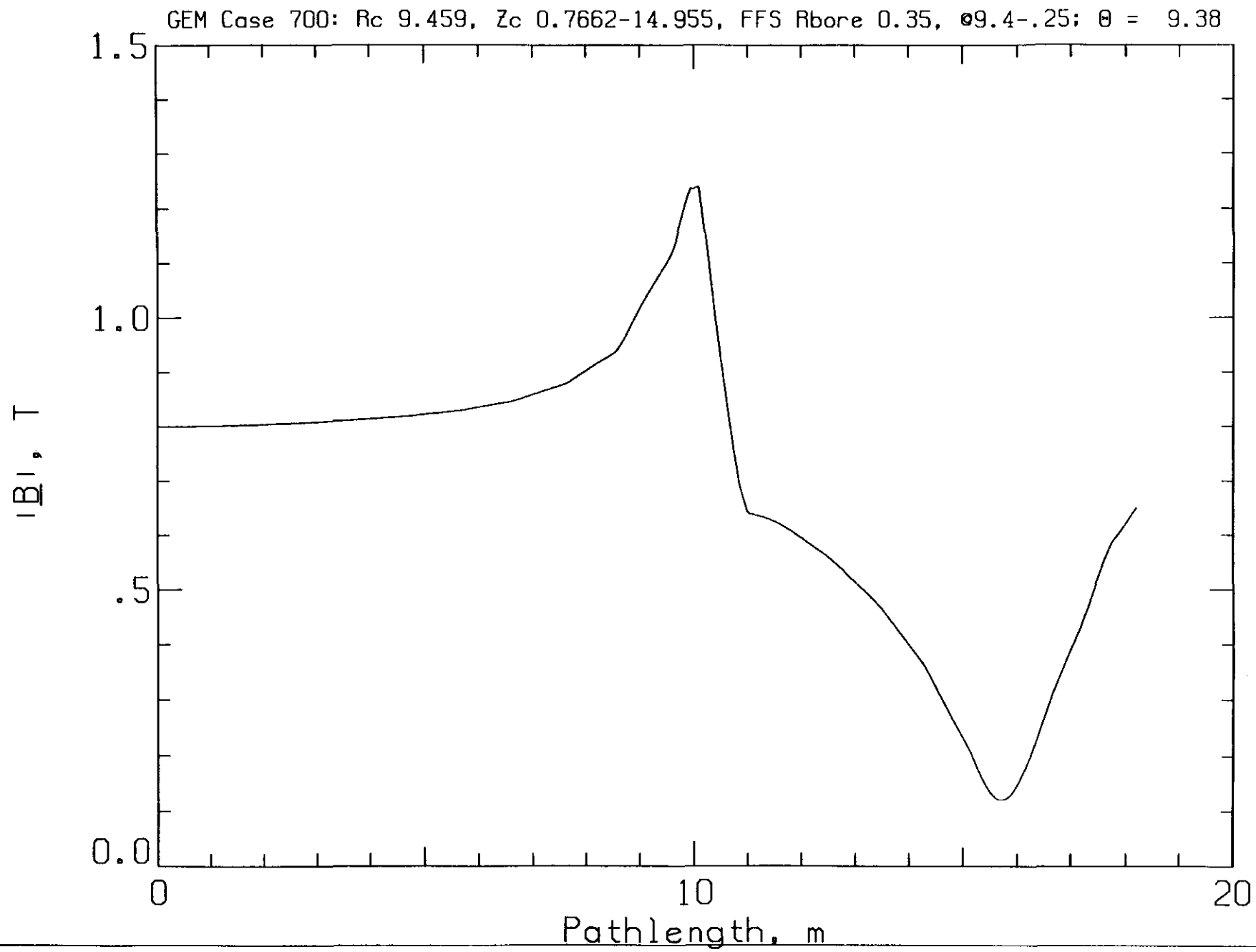
GEM Case 700: Rc 9.459, Zc 0.7662-14.955, FFS Rbore 0.35, ø9.4-.25; θ = 9.38
1.5
1.0
.5
0.0
|B|, T
0
10
20
Pathlength, m

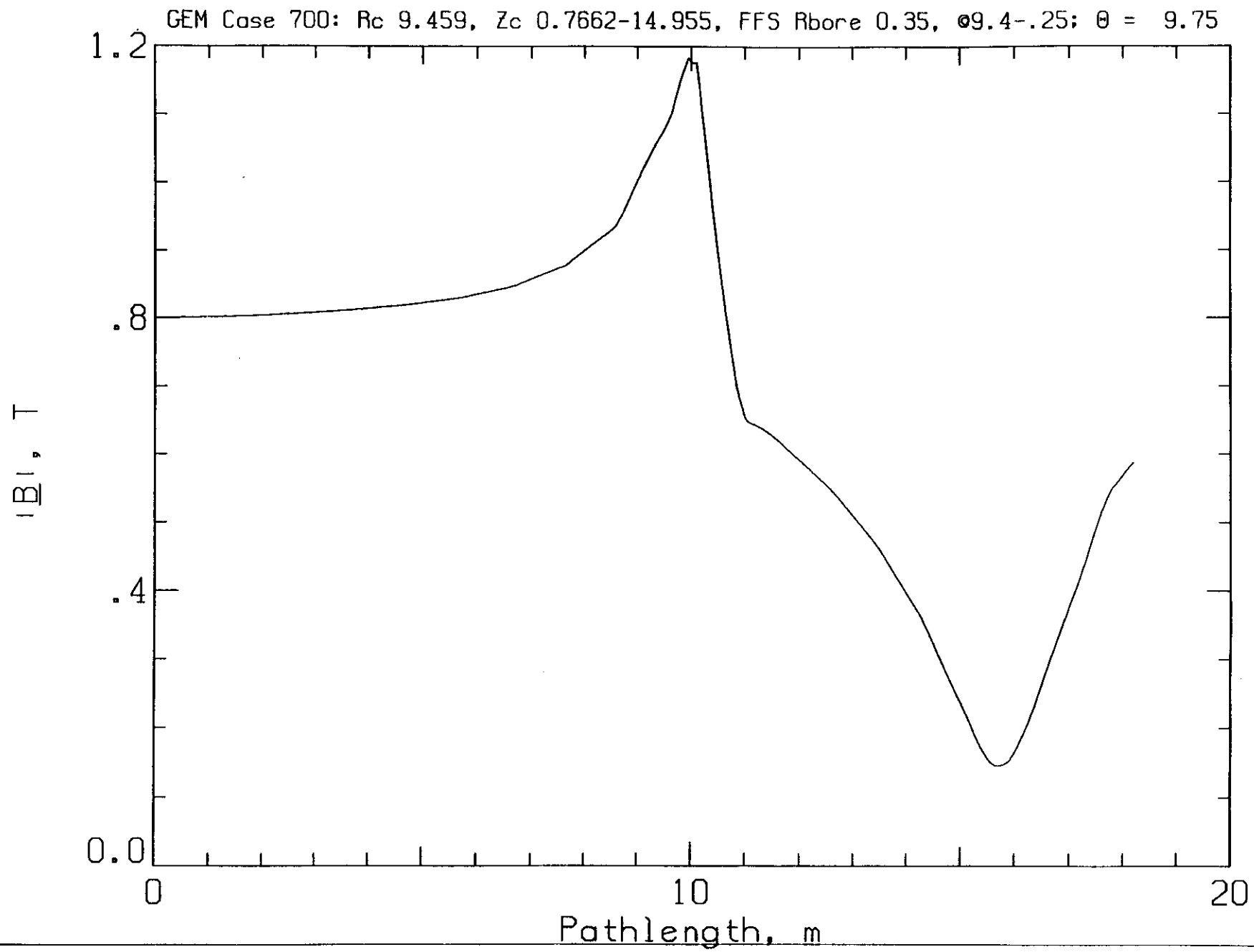
GEM Case 700: Rc 9.459, Zc 0.7662-14.955, FFS Rbore 0.35, ⊗9.4-.25; θ = 9.75
1.2
.8
.4
0.0
|B|, T
0
10
20
Pathlength, m

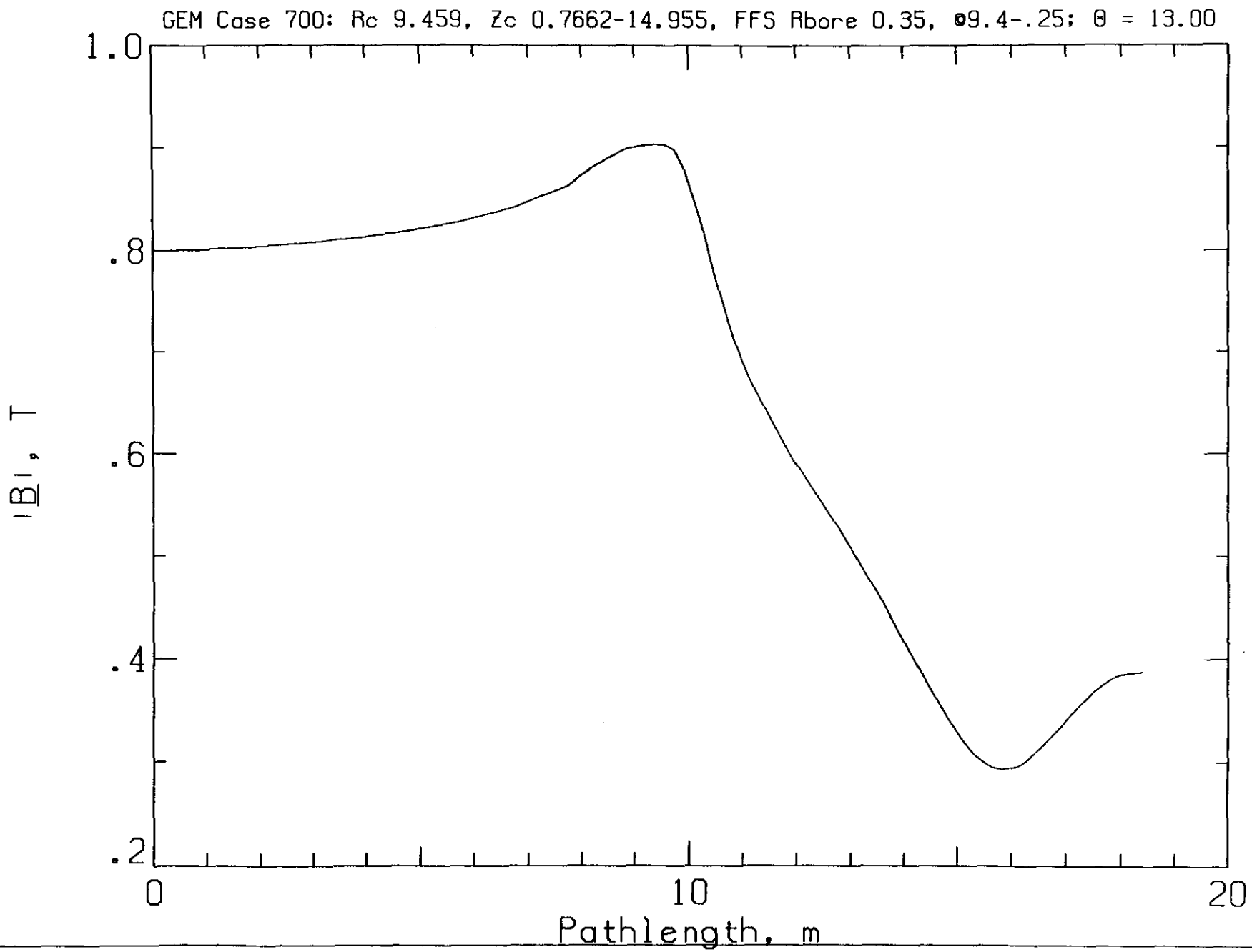
GEM Case 700: Rc 9.459, Zc 0.7662-14.955, FFS Rbore 0.35, ⌀9.4-.25; θ = 13.00
1.0
.8
.6
.4
.2
|B|, T
0
10
20
Pathlength, m

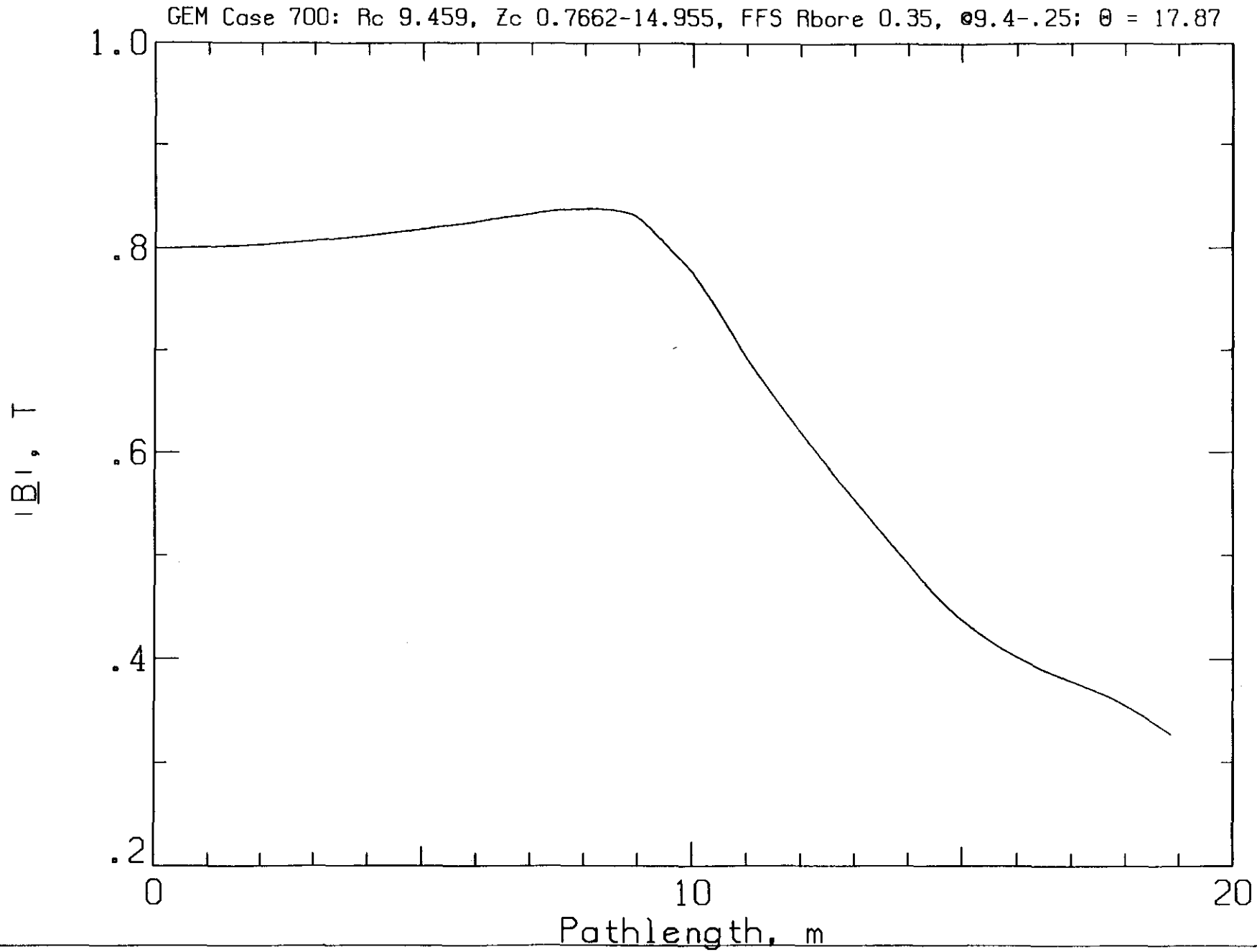
GEM Case 700: Rc 9.459, Zc 0.7662-14.955, FFS Rbore 0.35, ø9.4-.25; θ = 17.87
1.0
.8
.6
.4
.2
|B|, T
0
10
20
Pathlength, m

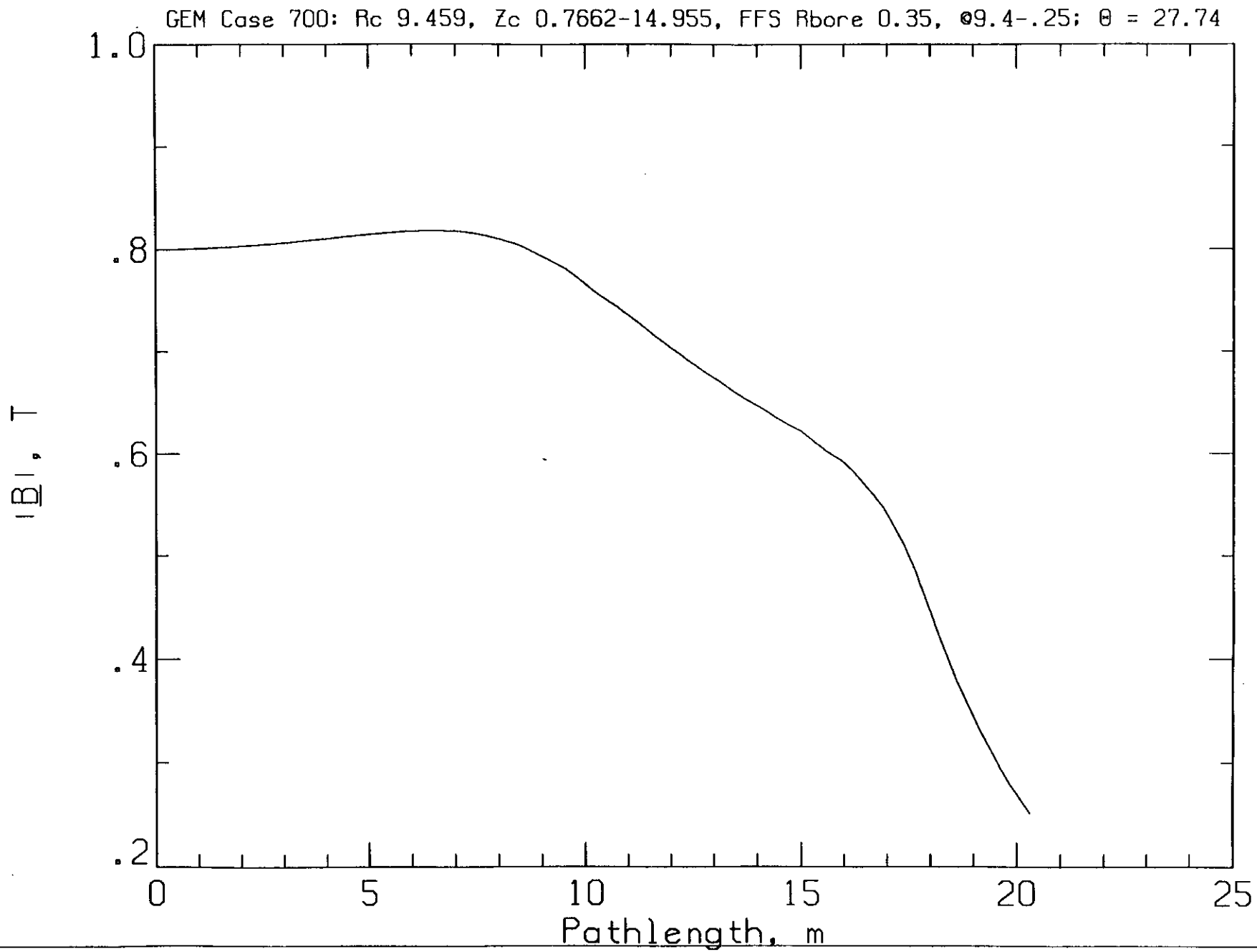
GEM Case 700: Rc 9.459, Zc 0.7662-14.955, FFS Rbore 0.35, ø9.4-.25; θ = 27.74
1.0
.8
.6
.4
.2
|B|, T
0
5
10
15
20
25
Pathlength, m

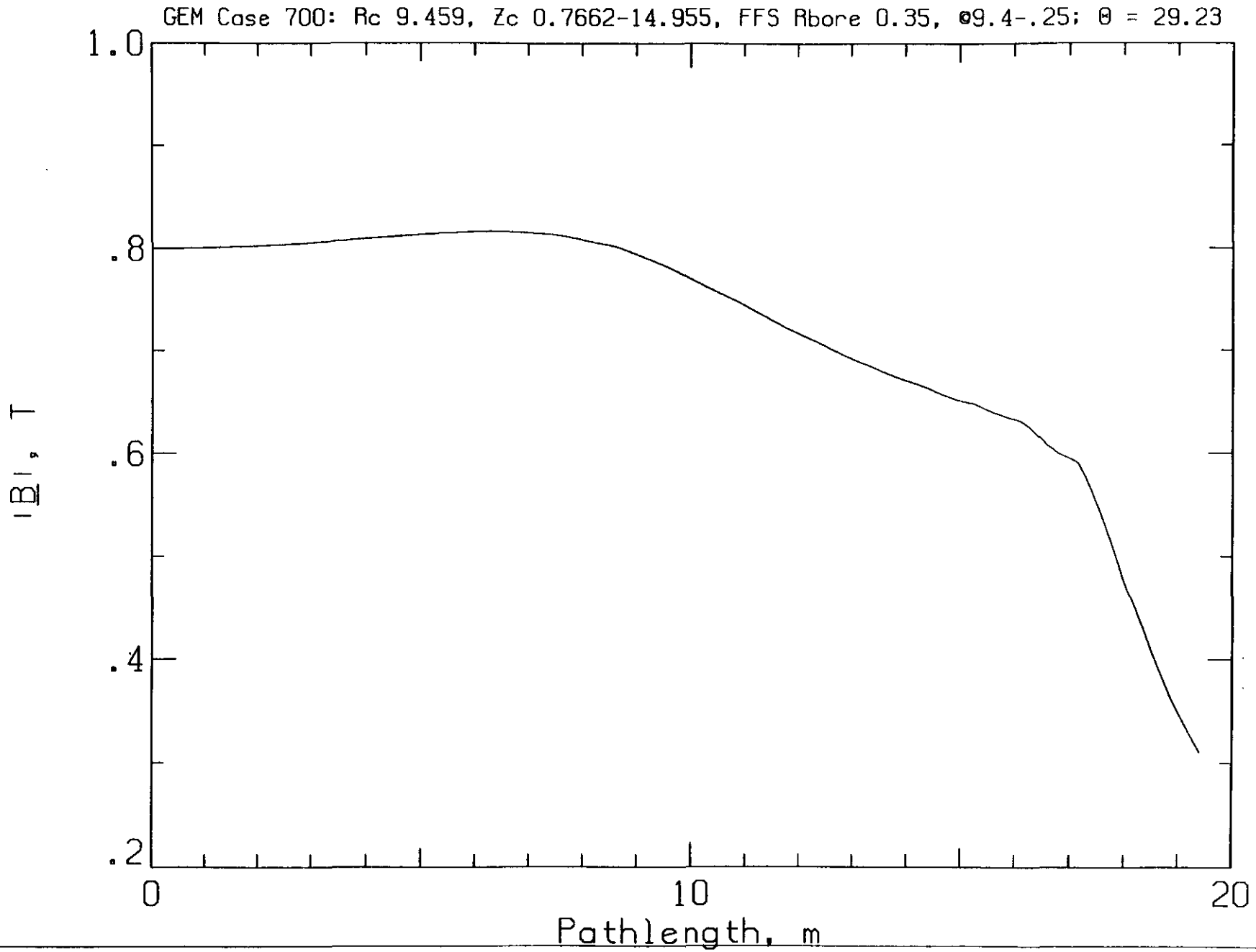
GEM Case 700: Rc 9.459, Zc 0.7662-14.955, FFS Rbore 0.35, @9.4-.25; θ = 29.23
1.0
.8
.6
.4
.2
|B|, T
0
10
20
Pathlength, m

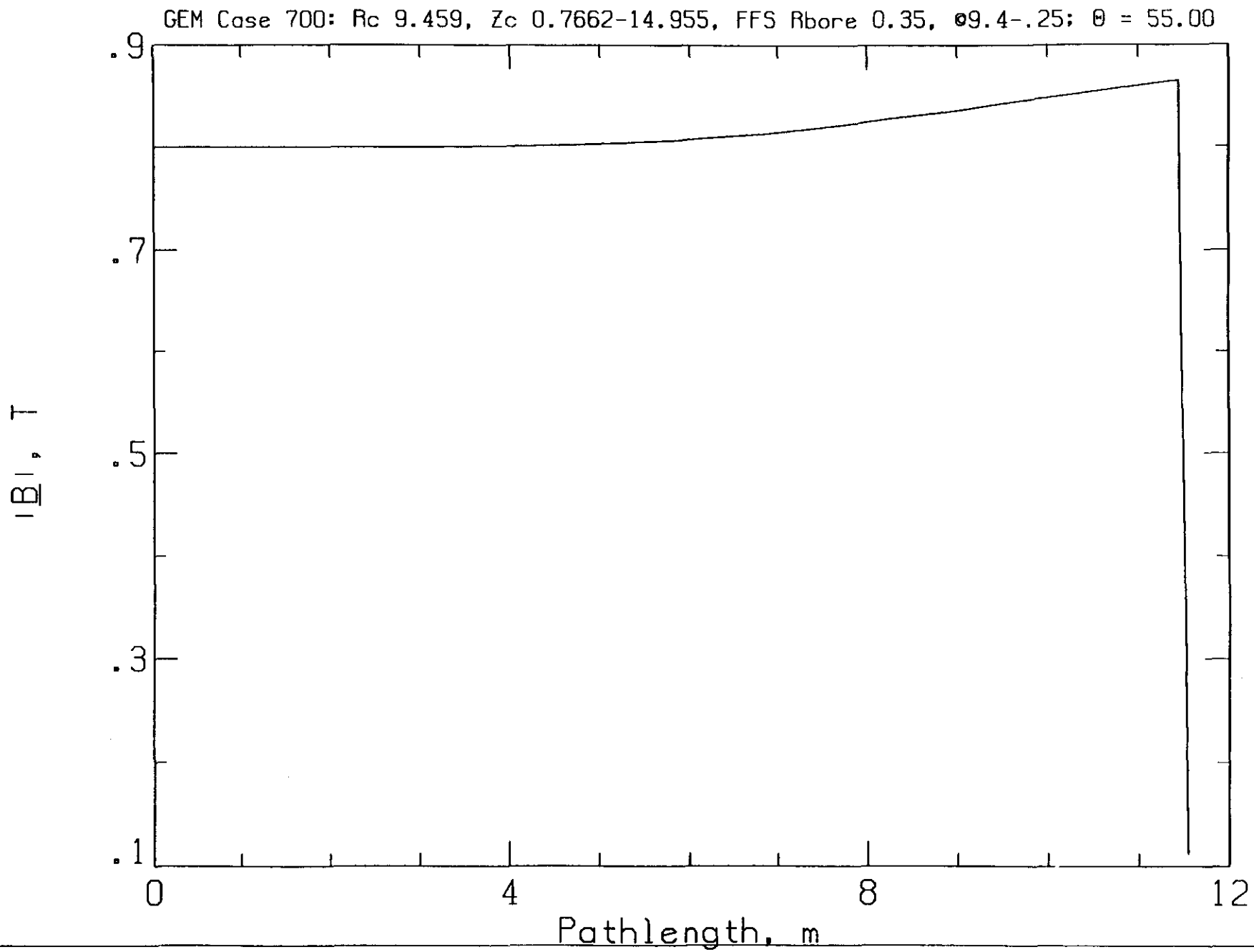
GEM Case 700: Rc 9.459, Zc 0.7662-14.955, FFS Rbore 0.35, ø9.4-.25; Θ = 55.00
.9
.7
.5
.3
.1
|B|, T
0
4
8
12
Pathlength, m

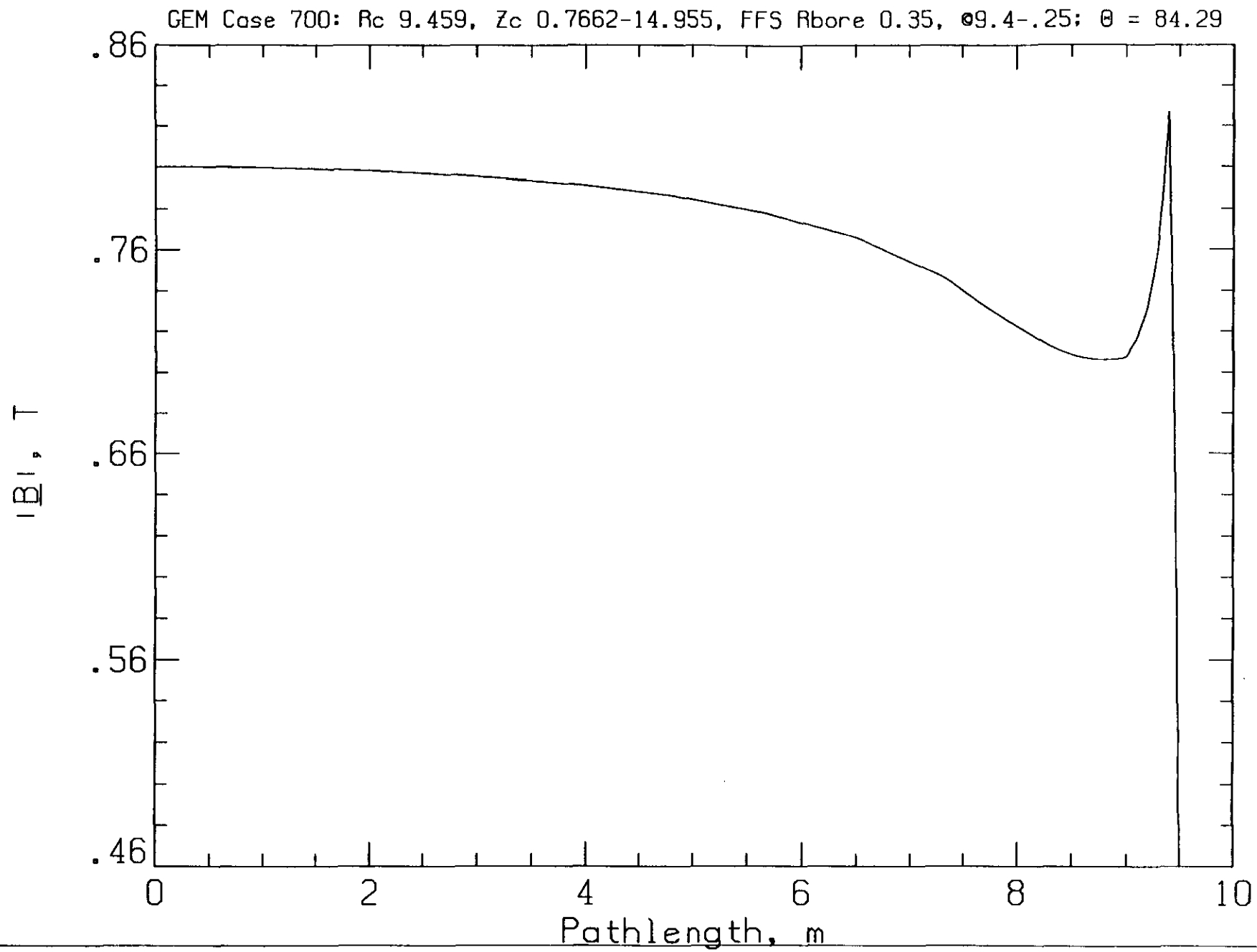
GEM Case 700: Rc 9.459, Zc 0.7662-14.955, FFS Rbore 0.35, ⊗9.4-.25; θ = 84.29
.86
.76
.66
.56
.46
|B|, T
0
2
4
6
8
10
Pathlength, m

GEM

March 26, 1992

To: P. Marston
From: J. Sullivan

Re: Field mapping initiative for GEM

Because of the importance of knowledge of the magnetic field to the success of the GEM experiment and the uncertainties, costs, and schedule impacts of direct field mapping, we have developed a concept for mapping the field by using a finite number of measurements and an analytic fit to determine the field in the active detector volume. We would like to conduct an initial study of this approach to document its utility for GEM. The MIT field mapping study team would include

- J.P. Freidberg, Professor of Nuclear Engineering, (Theoretical Group Leader, PFC),
- R.D. Pillsbury, Jr., Research Scientist and Computational Group Head, PFC,
- W.F.B. Punchard, Principal Research Engineer, NML, and
- J.D. Sullivan, Research Scientist, PFC.

The initial study should determine what accuracy of measurement is needed, the accuracy, cost, and time of measurement with conventional techniques, and define the necessary field transducers (e.g., search coils, Hall probes, NMR probes, etc.) their number and spatial distribution for an analytic solution. The statement of work will include:

- Determination of realistic requirements in consultation with the muon, central tracker, and physics groups and preparation of a preliminary field mapping requirements document. *Need to know what accuracy, components, threshold values, etc before definitive results can be given.*
- Review of current direct measurement praxis and implications (schedule, accuracy, reproducibility, etc.) for GEM; praxis from L3, CDF, and SLD would be covered — it has been suggested that we speak with Dave Luckey and read Dai's thesis for L3, Harry Lynch (now at SSCL), Henry Kendall, and Bill Ash for SLD, and Sham Sumorok (to start) for CDF. Again a summary report would be written.

- Evaluation by computer modeling of the effect of manufacturing (tolerance) errors (winding placement, physical and chemical iron asymmetries, cycling, etc.) on the field, i.e., sensitivity studies.

- Investigation of three analytic approaches

  1. Expansion in orthogonal polynomials. Here, we only need measure one component of the field as $H = -\nabla\Psi_m$,

     $$\Psi_m = c^i f_i$$

     where Ψ_m is the magnetic scalar potential, c^i are the coefficients, and f_i are basis functions. So that,

     $$H_\rho = -\frac{\partial\Psi_m}{\partial\rho} = -c^i\frac{\partial f_i}{\partial\rho}$$

     Dr. Punchard has many years of experience with this approach and, in the central detector volume, it can certainly be done; numerical simulation (experiment) will refine and scope technique.

  2. Green's function analysis, integral equation, on a simply connected, possibly concave, surface (e.g., a sector of the muon detector or even the whole barrel); Prof. Freidberg has twenty years experience applying this method to Stellerator and Tokamak plasmas which are more complex than GEM.

  3. Possible direct modeling of sources (nominal design and homogeneous iron) with perturbations from the baseline.

  An extensive collection of software exists at MIT for each approach.

This effort is estimated to cost $70,000 including travel, computer-costs, etc. and would be completed within four months. The final report will include an estimate of the cost, time, and impact on the GEM construction schedule to measure the GEM magnetic field by both the conventional and analytical techniques.

cc: J. Freidberg
R. Pillsbury
W. Punchard

GEM

PAC Review
Background Material — Field Mapping
TDR sections 3.2.1 and 4.3.1

June 23, 1993

J.D. Sullivan
MIT/PFC NW22-247, (617)253-7537

Field Mapping — Requirements:

Subsystem	Specification	Accuracy
Central tracker	$\lvert\vec{B}\rvert \sim 0.5\%$	40 G
Muon		
Lorentz angle	$\lvert\Delta\vec{B}\rvert \sim 900$ G	900 G
Track reconstruction	$\mathcal{B}\mathcal{L}^2 \sim 0.4\%$	
barrel		35 G
endcap		20 G

Hall probes seem almost ideally suited given the linearity, sensitivity, temperature coefficient, and calibration required. Only radiation hardness need be verified but in the muon detector volume this does not seem to pose a problem. In the central tracker volume and other high radiation volumes, NMR probes will suffice.

Field Mapping — Techniques:

- Magnetic potentials (expansions in orthogonal functions)
  - scalar potential — needs only one field component on convex surface
  - vector potential — use Green's function expansion but vector field on (concave) surface
- Direct modeling of sources, e.g., conductor and iron but the inversion may be ill-conditioned.

The scalar potential is used for NMR magnets and may be suitable for the central tracket volume. The vector potential has been used for MHD devices, stellerators, and tokamaks.

Field Mapping — Number of Measurements:

Assume field source modeling—

Source	Specification	Total/half-GEM
Coil	10 parameters $\times$ 12 segments	120
Interconnects	2×11	22
Current return	6×2	12
FFS	$3(\vec{M}) \times 3(\rho) \times 12(\phi) \times 16(z)$	1728
Cryostat	$12(\phi) \times 12(z)$	144
External legs, etc.		74
SUM		2100

This implies 700 vector sensors per half GEM.

Field Mapping — Experience:

- L3, highly uniform field
- SLD
- CDF
- JET (Joint European Torus), pulsed machine with internal currents

Field Mapping — ROM Costs:

Sensor	Unit cost, k$	Count	Total Cost, k$
NMR	10	9	90
Hall cube	0.2	1400	280
Electronics			30
TOTAL			400